Arrangements einzelner Biomoleküle auf der Grundlage von Single-Molecule Cut&Paste

DISSERTATION

Mathias Strackharn

München 2012

Arrangements einzelner Biomoleküle auf der Grundlage von Single-Molecule Cut&Paste

Dissertation

an der Fakultät für Physik

der Ludwig-Maximilians-Universität

München

vorgelegt von

Mathias Günter Chung-Sab Strackharn

aus Berlin

München, den 14.08 2012

Erstgutachter: Prof. Hermann E. Gaub

Zweitgutachter: Prof. Joachim Rädler

Tag der mündlichen Prüfung: 12.10.2012

Inhaltsverzeichnis

Zusammenfassung

Um zu verstehen, welchen Einfluss kleine Systeme und die von ihnen ausgehenden Fluktuationen auf das Funktionieren einer Zelle haben, ist es zum einen nötig, Modellsysteme zu schaffen, die generellen Aufschluss über ihre Verhaltensweisen geben, zum anderen müssen solche Systeme isoliert beobachtet werden können und einem kontrollierbaren Parametersatz unterliegen. Einer der wesentlichen Parameter für solche Systeme ist die räumliche Anordnung der Komponenten.

Die Single-Molecule Cut&Paste (SMC&P) Technik erlaubt es, Biomoleküle mit großer Präzision (±10 nm) auf Oberflächen anzuordnen, wobei das Konzept auf einem hierarchischen Kraftsystem beruht. Sie konnte genutzt werden, um Bindungsstellen-Gerüste auf Oberflächen aufzubauen, auf die dann in selbstorganisierten Prozessen weitere nanoskalige Objekte binden konnten. Außerdem wurde gezeigt, dass SMC&P herangezogen werden kann, um Validierungsstandards für hochauflösende Mikroskopiemethoden zu erzeugen. Am Beispiel der Blink-Mikroskopie konnte gezeigt werden, dass programmierbare, kontrolliert hergestellte Muster auf Oberflächen als Kalibrierungsstandards verwendet werden können. Mit Hilfe dieser konnte gezeigt werden, wie das Auflösungsvermögen von systemrelevanten Parametern, z.B. der chemischen Umgebung, abhängt.

Die Technik wurde zudem genutzt, um den grundsätzlichen Nachweis der Machbarkeit einer mechanisch kontrollierten, funktionalen Assemblierung auf der Grundlage von einzelnen Molekülen zu erbringen. Hierfür wurden zwei RNA-Stränge, die jeder für sich keine Funktion tragen, mit Hilfe von SMC&P so zueinander positioniert, dass sich aus der Interaktion der Stränge eine neue Funktion ergab. Der zusammengefügte RNA-Komplex konnte als Aptamer das kleine Farbstoffmolekül Malachit-Grün erkennen. Durch das Binden verstärkte sich die Quanteneffizienz des Farbstoffs um drei Größenordnungen, so dass die neue Funktion durch klare Fluoreszenzsignale, die kurz aufblinkend auftraten, auslesbar war. Die Methode funktioniert mit einer solchen Robustheit, dass durch funktionale Assemblierung ein mikrometergroßes Muster in Form der Strukturformel von Malachit-Grün hergestellt werden konnte.

Außerdem wurde die Technik, die zunächst auf den Transport von Nukleinsäuresträngen beschränkt war, so erweitert, dass auch Proteine transferiert werden konnten. Um dies zu erreichen, wurde zunächst gezeigt, dass sich die Bindung zwischen einem Antikörperfragment und einem Antigen-Peptid in das DNA-basierte Kraftsystem so

einfügen lässt, dass Antikörperfragmente am Cantilever für den Transport genutzt werden können. Dazu wurden die unterschiedlichen Abhängigkeiten der Abrisskräfte von Ladungsraten bei den verschiedenen Bindungen ausgenutzt, um die Abrisskräfte aufeinander abzustimmen. Nun wurde als Modellsystem ein Fusionsprotein geschaffen, bei dem ein GFP-Molekül mit dem Antigen-Peptid am N-Terminus sowie sechs Zinkfingern am C-Terminus koexprimiert wurde. Über die Zinkfinger konnte das Fusionsprotein einen Komplex mit einer fluoreszent gelabelten DNA bilden, die ihrerseits im SMCP-Prozess als Anker diente. Mit Hilfe des Antikörperfragments am Cantilever konnten die GFP-DNA-Komplexe zu Mikrometer-großen Ampelmännchen-Mustern zusammengefügt werden, was unterstreicht, dass die Methode robust ist und geeignet für einen funktionellen Transport, bei dem Proteine platziert werden können, ohne dass sie durch die auftretenden Kräfte denaturiert werden.

Einleitung

Auf die Frage, was Leben eigentlich davon abhält, in einen thermodynamischen Gleichgewichtszustand zurückzufallen, antwortete Erwin Schrödinger bildhaft, der Organismus ernähre sich von negativer Entropie (1). Die Ordnung, Organisation und Strukturierung, die in einer Zelle dadurch möglich werden, sind häufig im Zentrum der Wahrnehmung. Faszinierend ist in diesem Kontext, dass schon Strukturbildung an sich durch einen *zufällig* induzierten Prozess in einem dynamischen System erklärt werden kann. Wie von Gierer und Meinhardt beschrieben können eine lokale, verstärkende Reaktion und ein langreichweitiger, antagonistischer Effekt dazu führen, dass schon kleine Fluktuationen in einem homogenen Umfeld Musterbildung auslösen (2). Die Natur hat es geschafft, sich sowohl die sehr deterministischen Abläufe, wie man sie beispielsweise beim Zellzyklus beobachten kann, als auch die Stochastizität etwa von Bindungsereignissen einzelner Biomoleküle zu eigen zu machen. Mechanismen, die in einer Zelle ablaufen, werden häufig von einer kleinen Anzahl von Molekülen kontrolliert. Sicher ist das prominenteste Beispiel die DNA, die als Träger der genetischen Information von ungeheurer Wichtigkeit, jedoch nur in einer abzählbaren Anzahl vorhanden ist. Die sich durch die kleinen Systeme ergebenden Fluktuationen sind für die in der Zelle ablaufenden Prozesse entscheidend. Wie sehr z.B. Genexpression Fluktuationen unterliegt, wurde eindrucksvoll von Elowitz *et al.* gezeigt (3). Durch Expression von Genen, die durch *denselben* Promoter kontrolliert wurden, konnte die Stochastik des Prozesses demonstriert werden. Ebenfalls konnte gezeigt werden, dass die Transkription in mRNA in *bursts* auftritt, also zeitlichen Fluktuationen unterliegt, und dass die Kopienzahlen klein, d.h. von der Größenordnung 10 sind (4). Ob auf Proteinebene Enzyme aufgrund ihrer Konformationsänderungen zeitliche Fluktuationen ihrer katalytischen Aktivität zeigen (*dynamic disorder*) wird noch diskutiert (5, 6). Gleichwohl bestehen theoretische Beschreibungen, deren Validierung auf der Grundlage von Einzelmoleküldaten fortgeführt werden will (7, 8). Gleiches gilt für biochemische Netzwerke, die aus einzelnen Enzymen bestehen (9). Gerade in diesem Bereich sind Modellsysteme mit einem kontrollierbaren Parametersatz notwendig, um die zugrunde liegenden Prozesse zu verstehen.

Feynman wird gerne mit dem Ausspruch zitiert: „*What I cannot create, I do not understand.*“ Das Prinzip des „Verstehens durch Aufbauen“ kann auch auf den Kontext von enzymatischen Systemen angewandt werden. Ein solches Aufbauen erfordert Bausteine

mit gutmütigen Eigenschaften. Ihre Funktion sollte beobachtbar sein, die Bausteine kompatibel und ihre Komplexität gering genug, um auch in einem komplexen Gesamtsystem eindeutige Schlüsse zuzulassen. Beispielsweise erzeugen auf fluorogenen Substraten beruhende Enzymassays in Einzelmolekülexperimenten Datensätze, deren Auswertung sich als extrem schwierig erweisen können (10). Auf der anderen Seite ist die Verwendung von fluorogenen Substraten wünschenswert, da ein exzellentes Signal/Rauschen-Verhältnis die Messung von falsch-positiven Ereignissen verhindern kann. Bausteine wie Aptamere, die Farbstoffe erkennen und beim Binden deren Quanteneffizienz um drei Größenordnungen steigern, sind bekannt (11, 12) und erscheinen aufgrund ihrer Komposition und Struktur hinreichend robust. Die Einsetzbarkeit solcher RNA-Strukturen zum Auslesen einer neu geschaffenen Funktion in Systemen, die aus mehreren Komponenten zusammengesetzt wurden, ist in dieser Arbeit gezeigt worden. Das dabei zur Verfügung gestellte Signal/Rauschen reicht aus, so dass damit auch eine Grundlage für die Verwendung als Signalkomplex in Studien an Enzymen und Enzymnetzwerken geschaffen wurde.

Der Aufbau von Modellsystemen erfordert neben der zeitlichen Kontrolle der Funktion auch eine präzise Kontrolle über die Position der Komponenten. Das Erzeugen von Strukturen aus atomaren Komponenten auf Oberflächen und der Nachweis von neuen, sich aus der Struktur ergebenden Eigenschaften war schon in den 1990er Jahren durch die Arbeit von Don Eigler und seinen Kollegen möglich geworden (13). Unter physiologischen Bedingungen, wie sie für biologische Proben notwendig sind, ist der kontrollierbare Aufbau kleiner Systeme aus molekularen Komponenten jedoch erst vor kurzem trotz und auch aufgrund der von Smalley im Streit mit Drexler angeführten „Klebrigkeit“ des Manipulators möglich geworden (14). Durch die Kombination der Positionierungspräzision eines AFMs mit dem selektiven Hybridisierungsverhalten von DNA-Molekülen konnte mit SMC&P eine Methode zur Oberflächen-Assemblierung einzelner Moleküle etabliert werden (15). Für die Studie von einzelnen Enzymen in Netzwerken kann sie Verwendung finden, um Proteinkomponenten relativ zueinander anzuordnen. Darüber hinaus kann die Positionskontrolle auch für die Studie von Einzelmolekülen überaus hilfreich sein. In *zero-mode waveguides* (Nullmoden-Wellenleitern) beispielsweise, die eine erhebliche Verbesserung des Signal/Rauschen ermöglichen, ist unter Umständen eine Vergleichbarkeit der zu untersuchenden Moleküle nur dann gewährleistet, wenn durch die Metallwand induzierte Randeffekte keine Rolle spielen. Die im Rahmen dieser Arbeit entwickelten Methoden, Proteine mit mechanischer Kontrolle in einem Konstruktionsbereich zusammenzuführen und beliebige

Arrangements zusammenzustellen, stellen eine sehr große Kontrolle über die Proteinpositionen zur Verfügung.

Die in dieser Dissertation vorgestellten neuen Methoden und Experimente beschäftigen sich hauptsächlich mit der räumlichen Kontrolle von einzelnen, biologischen Molekülen, DNA, RNA und Proteinen. Die Schaffung von neuer Funktion durch das Zusammenspiel zweier molekularer Komponenten, das durch ihre präzise Anordnung ermöglicht wurde, ist demonstriert worden. Die Erkenntnisse können nun dazu verwendet werden, um räumliche und zeitliche Kontrolle über kleine, enzymatische Systeme und ihre Aktivität zu erlangen. Stochastizität und Gesetzmäßigkeiten, die das Verhalten dieser Systeme prägen, werden somit zugänglich gemacht.

Grundlagen

Um die Arbeitsweise von biologischen Molekülen zu verstehen, reicht es durchaus nicht immer aus, Ensemblemessungen auszuwerten. Beispielsweise können bei enzymatischen Reaktionen zwar in vielen Fällen die Michaelis-Menten-Konstante K_m und die maximale Reaktionsrate v_{max} bestimmt und zur Beschreibung der Reaktion herangezogen werden, individuelle Abläufe und Fluktuationen der molekularen Eigenschaften werden aber so nicht erkenntlich. An dieser Stelle können Einzelmolekülmessungen es dem Wissenschaftler ermöglichen, genauere Einblicke zu erhalten. Lange Zeit war zum Beispiel unbekannt, ob sich das Motorprotein Myosin V in einem Hand-über-Hand-Mechanismus an Aktinfilamenten entlang bewegt oder eher wie eine Raupe. Diese Fragestellung konnte 2003 durch Yildiz et al. (16) beantwortet werden, indem einzelne assymetrisch mit Farbstoff markierte Motorproteine beobachtet wurden. Die Positionen der einzelnen Farbstoffmoleküle konnten zeitaufgelöst auf wenige Nanometer genau bestimmt werden, wodurch offenbar wurde, dass sich das Molekül in einem Hand-über-Hand-Mechanismus vorwärtsbewegt. Ebenfalls ersichtlich wurde auch die Verteilung der Wartezeiten zwischen zwei Schritten. Das Beispiel macht ersichtlich, dass durch den *Einzelmolekül-Ansatz* Wahrscheinlichkeitsverteilungen von molekularen Eigenschaften und Verhaltensweisen zugänglich gemacht werden können. Die in der vorliegenden Arbeit verwendeten Methoden zur Messung von Einzelmolekülen sollen im Folgenden kurz beschrieben werden.

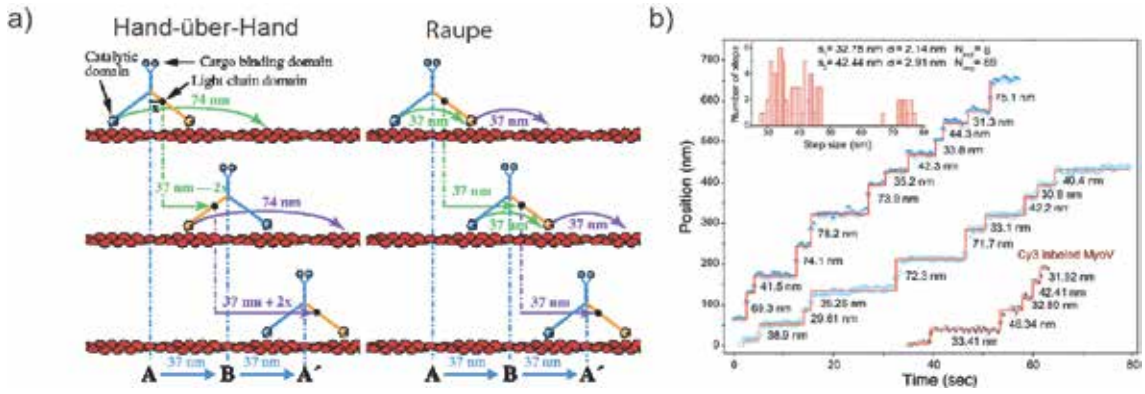

Fig. 1 Lange Zeit stand die Frage im Raum, durch was für einen Mechanismus sich Myosin V eigentlich bewegt (a). Die Auswertung von Einzelmolekülexperimenten konnte hier Aufschluss geben, indem Schrittweiten asymetrisch gelabelter Myosine bestimmt wurden (b). Nach (16). *Reprinted with full permission from AAAS.*

Einzelmolekül-Fluoreszenzspektroskopie

Die Anfänge der optischen Beobachtung einzelner Moleküle kann man in den 70er Jahren des 20. Jh. finden. Bereits damals konnten Hirschfeld et al. einzelne Antikörper mit Hilfe vieler Fluorophore sichtbar machen (17). Die tatsächliche Beobachtung eines einzelnen Farbstoffs gelang aber erst Mörner und Kador (18), wohingegen Keller et al. einzelne Fluorophore in einer biologisch relevanten Umgebung messen konnten (19). Einzelmolekül-Fluoreszenzmessungen sind heute ein häufig genutztes, wissenschaftliches Werkzeug. Wichtigste Voraussetzung ist hier, dass das Molekül genügend Photonen emittiert, um ein möglichst günstiges Verhältnis von Signal zu Hintergrund zu gewährleisten. Durch Einschränkung des Anregungsvolumens kann dies erreicht werden. Methoden wie konfokale Mikroskopie (20) oder TIRF-Mikroskopie (21) ermöglichen dies ohne die beobachtbare Fläche zu verkleinern. Die Verwendung von zero-mode waveguides (ZMW) (22) hingegen ermöglicht die alleinige Anregung von zeptoliter-Volumina. Die beobachtbare Fläche ist hier allerdings durch die ZMW selbst begrenzt.

TIRF-Mikroskopie

Im Rahmen dieser Arbeit wurden Fluoreszenzaufnahmen von Biomolekülen vor allem mit dem TIRF-Mikroskop (*total internal reflection fluorescence microscopy,* TIRFM) gemacht. Bei dieser Technik wird im Weitfeld eine Fläche evaneszent mit Laserlicht angeregt. Der Laser wird hierfür unter einem Winkel, bei dem Totalreflexion auftritt, auf die Glas-Wasser-Grenzfläche gerichtet. Der kritische Winkel, bei dessen Überschreitung Totalreflexion auftritt, ist durch $\alpha_c = \arcsin\left(\frac{n_2}{n_1}\right)$ gegeben, wobei für die Brechungsindizes gilt, dass $n_2<n_1$. Unter diesen Bedingungen bildet sich an der Glas-Wasser-Grenzfläche ein evaneszentes Feld aus. Die transmittierte Intensität nimmt mit zunehmendem Abstand von der Grenzfläche exponentiell ab. Es gilt

$$I(z) = I_0 e^{-\frac{z}{d}}$$

wobei die Eindringtiefe *d* gegeben ist durch

$$d = \frac{\lambda_t}{4\pi\sqrt{n_1^2 \sin^2 \alpha - n_2^2}}.$$

Dies ermöglicht es, nur die Moleküle im Probenvolumen anzuregen und zu detektieren, die sich im Bereich einiger hundert Nanometer von der Grenzfläche befinden.

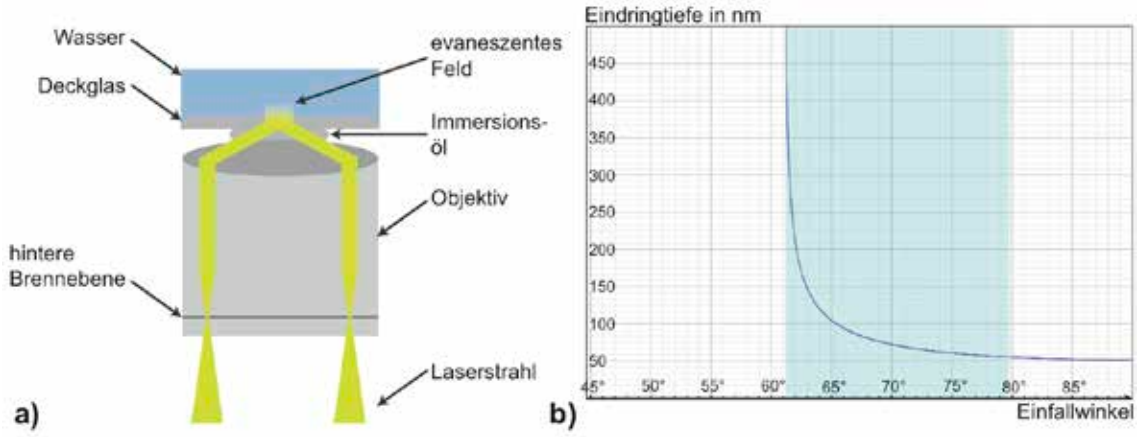

Fig. 2 a) Objective-Type TIRF. Bei genügend großer NA des Objektivs kann ein Laser, der in die hintere Brennebene des Objektivs fokussiert wird, unter einem so großen Winkel austreten, dass Totalreflexion an der Deckglas-Wasser-Grenzschicht auftritt. b) Die Eindringtiefe des evaneszenten Felds in Abhängigkeit von Einfallwinkel. In blau ist der Winkelbereich markiert, in dem durch ein Objektiv mit NA 1.49 Totalreflexion auftritt.

Die Einkopplung des Lasers kann über ein Prisma erfolgen, wobei die Anregung des Probenvolumens durch das Prisma, die Beobachtung dann aber von der entgegengesetzten Seite erfolgt. Bei dieser Realisierung ist also die Oberfläche nicht für eine mechanische Handhabung zum Beispiel durch ein AFM zugänglich. Eine andere Möglichkeit besteht darin, den Anregungsstrahl durch das Objektiv, durch das auch die Detektion erfolgt, in die Probe einzukoppeln (23). Dies ist möglich, wenn die Numerische Apertur des Objektivs so groß ist, dass ein parallel zur optischen Achse verlaufender, aber seitlich versetzter Laserstrahl unter einem Winkel aus dem Objektiv tritt, der größer als der kritische Winkel α_c ist. Bei dieser Realisierung bleibt der obere Halbraum für Manipulationen durch das AFM zugänglich.

Nanometergenaue Lokalisierung von Einzelmolekülen

In der optischen Mikroskopie wird die beugungsbegrenzte Auflösungsgrenze, also der Abstand zweier punktförmiger Lichtquellen, die bei konventioneller Mikroskopie noch voneinander getrennt werden können, gerne durch das Rayleigh-Kriterium beschrieben:

$$r = \frac{0{,}61 \cdot \lambda}{NA}$$

Dies reflektiert die Tatsache, dass das Bild einer Punktlichtquelle, welches von einer begrenzten Optik erzeugt wird, ein Airy-Scheibchen umgeben von Beugungsringen ist. Die Intensitätsverteilung folgt der Funktion

$$psf(r) = \left(\frac{2J_1(ra)}{r} \right)^2,$$

wobei $a = \frac{2\pi NA}{\lambda}$ und $J_1(x)$ die Besselfunktion 1. Ordnung ist (24). Im Zentrum des zentralen Maximums (Airy-Scheibchen) befindet sich die Punktlichtquelle. Es hat sich als ausreichend erwiesen, die Intensitätsverteilung mit einer 2-dimensionalen Gaussfunktion anzufitten, um das Zentrum der Verteilung festzustellen. In Abhängigkeit von Größen wie Standardabweichung der Intensitätsverteilung, Pixelgröße, Hintergrundrauschen und der Anzahl der Photonen kann die Position einer Punktlichtquelle (wie etwa die eines einzelnen, fluoreszierenden Moleküls) festgestellt werden (25). De facto ist eine Bestimmung der Position eines einzelnen Farbstoffmoleküls mit einer Präzision von unter einem Nanometer bei genügend großer Photonenausbeute möglich (26).

Auf der Grundlage dieses Prinzips sind hochauflösende Mikroskopiemethoden entwickelt worden. Lassen sich in einer Aufnahme die Fluoreszenzverteilungen der leuchtenden Fluorophore voneinander trennen, dann können deren Positionen mit großer Genauigkeit bestimmt werden. Methoden wie PALM (27), FPALM (28), STORM (29) und BLINKM (30) beruhen darauf, stochastisch nur so wenige Moleküle in den fluoreszenten Zustand zu versetzen, dass die Fluorophore in einem Bild getrennt voneinander lokalisiert werden können. Das „Schalten“ erfolgt dabei durch Photoaktivierung oder chemische Reaktionen. Vielfach wiederholte Aufnahmen erlauben bei Anwendung dieses Prinzips die Rekonstruktion eines Bildes der Probe. Von den genannten Methoden unterscheidet sich STED-Mikroskopie (31). Hier werden durch einen fokussierten Laserstrahl über die gesamte Fokus-Breite Moleküle angeregt. Ein zweiter Strahl mit einem Donut-förmigen Fokusprofil induziert um das Zentrum des ersten Strahls eine stimulierte Emission, so dass nur im Zentrum Moleküle angeregt bleiben, die durch spontane Fluoreszenz in den Grundzustand zurückkehren. Der Bereich, aus dem spontane Fluoreszenz gemessen werden kann, ist deutlich kleiner als die Rayleighsche Auflösungsgrenze.

Einzelmolekül-Kraftspektroskopie

Kraftspektroskopie an Molekülen wird im Allgemeinen vorgenommen, indem man das zu untersuchende Molekül zwischen einer festen Oberfläche und einem Kraftsensor einspannt. Bekannte Systeme, um molekulare Kräfte zu messen, sind magnetische Fallen (32), optische Fallen (33) und das Kraftmikroskop (*atomic force microscope*, AFM) (34). Diese Methoden unterscheiden sich sowohl im ihnen zugänglichen Kraftbereich als auch in ihren jeweiligen Vorteilen. Während mit magnetischen Fallen Kräfte im Bereich 0.01 – 10 pN gemessen werden und mit der optischen Falle Kräfte im Bereich 0.1 – 100 pN, ermöglicht das AFM das Messen von Kräften der Größenordnung von 10 pN bis 100 nN. In magnetischen Fallen kann auch ein Drehmoment an die Probe angelegt werden, die optische Falle hat eine hohe Kraftauflösung und das AFM stellt eine exzellente räumliche Auflösung zur Verfügung (35). Für die im Rahmen dieser Arbeit durchgeführten Experimente wurde ausschließlich das AFM verwendet.

Das Rasterkraftmikroskop (AFM)

Ursprünglich wurde das Rasterkraftmikroskop entwickelt, um Oberflächentopographien aufzunehmen. Mit einer an einer Blattfeder (Cantilever) befestigten, atomar spitzen Nadel kann hierfür die Oberfläche abgerastert werden. Die dabei zwischen den Atomen der Oberfläche und der Nadel auftretenden Kräfte führen zu einer Verbiegung der Blattfeder, die registriert wird. Für kleine Auslenkungen verhält sich die Blattfeder wie eine Hook'sche Feder. Ist die Federkonstante k_F bekannt, kann also aufgrund der gemessenen Auslenkung die verursachende Kraft

$$F = k_F \cdot \Delta x$$

berechnet werden. Die Auslenkung der Blattfeder lässt sich präzise mit Hilfe des Lichtzeigerprinzips messen (36). Ein Laserstrahl wird auf die reflektierende Blattfeder fokussiert, der reflektierte Strahl fällt dann auf eine segmentierte Photodiode. Die Differenz der auf den einzelnen Segmenten gemessenen Spannungen kann zur Bestimmung der Auslenkung des Cantilevers herangezogen werden. Sowohl zum Ansteuern eines Punktes auf der Oberfläche als auch zum Einstellen der Position des Cantilevers über der Oberfläche werden Piezosysteme verwendet, die eine Ångström-genaue Positionierung erlauben.

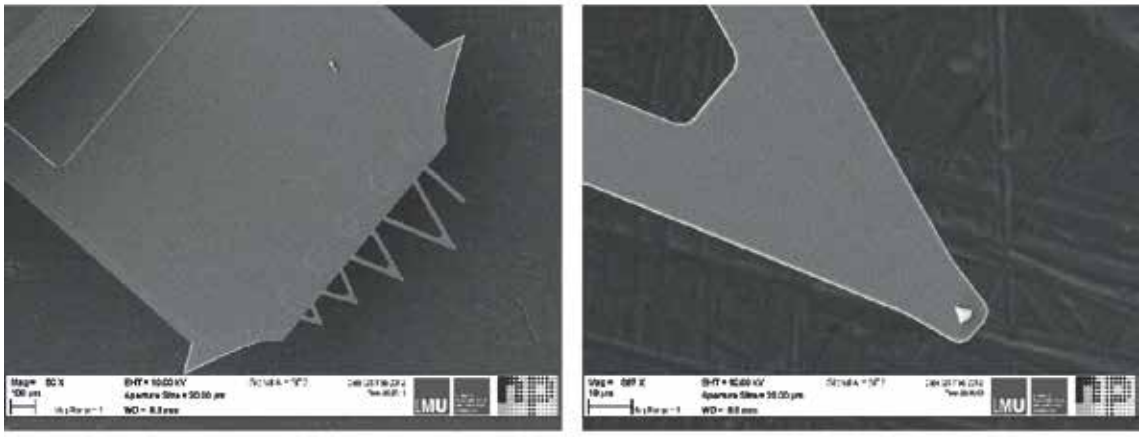

Fig. 3 Elektronenmikroskopische Aufnahme von Cantilevern in verschiedenen Vergrößerungen. Links: MSCT-Cantilever (Brooker) an einem Chip. Rechts: Am Ende des Cantilevers ist die Spitze erkennbar. Die Bilder wurden S. Heucke zur Verfügung gestellt.

Das AFM kann als Kraftmikroskop zur kraftspektroskopischen Untersuchung einzelner Moleküle verwendet werden. Die Moleküle werden hierfür zwischen der Cantileverspitze und der Oberfläche eingespannt. Wenn der Cantilever von der Oberfläche entfernt wird, wird eine Kraft an das Molekül angelegt, die über die Verbiegung des Cantilevers vermessen wird. Wird die gemessene Kraft über den Abstand aufgetragen, so ist es möglich, Wechselwirkungen innerhalb eines Moleküls oder auch zwischen verschiedenen Molekülen zu interpretieren wie z.B. in (37).

Auflösbarkeit von Kräften

Näherungsweise kann der Cantilever als harmonischer Oszillator betrachtet werden. Nach dem Equipartitionstheorem steht dem System pro Freiheitsgrad die Energie ½k_BT zur Verfügung. Für die von der Feder thermisch aufgenommene Energie gilt also:

$$\frac{1}{2} k_F \langle \Delta x^2 \rangle = \frac{1}{2} k_B T$$

Daraus ergibt sich zum einen, dass das mittlere, quadratische Auslenkungsrauschen proportional zur Temperatur und umgekehrt proportional zur Federkonstante ist. Das mittlere, quadratische Kraftrauschen hingegen ist proportional zur Federkonstante und zur Temperatur.

$$\left\langle \Delta x^2 \right\rangle = \frac{k_B T}{k_F}$$
$$\left\langle \Delta F^2 \right\rangle = k_F \cdot k_B T$$

Ein häufig verwendeter Lever ist der Bruker MLCT D-Lever. Dieser weist typischerweise eine Federkonstante von 15 pN/nm auf. Die einfache Rechnung ergibt ein Kraftrauschen von $\sqrt{\left\langle \Delta F^2 \right\rangle} \cong 8pN$.

Eine genauere Betrachtung findet sich in (38). Die kleinste auflösbare Kraft ist hier gegeben durch

$$F_{\min} = \sqrt{4k_B TRB},$$

wobei B die Bandweite der Messung und R die viskose Dämpfung ist. Es zeigt sich, dass bei konstanter Bandweite und Temperatur nur eine geringere, viskose Dämpfung kleinere Kräfte detektierbar macht. Dies kann z.B. durch kleinere Cantilever erreicht werden.

Molekulare Wechselwirkungen

DNA

Bekannt ist DNA vor allem als Träger der genetischen Information. Genau aus diesem Grund gilt es auch als eines der wichtigsten Moleküle in der Zelle. Da die Folge einer chemischen Veränderung oder eines strukturellen Fehlers tödlich für die Zelle sein kann, muss sich dieses Molekül durch Robustheit, Einfachheit und Spezifizität seiner Wechselwirkungen auszeichnen. Die vier Basen Adenosin (A), Cytosin (C), Guanosin (G) und Thymin (T) sind über ihre Zucker (Desoxyribose) und Phosphatreste miteinander kovalent zu Polymeren verbunden. Wie J. Watson und F. Crick 1953 nachweisen konnten, sind zwei DNA-Stränge normalerweise in einer Doppelhelix organisiert (39). Für Stabilität sorgen die sich zwischen gegenüberliegenden Basen A-T und G-C bildenden Basenpaarungen, die aufgrund von Wasserstoffbrücken auftreten, und das sogenannte *base stacking* (40). Liegen Basen gegenüber, die eine Basenpaarung nicht erlauben, wird die Hybridisierung destabilisiert. Je vollständiger also die Komplementarität der DNA-

Sequenzen ist, desto stabiler wird auch die Wechselwirkung. Die Stränge sind gegenläufig, d.h. das 5'-Ende eines Stranges liegt dem 3' Ende des anderen gegenüber.

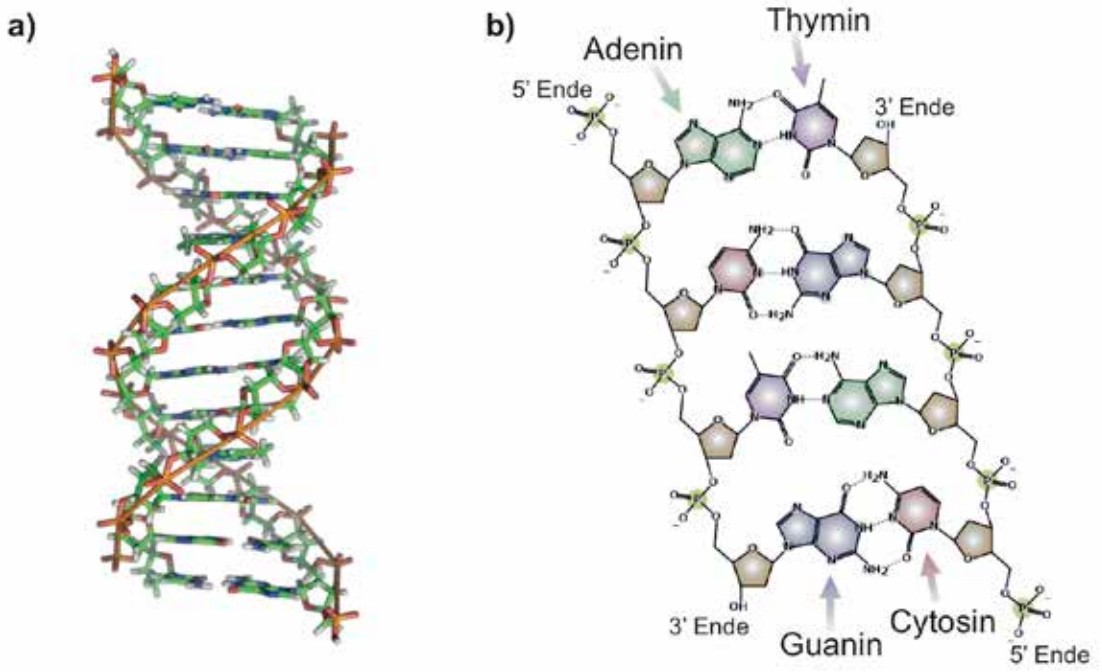

Fig. 4 a) B-DNA. Komplementäre DNA Stränge hybridisieren zu einer doppelhelikalen Struktur, die durch base stacking und Basenpaarungen stabilisiert wird. b) Kanonische Basenpaarungen bilden sich aufgrund von Wasserstoffbrücken zwischen Adenin und Thymin, Guanin und Cytosin aus. Nach (41).

DNA als programmierbarer Baustein für SMC&P

Wegen der stark sequenzspezifischen Wechselwirkung zwischen zwei Strängen wird DNA in der Nanotechnologie gerne als programmierbarer Baustein genutzt. Die Tatsache, dass Doppelstränge sich sequenzspezifisch und vorzugsweise so ausbilden, dass Basenpaarungen über die gesamte Länge der Hybridisierung auftreten, hat z.B. die Schaffung künstlicher, zwei- oder dreidimensionaler Objekte wie Origamis (42, 43) oder sogenannter *tensegrity structures* (44) ermöglicht. Der Aufbau solcher nanoskaligen Strukturen erfolgt selbstorganisierend (*self-assembly*). Die Kontrolle über die Position der Moleküle beschränkt sich auf die Größe der Strukturen. Eine weitere Möglichkeit, nanoskalige Strukturen aufzubauen, ist durch die Single-Molecule Cut&Paste Technik (SMC&P) ermöglicht worden (15). Hier werden die mechanischen Eigenschaften von DNA genutzt, um ein hierarchisches Kraftsystem zu schaffen. Das Schmelzverhalten von DNA unter Kraft ist stark abhängig von der Geometrie, unter der die Kraft auf die DNA wirkt. Eine Möglichkeit ist es an beiden Stränge am gleichen Ende, also entweder am 5'- oder am 3'-Ende zu ziehen, also in Scher-Geometrie. In diesem Fall ist die Kraft parallel zur Längsachse des Doppelstrangs gerichtet, so dass zunächst eine Streckung in diese

Richtung erfolgt. Alle Basen werden hier gleichmäßig belastet und die Abrisskraft hängt in diesem Fall von der Anzahl der Basen und der Kraftladungsrate ab (45). Auch die Befestigung der DNA entweder am 3'- oder 5'-Ende spielt hier eine Rolle, da durch die Helizität der DNA jeweils verschiedene Pfade durch die Energielandschaft durchlaufen werden (46). Anders verhält es sich, wenn die Kraft am 3'-Ende des einen Strangs und am 5'-Ende des anderen Strangs angelegt wird (*unzip*-Geometrie). Die Kraft ist hier senkrecht zur DNA-Längsachse angelegt, wodurch jede Basenpaarung einzeln belastet wird. Die Kräfte zum Öffnen der Hybridisierung bei dieser Geometrie sind kaum von der Kraftladungsrate abhängig. Sie liegen in der Regel zwischen 15 und 25 pN in Abhängigkeit vom Anteil an G-C oder A-T (47, 48).

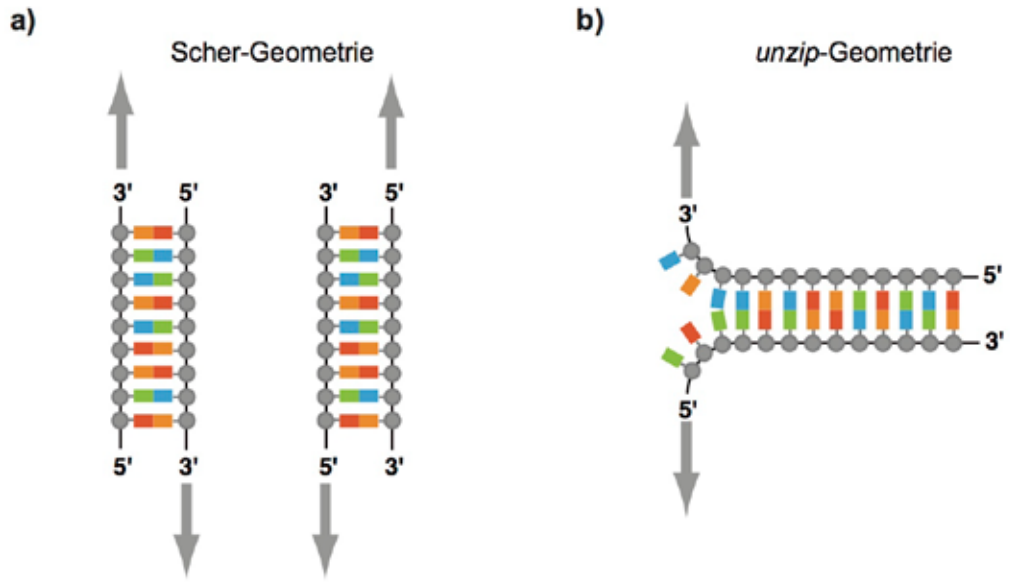

Fig. 5 Kraftinduziertes Schmelzen doppelsträngiger DNA. Zwei Belastungsgeometrien, die zum Aufbrechen der Hybridisierung führen, sind a) die Schergeometrie und b) die *unzip*-Geometrie. In der Schergeometrie hängt die Abrisskraft von der Anzahl der Basen, der Kraftladungsrate und der Befestigung der DNA ab. In der *unzip*-Geometrie betragen die Kräfte zum Öffnen der Hybridisierung abhängig vom Anteil von G-C und A-T Basenpaarungen 15-25 pN.

Ein hierarchisches Kraftsystem und Single-Molecule Cut-and-Paste

Auf der Grundlage der eben beschriebenen Möglichkeiten, mechanisch ein Aufschmelzen von doppelsträngiger DNA zu induzieren, lässt sich ein hierarchisches Kraftsystem aufbauen, das ein „Ausschneiden" und „Einsetzen" (Cut&Paste) von DNA-Molekülen zulässt. Hierfür wird eine Oberfläche in einen Depot- und einen Zielbereich unterteilt. An eine kovalent am 5'-Ende in der Depotregion befestigte DNA, den *Ankerstrang*, wird eine *Transfer-Strang* genannte DNA über eine ca. 30 bp lange Sequenz hybridisiert. Diese besitzt an ihrem 3'-Ende eine freie, einzelsträngige Teilsequenz. Komplementär zu dieser ist die Sequenz eines Oligomers, *AFM-Strang* genannt, die am 5'-Ende kovalent an die

Spitze eines AFM-Cantilevers gebunden ist. Wird die Spitze mit der Oberfläche im Depotgebiet in Kontakt gebracht, dann hybridisiert die AFM-Sequenz über ca. 20 bp an den Überhang des Transferstrangs. Wenn nun der Cantilever wieder von der Oberfläche entfernt wird, baut sich eine Kraft auf, und beide Bindungen werden sequenziell belastet: Die Bindung zum Ankerstrang wird in der unzip-Geometrie, die Bindung zum AFM-Strang hingegen in Scher-Geometrie aufgebaut. Die Abrisskräfte sind von der Belastungsgeometrie abhängig. Obwohl die 30 bp lange Bindung zum Ankerstrang thermodynamisch stabiler ist als die zum AFM-Strang, öffnet sie sich schon bei 20 pN, wohingegen die Bindung zum AFM-Strang noch stabil ist. Der Transferstrang ist nun an die Cantileverspitze gebunden und kann mit Hilfe eines Piezosystems nanometergenau in die Zielregion gebracht werden. Dort ist die Ankersequenz kovalent mit ihrem 3'-Ende an der Oberfläche verbunden. Wenn die AFM-Spitze nun auf die Oberfläche gebracht wird, hybridisiert der Transferstrang an die Ankersequenz. Beim Zurückziehen des Cantilevers werden diesmal beide Bindungen, die zum Ankerstrang und die zum AFM-Strang, in Schergeometrie belastet. Da aber die Hybridisierung an den Ankerstrang über 30 Basenpaare erfolgt, die an den AFM-Strang aber nur über 20 Basenpaare, ist diesmal die Bindung zum AFM-Strang instabiler. Sie reißt bei etwa 50 pN. Die Cantileverspitze ist nun wieder frei von Transfer-DNA und kann für den nächsten Transferzyklus eingesetzt werden.

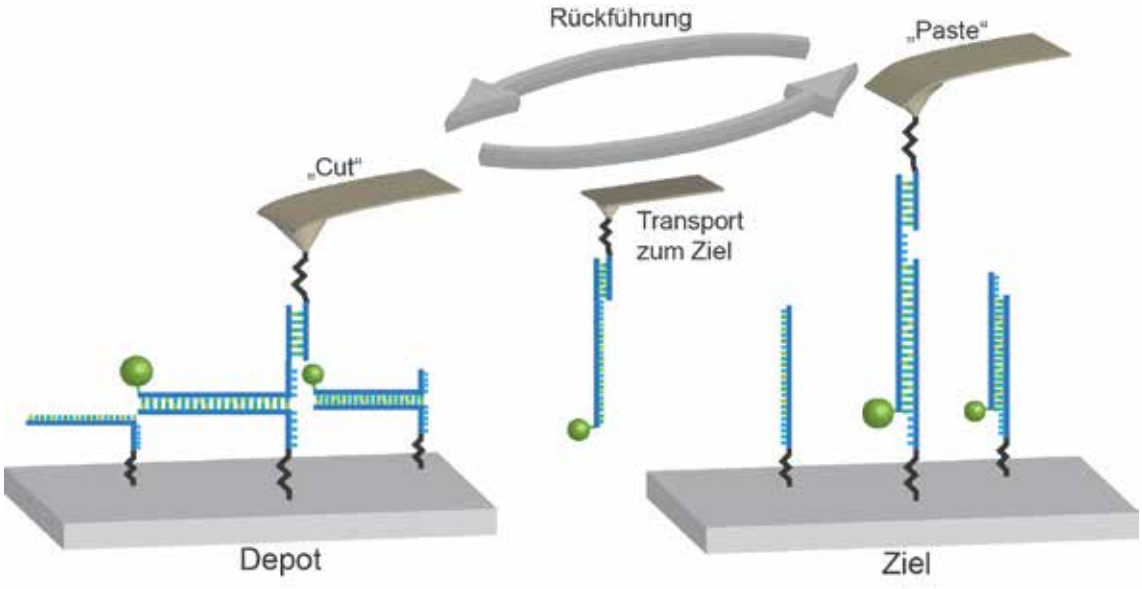

Fig. 6 Der DNA-basierte SMC&P Prozess. Im Depot werden gelabelte Transferstränge an Ankerstränge hybridisiert. Unter Ausnutzung des hierarchischen Kraftsystems können Moleküle im Depot ausgeschnitten („Cut") und ins Ziel transportiert werden. Dort werden sie eingesetzt („Paste") und die leere Cantileverspitze wird am Ende des Zyklus zum Depot zurückgeführt.

Single-Chain Antikörper Fragment

Die im vorangehenden Abschnitt beschriebene SMC&P Technik beruht im Wesentlichen auf einem hierarchischen Kraftsystem. Obwohl die erste Realisierung durch Ausnützen der Wechselwirkungen zwischen DNA-Strängen gezeigt wurde, ist eine Einbeziehung von anderen molekularen Wechselwirkungen möglich und im Rahmen der vorliegenden Arbeit gezeigt worden (Publikation 5). Hierfür wurde eine Antikörper-Antigen-Wechselwirkung genutzt. Die gemeinhin bekannte Y-förmige Gestalt eines Antikörpers setzt sich aus zwei schweren Ketten und zwei leichten Ketten zusammen, wobei die schweren Ketten miteinander durch Disulfidbrücken verbunden sind und ebenfalls über Disulfidbrücken je eine leichte an eine schwere Kette bindet. Die variablen Domänen befinden sich an den N-Termini der schweren und der leichten Kette. Dort wird das spezifische Bindungsverhalten des Antikörpers ausgebildet. Diese Domänen bilden das Fv-Fragment, das somit die kleinste Antigen-bindende Einheit bildet. Im single-chain Fv - Fragment (scFv) werden die Domänen der schweren und der leichten Kette, die das Fv-Fragment ausmachen, durch einen Peptidlinker verbunden. Dieses Protein bildet dann eine stabile und kleine Einheit. Für kraftspektroskopische Experimente ist es ideal, da auf diese Weise die Möglichkeiten für unspezifische Wechselwirkungen reduziert sind. Antigene, die nur aus einem kleinen Peptid bestehen, sind in diesem Zusammenhang besonders interessant, da sie an das zu untersuchende Protein fusioniert werden können, ohne dass sie das Verhalten des Proteins deutlich beinflussen. Auf diese Weise kann die Bindung zwischen scFv und Antigen als kraftspektrosopische Sollbruchstelle benutzt werden, die zu einem gewissen Grad Kraftspektroskopie am Protein erlaubt, auf der anderen Seite aber aufbricht, bevor das Protein zerstört wird. Genauere Untersuchungen zum Bindungsverhalten des in dieser Arbeit benutzten C11L34 scFv und des 12 aa langen GCN4 Peptids unter Krafteinwirkung finden sich in (49). Die Kristallstrukturdaten sind aus (50) bekannt. Das Peptid bildet an des scFv gebunden eine α-helikale Struktur aus, nicht im Komplex verhält es sich wie ein statistisches Knäuel.

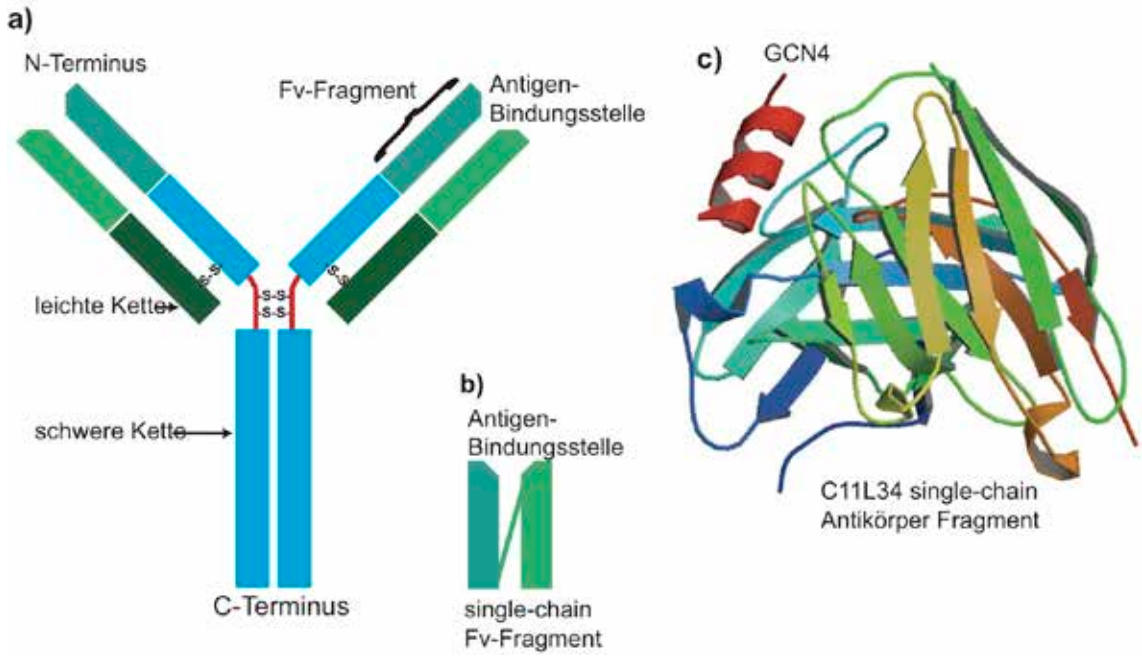

Fig. 7 a) Skizze eines IgG-Antikörpers. b) Die kleinste Einheit, die das Antigen erkennt, wird durch das Fv-Fragment gebildet. Dessen Domänen können durch einen Peptid-Linker verbunden werden, um ein single-chain Fv-Fragment (scFv) zu erhalten. c) Die Kristallstruktur des scFv C11L34. In rot ist das gebundene GCN4-Peptid erkennbar (PDB 1P4B).

Zinkfinger – DNA Wechselwirkung

Unter den DNA-bindenden Proteinen gehören Zinkfinger zu den am stärksten in der Natur verbreiteten. Sie treten als Transkriptionsfaktoren auf und unter ihnen ist der Cys_2His_2-Typ am besten charakterisiert. Man findet ihn in den Genomen verschiedenster Organismen – von dem der Hefe bis hin zum menschlichen, wo er immerhin 3% der Gene ausmacht (51). Charakteristisch für Cys_2His_2–Zinkfinger ist die aus zwei β-Faltblättern und einer α-Helix bestehende Struktur, die durch ein zwischen zwei Histidine und zwei Cysteine gebundenes Zink-Ion stabilisiert wird. Für die Erkennung von DNA-Sequenzen ist hauptsächlich die α-Helix verantwortlich. Sie bindet in die *major groove* der DNA. Die drei Aminosäuren an den helikalen Positionen -1, 3 und 6 bilden dort spezifisch Wasserstoffbrückenbindungen zu drei aufeinander folgenden Basen an einem Strang aus (52) und es existiert noch eine weitere Wechselwirkung durch eine vierte Aminosäure in der α-Helix (helikale Position 2) zu einer Base des Komplementärstrangs (53). Die DNA wird beim Binden des Zinkfingers verformt. Die Rotation der Doppelhelix weicht bei dieser Wechselwirkung von den typischen 36 ° Schritten ab. Die Wechselwirkung zwischen Zinkfingern und DNA ist soweit verstanden, dass durch Mutation der entsprechenden Aminosäuren spezifische Bindungen zu einer Vielzahl von Basentripletts hergestellt werden können. Außerdem können durch Kombination verschiedener Zinkfinger-Module längere Zielsequenzen erkannt werden. Kombinationen solcher

Aneinanderreihungen mit Nukleasen sind kommerziell verfügbar und können u.a. zur Manipulation von Genomen herangezogen werden (54). Im Rahmen dieser Arbeit wurde ein 6-Zinkfinger-Konstrukt (Zif268-NRE) genutzt, das spezifisch und mit einer sub-picomolaren Affinität eine DNA-Sequenz bindet (55), um stabile DNA-Protein-Komplexe herzustellen. Mit Hilfe dieser Komplexe konnte die Verwendbarkeit von SMC&P zur Schaffung von funktionalen Proteinarrangements gezeigt werden.

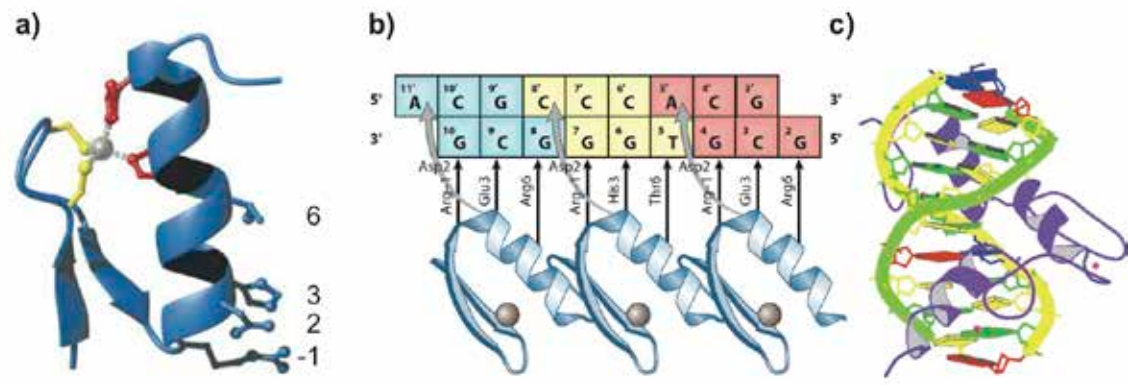

Fig. 8 a) Für die Struktur eines Cys_2His_2-Zinkfingers sind zwei β-Faltblätter und eine α-Helix sowie das zwischen zwei Cysteinen und zwei Histidinen gebundene Zink-Ion charakteristisch. Die Bindung an die DNA erfolgt über die Aminosäuren an den gekennzeichneten Positionen. Aus (56). b) Zinkfinger binden sequenzspezifisch an Basentripletts. Ein Modularer Aufbau aus mehreren Zinkfingern erlaubt es, längere Sequenzen zu erkennen, und ermöglicht eine Bindung mit höherer Affinität. Aus (51). Kristallstruktur eines Zif268-DNA-Komplexes (PDB 1AAY).

Aptamerische Bindung von Malachit Grün

Ähnlich wie Antikörper haben Aptamere die Fähigkeit, Moleküle zu erkennen und spezifisch zu binden. Dabei handelt es sich zumeist um DNA– oder RNA–Strukturen, die eine dreidimensionale Struktur ausbilden, in die das Target-Molekül bindet. In Form von *Riboswitches* treten Aptamere in der Natur auf und sind vor allem in Bakterien gefunden worden. Sie bieten die Möglichkeit auch auf RNA-Ebene durch Binden eines Liganden die Aktivität eines Gens zu steuern (57). Künstlich werden Aptamere in SELEX-Verfahren (*systematic evolution of ligands by exponential enrichment*) hergestellt (58). Grundlage ist hier die Idee, dass in sehr großen RNA-Bibliotheken die Wahrscheinlichkeit groß ist, eine Sequenz zu finden, die in der Lage ist, in eine Struktur zu falten, die ein bestimmtes Target-Molekül bindet. Diese Moleküle werden *in vitro* kompetitiv in automatisierten Verfahren angereichert und identifiziert. Anwendungsmöglichkeiten von Aptameren liegen vor allem in Methoden zur Proteinaufreinigung (59), in Diagnoseverfahren (60) und als Biosensor (61). Im Rahmen dieser Arbeit wurde ein RNA-Aptamer verwendet, das den Farbstoff Malachit Grün spezifisch bindet (12). Die Fluoreszenzeigenschaften von Malachit Grün sind stark abhängig von den Freiheitsgraden der Phenylringe (62, 63). Dies führt

dazu, dass die Quanteneffizienz des Farbstoffs in Lösung lediglich $7.9 \cdot 10^{-5}$ beträgt, durch das Binden des Farbstoffs in die Aptamer-Bindungstasche aber um drei Größenordnungen gesteigert wird (64). Strukturdaten des Aptamers sind mit dem analogen Liganden Tetramethylrosamin aufgenommen worden. Die Bindungstasche besteht aus einem asymetrischen *loop*, der durch nichtkanonische Basenpaarungen und *base stacking* stabilisiert wird. Sterische und elektrostatische Komplementarität fügen den Farbstoff als hydrophoben Kern in die Bindungstasche. Wasserstoffbrückenbindungen spielen keine Rolle (65). Das Malachit Grün-Aptamer konnte als DNA Sensor verwendet werden (66), der ein Auflösungvermögen von einer fehlerhaften Basenpaarung hat. Hierfür wurde das Aptamer in zwei Teile geteilt und erst durch Hinzugabe eines Analytstranges zusammengefügt, so dass sich dann das Aptamer formen konnte. Für die vorliegende Arbeit wurde das geteilte Malachit Grün-Aptamer verwendet, um das erste Beispiel einer mechanisch kontrollierten Assemblierung einzelner Moleküle zu einer funktionalen Einheit zu erbringen.

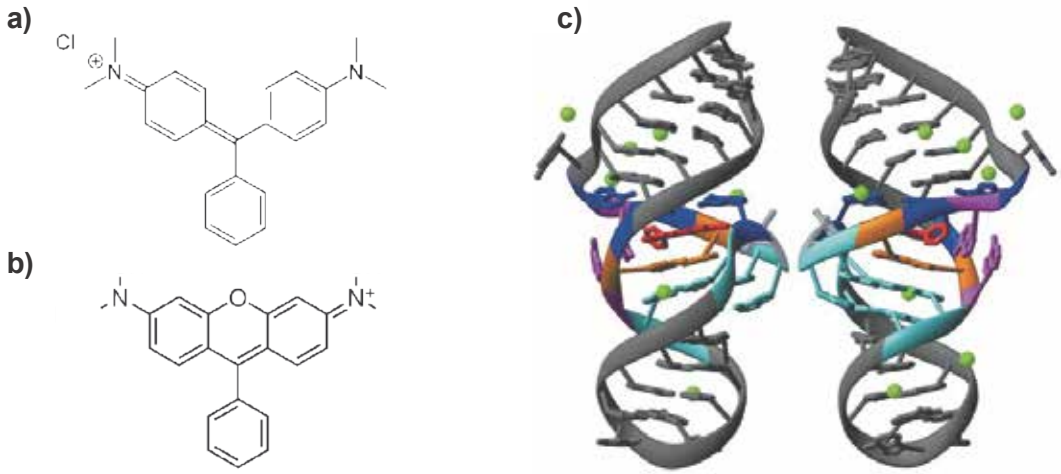

Fig. 9 In a) und b) werden die Farbstoffe Malachit Grün und Tetramethylrosamin gezeigt. Beide Farbstoffe können durch das Malachit Grün-Aptamer gebunden werden. c) Kristallstruktur des Malachit Grün-Aptamer komplexiert mit Tetramethylrosamin aus zwei Perspektiven. Der Farbstoff ist rot dargestellt. Aus (65).

Ergebnisse

Alle Messungen (mit Ausnahme derer in Publikation 4) wurden an einem kombinierten TIRF/AFM-Hybridmikroskop durchgeführt, welches im Detail in Publikation 3 beschrieben ist. Mechanische Vibrationen sowohl des AFM-Kopfes als auch der Probe können die Abrisskräfte beim Öffnen von molekularen Bindungen beeinflussen (67). Das spezielle Design dieses Mikroskops erlaubt eine Reduzierung der mechanischen Vibrationen der Probe. Dies wurde insbesondere durch die starre Kopplung des Objektivs an die Auflagefläche des AFMs erreicht. Somit ist dieses Gerät besonders geeignet für Fluoreszenzspektroskopie am TIRF-Mikroskop und Einzelmolekül-Manipulationen durch das AFM und erlaubt so die nachfolgend beschriebenen Experimente an Einzelmolekülen.

Die Genauigkeit der SMC&P-Technik

Die SMC&P-Technik ermöglicht den molekülweisen Aufbau nanoskaliger Arrangements. Insbesondere die Schaffung maßgeschneiderter, abstandsabhängiger Systeme aus interagierenden Komponenten verlangt eine genaue Kontrolle der Güte der Positionierung. Eine Validierung der Technik ist also notwendig. Die Frage nach der Genauigkeit, mit der ein Molekül positioniert werden kann, nach dem lateralen Fehler, ist also von Bedeutung. Um festzustellen, dass ein *einzelnes* Molekül bei einem Transportvorgang transportiert wird, wurden gleichzeitig die Cantilever-Spitze und die fluoreszenzmarkierte Transfer-DNA beobachtet. Die Beobachtung der Spitze im Fluoreszenzmikroskop ist aufgrund von inelastischer Streuung am Cantilever möglich. Da das Streulicht bei einer anderen Wellenlänge auftritt als die Fluoreszenz des Labels am DNA-Strang, können die Emissionen im Fluoreszenzmikroskop unterschieden werden, wenn das Licht in zwei Farbkanäle aufgeteilt wird. So konnte nach dem Eintreten der Spitze in das evaneszente Feld das Absetzen eines Moleküls *live* beobachtet werden. Der beobachtete einzelne Bleichschritt zeigte, dass in der Tat ein Molekül abgesetzt wurde. Gleichzeitig konnte der Vorgang auch durch Kraftspektroskopie analysiert werden. Der charakteristisch auftretende Einzelabriss in der Kraft-Abstand-Kurve zeigt ebenfalls, dass höchstens ein Molekül transportiert wurde. Der Positionierungsfehler, der beim Absetzen eines Moleküls auftritt, konnte durch Erstellen eines 3x3-Punkte-Musters (50 nm Molekülabstand) und Messen der Abweichung von der anvisierten Position quantifiziert werden. Da die Abstände der Moleküle kleiner waren, als die Abbésche Auflösungsgrenze, wurden die Moleküle durch Anfitten einer Gaussfunktion an ihre Fluoreszenzverteilungen lokalisiert. Diese sind zwar örtlich überlagert, können jedoch zeitlich in der

Fluoreszenzzeitspur durch ihr individuelles, stufenweises Bleichen getrennt werden. Ausgehend davon, dass sich die Fluoreszenzverteilungen vor und nach dem Bleichen eines Farbstoffs gerade um die Fluoreszenzverteilung des gebleichten Farbstoffs unterscheiden und dass sich die Fluoreszenzbeiträge aller Moleküle einfach aufsummieren lassen, kann der Fluoreszenzbeitrag jedes Moleküls rekonstruiert und die Position dieses Moleküls nanometergenau bestimmt werden. Die Positionierungspräzision bei Anwendung der SMC&P-Technik konnte dadurch auf ±11 nm bestimmt werden. Ein einfaches Modell, das Fluktuationen des End-zu-End-Abstands der DNA und des Zuckers, mit dem die DNA an der Oberfläche befestigt ist, als Ursache für den Fehler annimmt, liefert einen übereinstimmenden Wert. Die Ergebnisse dieser Experimente finden sich in Publikation 2.

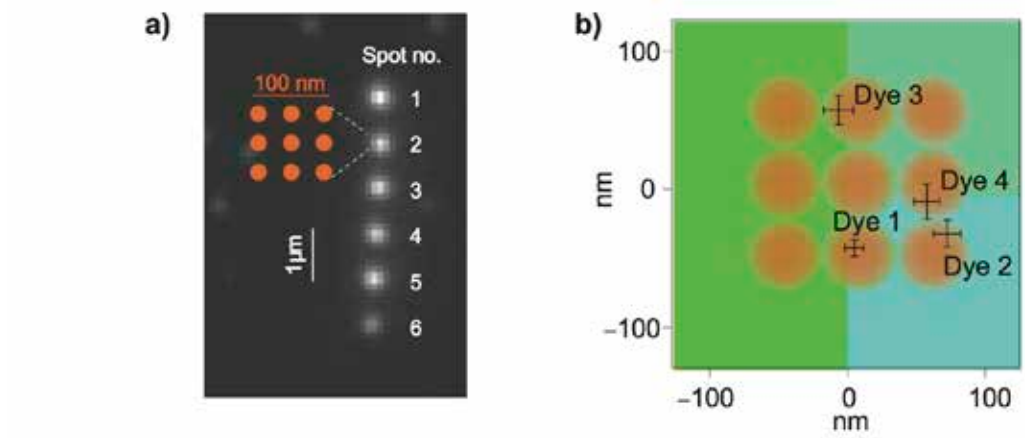

Fig. 10 Ein 3x3 Muster wurde durch SMC&P aus einzelnen Molekülen hergestellt. a) Zeigt sechs solcher Muster im beugungsbegrenzten Fluoreszenzbild. Diese konnten, obwohl sie nur 50 nm voneinander entfernt waren, durch Anwendung einer hochauflösenden Rekonstruktionsmethode getrennt aufgelöst und nanometergenau lokalisiert werden. Die Rekonstruktion der Positionen in b) zeigt in orange das zugrunde gelegte 3x3 Muster. Die Abweichungen der Moleküle sind in der Größenordnung von 10 nm. Nach (68).

Arrangements nanoskaliger Bausteine an Oberflächen

Modellierung und Realisierung von SMC&P beruhten zunächst auf einem hierarchischen Kraftsystem, das nur auf Wechselwirkungen zwischen DNA-Molekülen beruhte. Ein Transport und die Anordung von anderen Objekten als DNA sind ebenfalls möglich und konnten im Rahmen der Arbeit gezeigt werden.

Nachträgliche Anbindung von Nanoskaligen Objekten

Eine Möglichkeit für die Anordnung nanoskaliger Objekte durch SMC&P besteht darin, den Transferstrang mit einer Bindungsstelle auszustatten, die von einem anderen Molekül erkannt wird. Es empfiehlt sich, hierfür einen kleinen Liganden zu wählen, der die Transporteigenschaften der Transfer-DNA nicht beeinflusst. Nach der Anordnung dieser Transfer-Moleküle können dann Rezeptormoleküle oder mit Rezeptormolekülen versehene

Objekte hinzugegeben werden, so dass die Bindungsstellen nachträglich besetzt werden. Mit einer Affinität von 0.1 pM ist die Bindung zwischen Biotin und Streptavidin eine der stärksten und robustesten, nicht-kovalenten, in der Natur vorkommenden Bindungen (69, 70). Entsprechend der beschrieben Methode wurde diese Wechselwirkung zum gezielten Aufbau nanoskaliger Strukturen, die über DNA hinausgehen, genutzt. Es wurden biotinylierte Transfer-Stränge im Zielbereich durch SMC&P angeordnet. Auf diese Weise wurde ein Biotin-Gerüst an der Oberfläche geschaffen, an das dann in einem selbstorganisierten Prozess mit Streptavidin versehene Bausteine binden konnten. Die Durchführbarkeit wurde mit verschiedenen, fluoreszierenden, Strepativin-modifizierten Halbleiter-Nanokristallen (*Quantum Dots*) gezeigt. Diese Experimente werden in Publikation 1 ausführlich beschrieben.

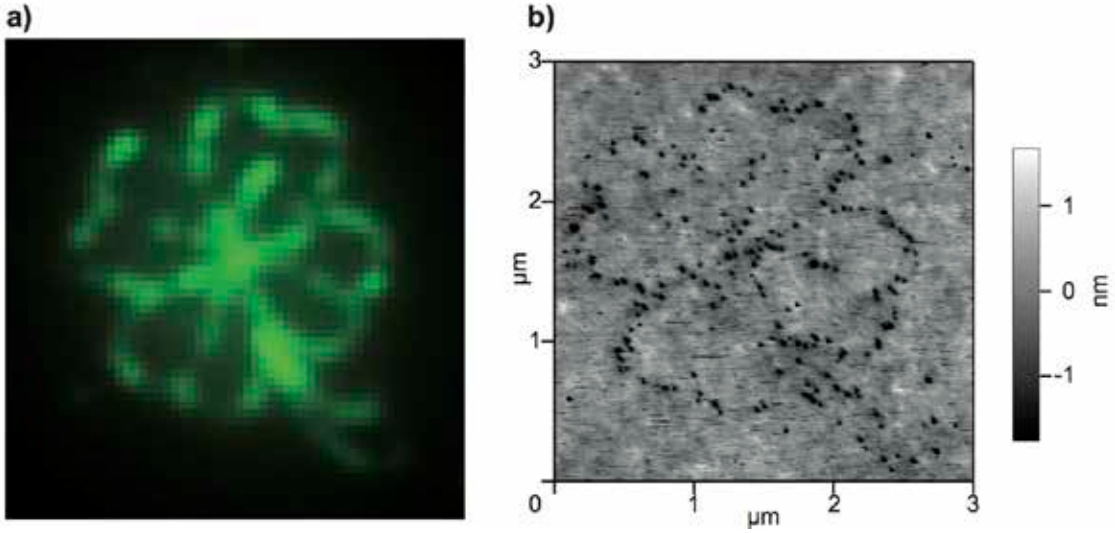

Fig. 11 Für den SMC&P-Transferstrang wurde biotinylierte DNA verwendet. Diese wurde im Zielbereich zu einem Biotingerüst in Form eines Kleeblatts arrangiert. Streptavidin-funktionalisierte, fluoreszierende Halbleiter-Nanopartikel konnten anschließend an die Bindungsstellen binden. Auf diese Weise konnten die Nanopartikel auf die gewünschte Weise angeordnet werden. a) Fluoreszenzbild der an der Oberfläche gebundenen Nanopartikel. b) Diese konnten auch durch das AFM abgebildet werden. Bei dem Scan-Prozess wurden einige Nanopartikel jedoch verschoben. Nach (71).

Direkte Arrangements von Proteinen durch SMC&P

Grundlage der SMC&P-Technik ist die Verwendung eines hierarchischen Kraftsystems. Obwohl die erste Realisierung auf DNA-DNA Wechselwirkungen beruht, die aufgrund verschiedener Belastungsgeometrien und Hybridisierungslängen unterschiedliche Abrisskräfte aufweisen, sind auch andere Wechselwirkungen verwendbar. Für den Transport von Proteinen bietet es sich an, einen für ein am Cantilever angebundenes Molekül zugänglichen Griff am Protein zu nutzen, der sich mit dem zu transportierenden Protein koexprimieren lässt. Spezifische Antikörper-Antigen Wechselwirkungen gehören zu den prominentesten zur Verfügung stehenden Möglichkeiten. Ihre Abrisskräfte lassen sich z.B. durch Mutationen in der Antikörperbindungsregion verändern (49). Wenn das Antigen ein kleines Peptid ist, kann man

davon ausgehen, dass es sich mit dem Protein exprimieren lässt, ohne dessen Funktionalität zu beeinträchtigen. Ein vergleichsweise kleines single-chain Antikörper Fragment (scFv), das am Cantilever kovalent angebunden ist, zeigt selbst nur minimale Wechselwirkungen mit der Oberfläche und kann zum Aufnehmen des Proteins dienen. Voraussetzung für eine solche Realisierung ist aber ein vollständig aufeinander abgestimmtes hierarchische Kraftsystem. In Publikation 5 konnte gezeigt werden, dass der Aufbau eines solchen Kraftsystems möglich ist. Hierfür wurde ein chimärisches Konstrukt aus DNA und dem als Antigen wirkenden GCN4-Peptid am 3'-Ende der DNA als Transfermolekül verwendet. An den Cantilever wurde das C11L34 scFv angebracht. Im Depot- und Ziel-Bereich wurde die Anker-DNA am 5'- bzw. 3'-Ende befestigt und das Transfermolekül war im Depotbereich an die Anker-DNA hybridisiert. Das so aufgebaute Kraftsystem musste, um eine stimmige Hierarchie zu erreichen, so eingestellt werden, dass die Abrisskraft zwischen Antigen und Antkörper größer war als die im Depot, aber kleiner als die im Ziel ($F_{Depot}<F_{Cantilever}<F_{Ziel}$). Für die Abrisskräfte der DNA-Stränge im Depotbereich und im Zielbereich in unzip- bzw. Schergeometrie konnte eine nahezu konstante Abhängigkeit von der Zuggeschwindigkeit festgestellt werden, was auf das sequenzielle Öffnen der Basenpaarungen in der unzip-Geometrie bzw. das Auftreten des B-S-Übergangs (72) in der Schergeometrie zurückgeführt wird. Die Kraft, die für das Aufbrechen der Antikörper-Antigen Bindung benötigt wird, hängt logarithmisch von der Zuggschwindigkeit ab, was in erster Näherung durch das Bell-Evans Modell erklärt wird (73). Diese Abhängigkeiten von der Zuggeschwindigkeit erlauben eine Feineinstellung des Kraftsystems. Bei einer Zugeschwindigkeit von ca. 200 nm/s konnten Moleküle effizient im Zielgebiet abgesetzt werden, das „Ausschneiden" aus dem Depotbereich konnte auch bei größeren Geschwindigkeiten erfolgen. Neben dem hierarchischen Kraftsystem ist auch die zyklische Arbeitsweise, also die Möglichkeit, den Transport hunderte Male zu wiederholen, typisch für SMC&P. Diese ist aber nur gewährleistet, wenn die eingesetzten Moleküle nicht ihre Funktionalität verlieren. Insbesondere der immer wieder belastete Antikörper an der Spitze des Cantilevers muss also in dieser Ausführung sehr robust sein. In den Experimenten (die sich in Publikation 5 finden) konnte dies gezeigt werden, indem ein Muster, das einen Cantilever und einen Antikörper zeigt, auf die beschriebene Weise in etwa 600 Transportzyklen zusammengesetzt wurde.

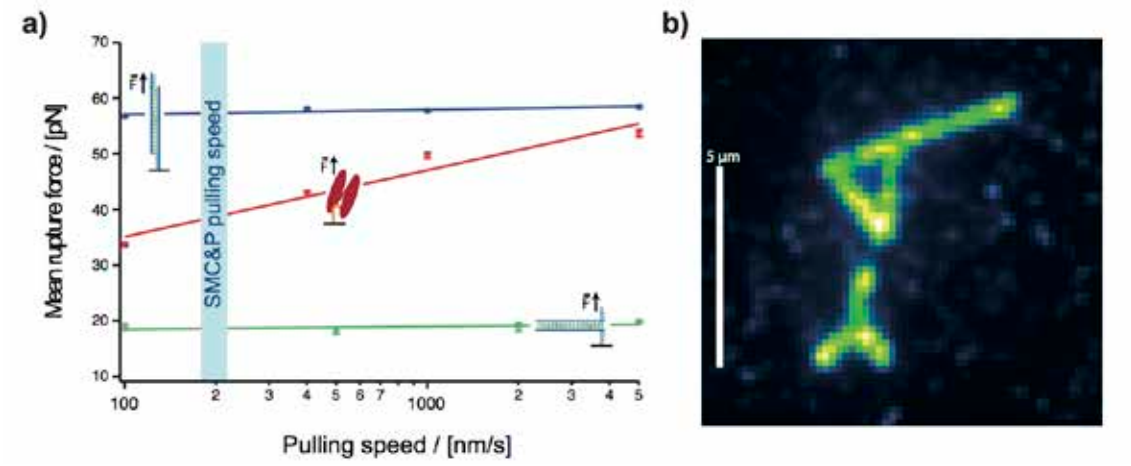

Fig. 12 a) Ein hierarchisches Kraftsystem konnte unter Einbeziehung einer Antikörper-Antigen Wechselwirkung aufgebaut werden. Die mittleren DNA Abrisskräfte in *unzip*- und Schergeometrie sind bei verschiedenen Zuggeschwindigkeiten näherungsweise konstant bei 20 pN bzw. 60 pN. Im Gegensatz dazu zeigt der Antikörper-Peptid Komplex eine logarithmische Abhängigkeit von der Zuggeschwindigkeit. Diese kann also zur Feinjustierung der Differenzen zwischen den mittleren Abrisskräften genutzt werden. b) Die Robustheit des Systems, insbesondere der am Cantilever befestigten Antikörperkomponente, konnte durch das Durchführen von vielen hundert SMC&P-Zyklen gezeigt werden. Die Moleküle wurden in Form eines Cantilevers mit Antikörper an der Spitze angeordnet. Nach (74).

Der direkte Transport und die Positionierung von einzelnen Proteinen mit SMC&P besitzt gegenüber der nachträglichen Anbindung an zuvor positionierte Bindungsstellen verschiedene Vorteile. Zum einen bedeutet es bei einer nachträglichen Anbindung zusätzlichen Aufwand, sicherzustellen, dass die Bindungsstellen vollständig besetzt wurden. Zum anderen entsteht beim Einbringen des anzubindenden Moleküls in die Lösung immer auch ein Hintergrund durch sich unspezifisch an die Oberfläche anlagernde Moleküle, da eine Passivierung durch Zuckermoleküle an der Oberfläche insbesondere bei Proteinen unterschiedlich gut wirkt. Außerdem können bei einem direkten Transport auch AFM-Daten für kraftspektroskopische Analysen herangezogen werden. Insbesondere sollte eine Manipulation einzelner Proteine (wie etwa Enzyme) durch den AFM-Cantilever bei gleichzeitiger Fluoreszenzbeobachtung an einem Ort, an dem sich keine weiteren Proteine befinden, möglich sein. Hierbei kann nach der funktionellen Zerstörung eines Proteins dieses durch Anwendung des SMCP-Zyklus leicht ersetzt werden. Auch die Verwendung von DNA im Depot- und Zielbereich bietet gegenüber Protein-Protein-Wechselwirkungen ein Reihe von Vorteilen. DNA ist offensichtlich biokompatibel, aber sehr robust und leicht verfügbar. Die sehr niedrigen Kräfte im Depotbereich bei gleichzeitig hoher Bindungsenergie ermöglichen es hier, die am Protein angreifende Kraft gering zu halten, was eine partielle Entfaltung unwahrscheinlich macht. Weiter lässt sich an DNA eine Feineinstellung von Abrisskräften und Bindungsenergien vornehmen, wenn dies das Experiment erfordert, indem die Anzahl der Basenpaarungen variiert wird. Ferner können in Experimenten mit verschiedenen Depot- und Zielregionen ungewollte Bindungen verhindert werden, indem die verwendeten Depot- und Ziel-Sequenzen

entsprechend gewählt werden. Die Realisierung eines direkten Transports von Proteinen mit dem oben vorgestellten, modifizierten Kraftsystem verlangt lediglich eine stabile Kopplung von DNA und Protein, da der GCN4-Tag ja mit dem Protein koexprimiert werden kann. Eine kovalente Verbindung zwischen DNA und Protein ist zwar sehr stabil, lässt sich abhängig vom Protein aber nur unter bestimmten Bedingungen und oft mit sehr schlechter Ausbeute bewerkstelligen. Um einen möglichst allgemeinen Ansatz zur Verfügung zu stellen, wurde für die Verbindung zwischen DNA und Protein der DNA-bindende Zif268-NRE-Zinkfinger benutzt. Auch dieses Molekül bietet ähnliche Vorteile wie die DNA. Aufgrund seines modularen Aufbaus können Bindungsenergien und Abrisskräfte variiert werden, und der Zinkfinger bindet sequenzspezifisch an dsDNA. Auch hier kann in Experimenten mit vielen Komponenten Crosstalk vermieden werden. Das verwendete 6-Finger-Protein besitzt sub-picomolare Affinität (55) und nach (75) einige hundert pN Abrisskraft. Aufgrund seiner einfach zu überprüfenden Funktionalität wurde GFP als Fusionsprotein mit GCN4 und Zinkfinger (GCN4-GFP-Zinkfinger) exprimiert. Das Fusionsprotein konnte selbstorganisierend an die DNA-Bindungssequenz koppeln. Ein Überhang an dieser Bindungssequenz konnte an die Ankersequenz hybridisieren. In den in Publikation 7 beschriebenen Experimenten konnten die DNA-Protein-Komplexe in mehreren hundert Transportzyklen in Ampelmännchen-Mustern arrangiert werden. Durch Auslesen der Fluoreszenz des GFP und der gelabelten DNA konnte gezeigt werden, dass mit diesem System der Transport von Proteinen möglich ist und ihre Funktionalität nicht beeinträchtigt wird. Die größte, beim Transport auftretende Abrisskraft tritt beim Abreißen des Antikörpers auf und beträgt ca. 40 pN. Diese Kraft reicht nicht aus, um das GFP zu entfalten und dadurch zu zerstören (76).

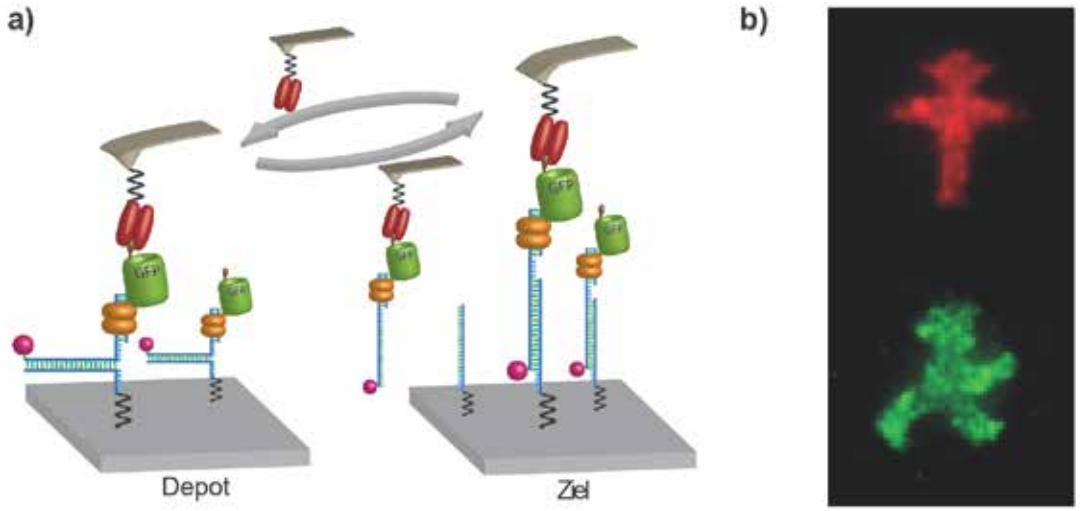

Fig. 13 a) Um eine Anordnung von Proteinen durch SMC&P möglich zu machen, wurde zwischen die Komponenten des in Fig. 11 gezeigten hierarchischen Kraftsystems ein GFP eingefügt. Die Verbindung zwischen DNA und Protein wurde durch eine äußerst stabile Zinkfinger-DNA Wechselwirkung erreicht. GCN4-GFP-Zinkfinger–DNA Komplexe wurden an die Anker-DNA im Depot hybridisiert, konnten dann vom Antikörper-funktionalisierten Cantilever aufgenommen und im Zielbereich beliebig arrangiert werden. b) Mit Hilfe eines Antikörperfragments am Cantilever konnten die Protein-DNA Komplexe im

Zielbereich zu molekularen Anordnungen in Form von Ampelmännchen zusammengefügt werden. Es wurde zunächst das obere Ampelmännchen assembliert und die rote Fluoreszenz des DNA-Labels ausgelesen. Dann wurde das untere Ampelmännchen zusammengesetzt und die grüne Fluoreszenz des GFP aufgenommen. Die Messungen zeigen, dass beide Komponenten gemeinsam transportiert wurden und dass das GFP durch die Krafteinwirkung nicht seine Funktionalität verliert.

Molekülweise, Funktionelle Assemblierung mit mechanischer Kontrolle

Das Zusammenfügen von Komponenten, die außerhalb des Komplexes ohne Funktion sind, zu einem Gesamtsystem mit einer neuen Funktionalität ist traditionell Aufgabengebiet der Ingenieure. Funktionale Assemblierung ist aber auch in der Natur eine gängige Weise, komplexe Aufgaben zu organisieren. Der Aufbau von Photosystemen (77) oder die Degradierung von Cellulose durch Cellulosome (78) sind prominente Beispiele. Obwohl im Hochvakuum und unter ultrakalten Bedingungen schon in den 90er Jahen kontrolliert atomare Arrangements mit neuen Eigenschaften geschaffen werden konnten (13), war dies unter physiologischen Bedingungen bis jetzt nicht möglich. In Publikation 6 wird über den mechanisch kontrollierten Aufbau von funktionalen Ensembles aus Einzelmolekülen berichtet. Für den experimentellen Machbarkeitsnachweis wurde das den Liganden Malachit Grün bindende RNA-Aptamer genutzt. Dieses Aptamer kann in zwei Hälften geteilt werden, die einzeln nicht die Fähigkeit haben, Malachit Grün zu binden. Das zusammengefügte Aptamer aber gewinnt die Funktion, Malachit Grün zu binden. Der gebundene Malachit Grün Farbstoff verliert aufgrund sterischer Einschränkungen Rotationsfreiheitsgrade für die Phenylringe, was dazu führt, dass die Quanteneffizienz um 3 Größenordnungen gesteigert wird. Dies kommt auf Einzelmolekülebene einem „Einschalten“ der Fluoreszenz gleich. Das Binden von Malachit Grün in das zusammengefügte Aptamer konnte an einzelnen Aptameren nachgewiesen werden. Hierfür wurde eine Hälfte des Aptamers (α-Teil) an die Oberfläche gebunden, die zusätzlich zur Aptamersequenz noch eine Ankersequenz aufwies. Eine zur Ankersequenz komplementäre Sequenz war an die zweite Hälfte des Aptamers (β-Teil) angefügt, so dass sie an den α-Teil angebunden werden konnte. Der β-Teil war mit einem Cy5 Farbstoff versehen, der nach dem Anbinden zur Lokalisierung des vollständigen Aptamers genutzt werden konnte und dann photogebleicht wurde. Nach der Zugabe von Malachit Grün trat an den Stellen, an denen Cy5-Fluoreszenz beobachtet worden war, fluoreszentes Blinken auf. Die Lokalisierung dieser Fluoreszenzereignisse ergab im Rahmen der Gerätegenauigkeit eine Übereinstimmung der Positionen von Cy5 und Malachit Grün. Es konnte also direkt das Binden durch die eintretende Quanteneffizienzverstärkung gemessen werden. Die β-Teile wurden dann mit den für SMC&P typischen Sequenzen versehen, die zum Anker- bzw. AFM-Strang komplementär sind, die α-

Teile mit der Ankersequenz. Auf einer Oberfläche, auf der die β-Teile im Depot an die Ankersequenz hybridisiert und die α-Teile kovalent im Zielgebiet befestigt wurden, konnten einzelne β-Moleküle vom Cantilever im Depot aufgenommen werden. Diese wurden dann im Zielgebiet an der programmierten Position abgesetzt, wo sie auf diese Weise mit mechanischer Kontrolle zu kompletten, funktionalen Aptameren zusammengefügt wurden. Die Robustheit der Methode und die Funktionalität der geschaffenen Aptamere konnte nachgewiesen werden, indem aus hunderten, kontrolliert assemblierten Aptameren auf der Oberfläche die Strukturformel des Malachit Grün Moleküls nachgebildet wurde. Nach Zugabe von Malachit Grün Molekülen konnten diese in die Bindungstaschen binden und so das Muster fluoreszieren lassen. Die Ergebnisse finden sich in Publikation 6.

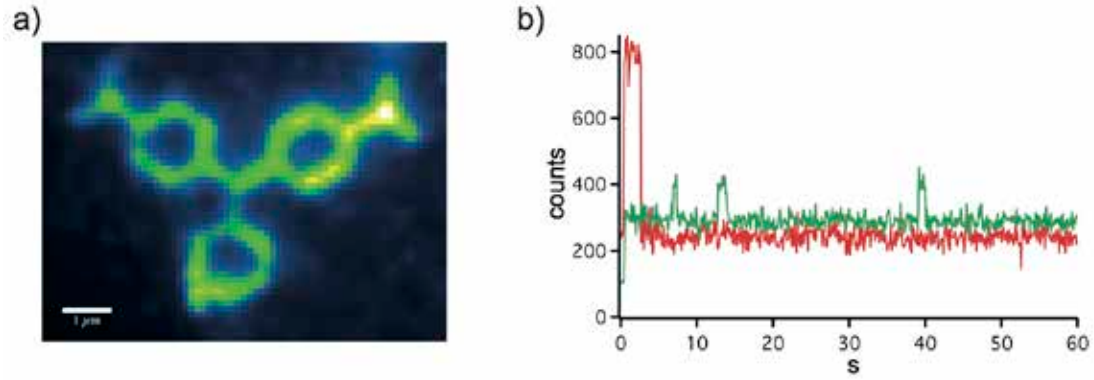

Fig. 14 a) Hunderte RNA-Stränge konnten durch SMC&P zu vollständigen, funktionalen Aptameren zusammengesetzt werden. Die Funktionalität wurde auf der Oberfläche im programmierten Muster der Malachit Grün Strukturformel sichtbar, nachdem Malachit Grün hinzugefügt worden war. b) Einzelne, assemblierte Aptamere wurden erst über die Cy5 Fluoreszenz (rot) lokalisiert. Nach Zugabe von 50 nM Malachit Grün wurde dann an derselben Stelle die (blinkende) Fluoreszenz der gebundenen Malachit Grün-Moleküle (grün) aufgenommen.

Validierungsstandards für hochauflösende Mikroskopie

Hochauflösende Mikroskopiemethoden haben in den Lebenswissenschaften eine wichtige Rolle eingenommen. Sie beruhen im Wesentlichen darauf, eine große Fraktion von Farbstoffmolekülen in einen inaktiven Zustand zu versetzen und die verbleibenden zu lokalisieren. Die häufige Wiederholung dieses Vorgangs erlaubt es dem Experimentator, sich ein Bild von der Probe zu machen. Um die komplexen Anordnungen vieler Moleküle, die mit SMC&P mit einer Präzision im Bereich von 10 nm erstellt werden können, im Fluoreszenzmikroskop aufzulösen, werden hochauflösende Mikroskopiemethoden benötigt. Auf der anderen Seite kann SMC&P auch verwendet werden, um Standards für die Validierung solcher Methoden zu schaffen oder Kalibrierungsstandards für die Optimierung solcher Methoden bereitzustellen. Programmierte Molekülanordnungen, die aus vielen Farbstoffen

bestehen, können zu diesem Zweck verwendet werden. Bei der BLINK Mikroskopie (30) werden Fluorophore durch die chemische Umgebung in einen nicht fluoreszenten Radikalanionzustand versetzt. Reduktionsmittel kontrollieren hierbei die Dauer von inaktiven Zuständen, Oxidationsmittel die der fluoreszenten. In Publikation 4 konnte für diese Mikroskopiemethode der Zusammenhang zwischen Fluorophor-Dichte und Auflösungsvermögen in Abhängigkeit weiterer, systemrelevanter Parameter gezeigt werden. Die programmierten Molekülmuster dienten dazu, die Abhängigkeit des Auflösungsvermögens von den chemischen Parametern und den Kompromiss zwischen Aufnahmegeschwindigkeit und Auflösungsvermögen aufzuzeigen.

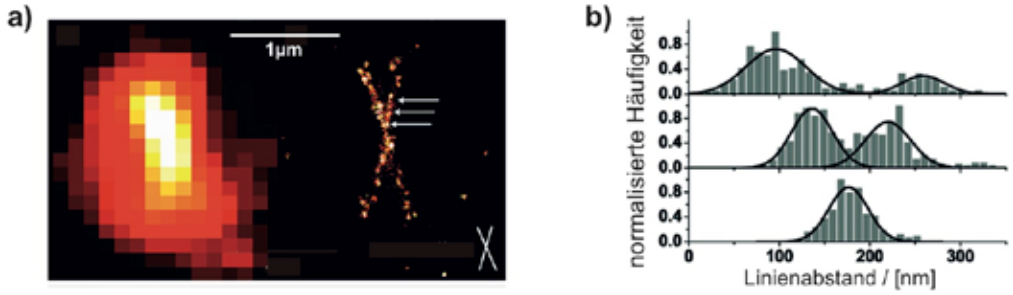

Fig. 15 Programmierbare Arrangements von Farbstoffmolekülen an der Oberfläche können durch SMC&P zur Verfügung gestellt werden. Diese werden als Validierungsstandards für hochauflösende Mikroskopiemethoden verwendet. a) Das X-förmige Muster, das durch SMC&P hergestellt wurde, kann durch beugungslimitierte, konventionelle Fluoreszenzmikroskopie nicht aufgelöst werden. Die Blink-Mikroskopie-Methode ermöglicht es, die Fluorophore zu lokalisieren und ein genaueres Bild des Musters zu rekonstruieren. b) Die Auswertung von Linienabständen kann dann zur Bestimmung des räumlichen Auflösungsvermögens herangezogen werden.

Einzelmolekül-Beobachtung von Horseradish Peroxidase

Um herauszufinden, welche Bedeutung Konformations-Fluktuationen für die Aktivität von Enzymen haben, ob dadurch auch zeitliche Fluktuationen der katalytischen Aktivität hervorgerufen werden, ist die Beobachtung einzelner Enzyme notwendig. TIRF-Mikroskopie oder auch konfokale Mikroskopie sind Beobachtungsmethoden, die hierfür verwendet wurden, da diese Methoden den Hintergrund reduzieren. Aus genau diesem Grund erscheint ein fluorogenes Enzymsubstrat, dessen Quanteneffizienz sich nach der katalytischen Verarbeitung durch das Enzym um Größenordungen steigert, besonders geeignet. Idealerweise würde ein nicht fluoreszierendes Substrat S an das beobachtete Enzym binden, dort nach dem Katalyseschritt als Produkt P beginnen, Photonen zu emittieren, und schließlich aus dem Beobachtungvolumen herausdiffundieren.

$$E + S \underset{k_{-1}}{\overset{k_1}{\rightleftharpoons}} ES \xrightarrow{k_2} EP_{fluorescent} \xrightarrow{k_3} E + P_{fluorescent}$$

Ein sehr robustes Enzym, das kommerziell z.B. in Western Blots und ELISA-Essays vielfach Verwendung findet, ist die 44 kDa schwere, in ihrer nativen Form glykosylierte Horseradish Peroxidase (HRP). Sie wurde aufgrund ihrer Robustheit für die in dieser Arbeit durchgeführten Experimente ausgewählt. Es ist davon auszugehen, dass das so standardisiert verwendete Enzym auch auf Polyethylenglycol-passivierten Glasoberflächen seine Arbeit verrichtet. Für Einzelmolekül-Experimente an HRP wurden bereits in früheren Arbeiten als fluorogene Substrate Dihydrorhodamin (DHR) oder Dihydroxyphenoxazin (Amplex Red) verwendet (79, 80).

Die Arbeitsweise von HRP ist gut verstanden (81). Im katalytischen Zentrum befindet sich die Häme-Gruppe mit einem Eisen-Ion in ihrem Zentrum. Das Enzym befindet sich zunächst im Grundzustand. Durch die Reduktion des Kosubstrats H_2O_2 wird das aktive Zentrum in einen Radikalzustand versetzt, aus dem das Enzym nach sukzessiver Oxidation von zwei Substratmolekülen in den Grundzustand zurückkehrt. Die Substratmoleküle können hierbei in Radikalzustände versetzt werden (82). Für die Reaktion gilt, dass das Verhältnis Substrat:H_2O_2 entweder 1:2 oder 1:1 ist. Für Amplex Red und DHR ist das 1:1 Verhältnis nachgewiesen worden (83, 84). Dies kann zum einen bedeuten, dass dasselbe Molekül zweimal hintereinander ein Elektron an HRP abgibt und somit am Enzym fluoreszent wird. Zum anderen ist es aber auch möglich, dass zwei Substrat-Radikale in die Lösung abgegeben werden und erst dort in einer enzymunabhängigen Dismutationsreaktion zu einem fluoreszenten Resorufin und einem nichtfluoreszenten Amplex Red reagieren (10).

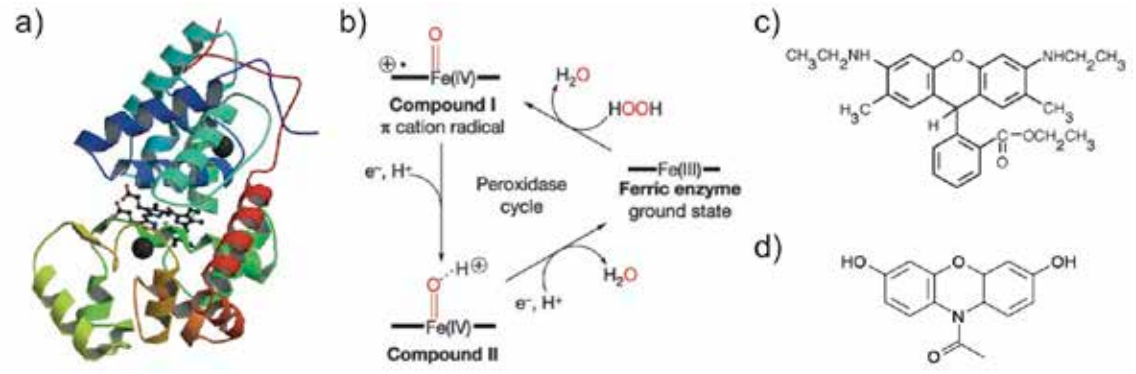

Fig. 16 a) Kristallstruktur von Horseradish Peroxidase. Die Häme-Gruppe bildet das katalytische Zentrum. b) Der Peroxidase-Zyklus. Das im Grundzustand befindliche Enzym wird durch das Kosubstrat H_2O_2 oxidiert und bildet daraufhin den *compound I* genannten Radikalzustand. Durch Oxidation eines Substratmoleküls kann sich das Enzym in den *compound II* Zustand begeben. Von hier kehrt es durch eine weitere Oxidation eines Substrats in den Grundzustand zurück. c) und d) zeigen die Strukturformeln von DHR und Amplex Red.

Ausgehend davon, dass die fluoreszenten Produkte direkt am Enzym entstehen, wurden Experimente durchgeführt, um die Aktivität von HRP auf Einzelmolekülebene zu beobachten.

Hierfür wurde HRP auf passivierte Glasoberflächen gebunden. Sobald Substrat hinzugegeben wurde, sollte Aktivität einzelner Enzyme aufgrund der immer neu entstehenden, fluoreszenten Enzym-Produkt-Komplexe kontinuierlich beobachtbar sein. Beide Substrate wurden, um die Messungen durchzuführen getestet. DHR erwies sich wegen seiner Instabilität in wässrigen Lösungen und der schlechten Löslichkeit als sehr unhandlich. Auch auf Oberflächen ohne HRP wurden konstant fluoreszierende Spots bei starkem Hintergrund gemessen. Amplex Red verhielt sich in diesen Punkten deutlich besser. Falsch-Positive Spots konnten aber nicht gänzlich ausgeschlossen werden. An den von den Spots erhaltenen Fluoreszenzzeitspuren konnten Autokorrelationsanalysen durchgeführt werden. Die von Edman *et al.* entwickelten Näherungen zur Beschreibung der Korrelation der Enzymaktivität als *stretched exponential* (79) konnten zwar auf die bei verschiedenen Konzentrationen gewonnenen Daten angewendet werden, allerdings war die Korrelation nur schwach und die Zeitauflösung reichte nicht, um die charakteristische Korrelationsstufe aufzulösen. Ausgehend davon, dass im Fluoreszenzmikroskop für den Enzymzustand nur zwischen einem Enzym mit und ohne fluoreszierendem Produkt unterschieden werden kann, ergibt sich unter der Annahme, dass Konformationsänderungen zu einem *stretched exponential*-Verhalten führen, für die Korrelationsfunktion G(τ) in erster Näherung:

$$G(\tau) = 1 + a \cdot e^{-k_{-1}\tau} + b \cdot e^{-(k_1 t)^{\beta}} + c$$, wobei $E \underset{k_{-1}}{\overset{k_1}{\rightleftarrows}} EP$, β stretch-Parameter.

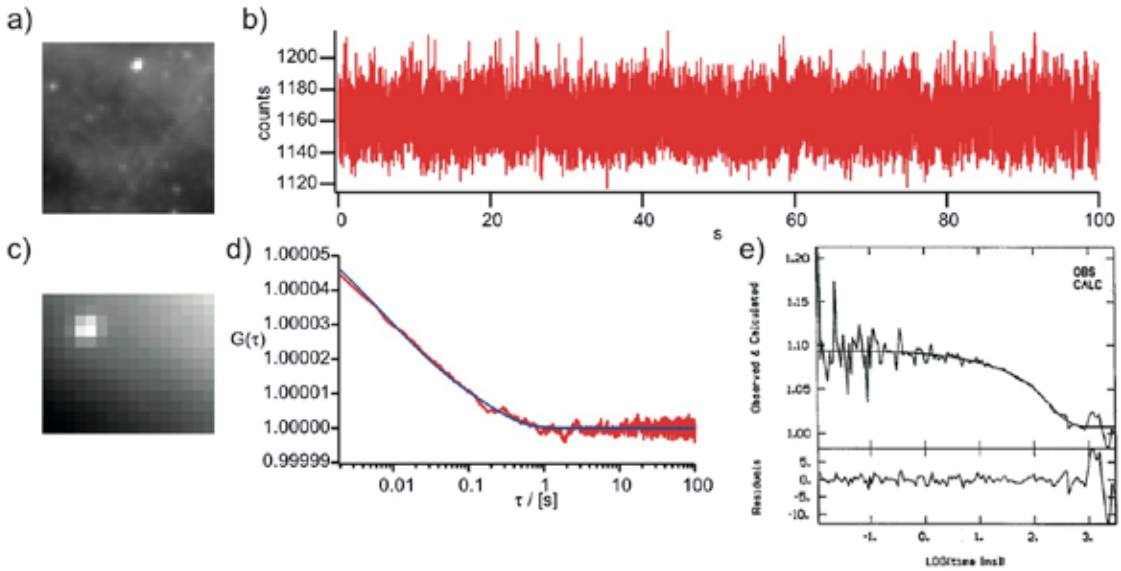

Fig. 17 a) zeigt ein Fluoreszenzbild einer Oberfläche ohne Horseradish Peroxidase, bei dem 5 µM DHR verwendet wurden. Die Verwendung des Substrats für Messungen mit Horseradish Peroxidase bietet sich nicht an, da die Zuordnung von Fluoreszenz zu Enzymen eine extrem schwierige Aufgabe darstellt. Besser verhält sich Amplex Red. Nach Hinzugabe von 1 µM Amplex Red können im TIRF-Mikroskop Zeitspuren (b) von kontinuierlich fluoreszierenden Spots (c) aufgenommen werden. Aus diesen können normierte Autokorrelationen errechnet werden (d), an die dann die Korrelationsfunktion nach Edman *et al.* (79) angefittet werden kann. e) Zeigt eine Autokorrelation aus (79), bei der die charakteristische Korrelationsstufe aufgelöst werden kann.

Bei den Experimenten fiel auf, dass auf der Oberfläche nur sehr wenige Enzyme identifiziert werden konnten, obgleich die Anbindungsdichte der Enzyme auf der Oberfläche sehr hoch war. Der These, dass durch das Binden an die Oberfläche die meisten Enzyme zerstört würden, stand ein sich im Laufe einer Messung verstärkender Hintergrund gegenüber. Da die wenigen als Enzyme identifizierten Spots unmöglich für den Umsatz einer so großen Menge von Substrat verantwortlich sein konnten, sollte auch eine gleichmäßig über die Oberfläche verteilte enzymatische Aktivität nachweisbar sein. Sofern die Bildung des fluoreszierenden Produkts direkt am Enzym erfolgte, sollte folgendes Experiment dies sichtbar machen. Mit größtmöglicher Dichte wurden Enzyme in einer Kammer auf eine Oberfläche gebunden. Die mit Enzymen besetzte Oberfläche wurde im TIRF-Mikroskop einmal im evaneszenten Feld beobachtet, einmal wurde sie außerhalb des evaneszenten Felds gehalten, so dass entstehende Produkte erst in das evaneszente Feld diffundieren mussten, um zur Hintergrund-Fluoreszenz beizutragen. Die direkt im evaneszenten Feld entstandenen Produkte hätten zu einer deutlich stärkeren und schneller auftretenden Fluoreszenz innerhalb des Anregungsvolumens führen sollen als die an der Enzymoberfläche außerhalb des evaneszenten Feldes entstandenen Produkte. Dies ließ sich allerdings nicht beobachten. Die Ergebnisse deuteten vielmehr darauf hin, dass auf der Oberfläche keine größere Konzentration von fluoreszierenden Produkten zu finden war als in der übrigen Lösung. Dies ist ein Hinweis darauf, dass fluoreszierende Produkte erst in Lösung entstehen. Die oben bereits erwähnte Möglichkeit, dass aus den Substraten zunächst Radikale gebildet werden, aus denen erst in einer weiteren enzymunabhängigen Reaktion fluoreszente Produkte hervorgehen, muss ernsthaft in Betracht gezogen werden. Die in (10) veröffentlichten Experimente zeigen dies ebenfalls.

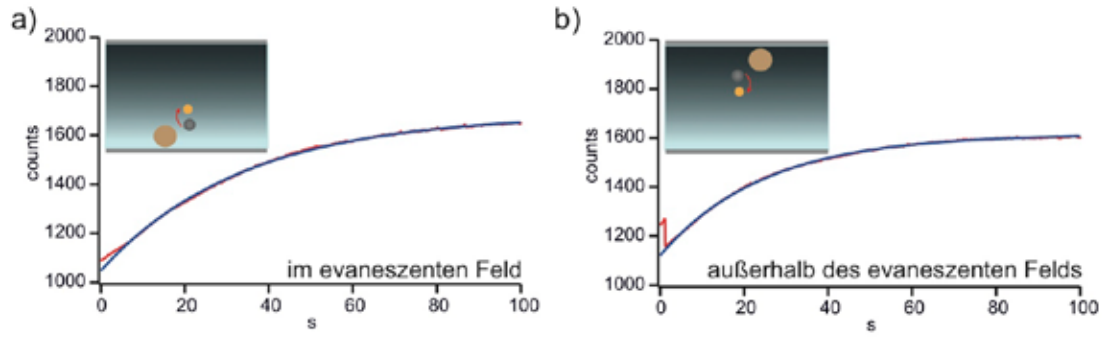

Fig. 18 Horseradish Peroxidase wurde dicht auf PEG-Oberflächen angebunden. Um den enzymatischen Umsatz von Amplex Substrat zu messen, wurde im TIRF-Mikroskop die im evaneszenten Feld entstehende Fluoreszenz beobachtet. Einmal befand sich bei der Beobachtung die Enzymoberfläche im evaneszenten Feld (a) und einmal außerhalb (b). Die gemessene Fluoreszenz (rot) wurde durch eine Exponentialfunktion gefittet (blau). Wenn direkt am Enzym das fluoreszierende Produkt entsteht, so wäre eine stärkere Fluoreszenz in (a) zu erwarten. Rate und Amplitude der Fluoreszenzzunahme waren bei den Messungen aber vergleichbar. Dass erst eine enzymunabhängige Reaktion die fluoreszierenden Produkte erzeugt ist sehr wahrscheinlich.

Publikationen

Publikation 1

Nanoparticle Self-Assembly on a DNA-Scaffold Written by Single-Molecule Cut-and-Paste.

Puchner, E. M.; Kufer, S. K.; Strackharn, M.; Stahl, S. W.; Gaub, H. E.; Nano Lett 2008, 8 (11), 3692-3695.

NANO
LETTERS

2008
Vol. 8, No. 11
3692-3695

Nanoparticle Self-Assembly on a DNA-Scaffold Written by Single-Molecule Cut-and-Paste

Elias M. Puchner,[†,‡] Stefan K. Kufer,[†] Mathias Strackharn,[†] Stefan W. Stahl,[†] and Hermann E. Gaub*[,†]

Chair for Applied Physics, Center for Nanoscience and Center for Integrated Protein Science Munich, Ludwig-Maximilians-Universität Munich, Amalienstrasse 54, 80799 Munich

Received June 27, 2008; Revised Manuscript Received September 16, 2008

ABSTRACT

Self-assembly guided by molecular recognition has in the past been employed to assemble nanoparticle superstructures like hypercrystals or nanoparticle molecules. An alternative approach, the direct molecule-by-molecule assembly of nanoscale superstructures, was demonstrated recently. Here we present a hybrid approach where we first assemble a pattern of binding sites one-by-one at a surface and then allow different nanoparticles to attach by self-assembly. For this approach, biotin bearing DNA oligomers were picked up from a depot using a cDNA strand bound to an AFM tip. These units were deposited in the target area by hybridization, forming a recognition pattern on this surface. Fluorescent semiconductor nanoparticles conjugated with streptavidin were allowed to assemble on this scaffold and to form the final nanoparticle superstructures.

Two fundamentally different strategies, commonly referred to as top-down or bottom-up, are feasible for the assembly of functional nanosystems. The bottom-up approach has two extremes. In the first, the building blocks are allowed to self-assemble, for example, guided by molecular recognition, much in the way mother nature does in embryogenesis.[1−7] Alternatively, the building blocks are assembled one-by-one, for example, using the tip of a scanning probe microscope, as we have demonstrated recently.[8,9] With the single-molecule cut-and-paste (SMCP) approach, we combine the precision of an AFM[10−12] with the selectivity of the DNA interaction. The units to be assembled, here biotin, are picked up with an AFM tip from a depot, where both the interaction of the unit with the depot surface as well as with the tip are mediated by specific DNA oligomers. Also the target area is covered with DNA oligomers. The interaction forces are chosen by binding geometry and by sequence such that the unit is first transferred from the depot to the tip and then from the tip to the target, allowing for a cyclic operation and thus the assembly of complex patterns of units. In this study, we have merged these two very successful strategies of self- and one-by-one assembly. We combined molecule-by-molecule assembly of patterns of binding sites with the self-assembly of nanoparticles[13] guided by specific molecular interactions to the scaffold.

The surface assembly process of the binding scaffold is schematically depicted in Figure 1. Both depot and target areas were functionalized with DNA anchor oligomers capable of hybridizing with the so-called transfer DNA via a 30 basepair (bp) DNA sequence. In the depot area, the anchor oligomers are covalently attached with the 5′ end and in the target area with the 3′ end. The depot area was then loaded with the transfer DNA, which is used as a carrier for the binding site for the nanoparticles, in this case biotin. The transfer DNA is designed such that it hybridizes at its 5′ end with the anchor sequence and has a 20 bp overhang at the 3′ end. An AFM cantilever was covalently functionalized with a 20 bp DNA oligomer complementary to the overhang sequence. This cantilever was carefully lowered toward the depot surface allowing the tip oligomer to hybridize with the transfer DNA. This approach had been either stopped upon surface contact or alternatively, proximity had been detected by increased viscous damping of the tip vibrations. Typical force extension traces of this contact and noncontact pick up are shown in the Supporting Information (Figure S4).

Upon withdrawing the tip from the surface, the force that is built up in the molecular complex propagates through the two oligomers with the different geometries. Whereas the anchor duplex is loaded in unzip geometry, the tip duplex is loaded in shear geometry. As has been shown, the unbinding forces for these two configurations under load differ signifi-

* To whom the correspondence should be addressed. Email: gaub@lmu.de.
† Chair for Applied Physics, Munich.
‡ Center for Integrated Protein Science, Munich.

10.1021/nl8018627 CCC: $40.75
Published on Web 10/01/2008

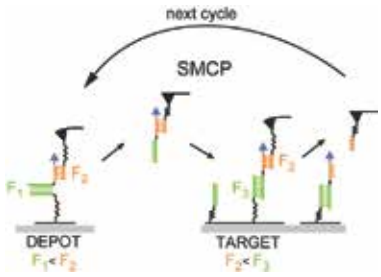

Figure 1. Schematics of the SMCP process. The transfer DNA oligomers carry biotin as the functional binding site (blue). They are stored in the depot area through specific DNA hybridization (30 bp, green) to the covalently immobilized depot anchor oligomer in the zipper geometry. The overhanging sequence of the transfer DNA is complementary to a 20 bp sequence, which is covalently attached to a tip of an AFM cantilever. When the cantilever is brought into contact with the surface, a 20 bp duplex (yellow) in shear geometry is formed. Although the binding energy of the transfer DNA to the depot is higher, the unbinding force F_1 is lower than the unbinding force F_2 between the tip and the transfer DNA due to the different unbinding geometries (zipper vs shear). Therefore, the transfer DNA remains on the tip sequence upon retraction of the cantilever. The tip is then moved to the target area with nm-precision and again brought into contact with the surface. Here the free part of the transfer DNA hybridizes to the 30 bp target sequence in shear mode. Since its rupture force F_3 is the highest, the transfer DNA including its functional unit biotin remains on the target site when removing the cantilever. Having transferred one functional unit in this way, the tip sequence is free again for the next cut-and-paste cycle.

cantly.[14,15] The rationale behind this effect is that the mechanical work to overcome the binding energy is performed over paths of different length, resulting in different forces. Despite the higher thermodynamic stability of the 30 bp anchor duplex compared to the 20 bp tip duplex, the rupture probability for the anchor is higher by an order of magnitude than that of the tip duplex. For a quantitative analysis see ref 16. As a result, the transfer DNA with the functional unit biotin is now bound to the tip and may be transferred to the target area.

At the target site the tip is lowered again, allowing the transfer DNA to hybridize at the chosen position with an anchor oligomer. Now, due to the different attachment, both duplexes are loaded in shear geometry when the tip is withdrawn. The longer anchor oligomer keeps the transfer DNA bound, and the tip is free again and ready to pick up the next object. The efficiency of the cut-and-paste process depends both on the density of DNA oligomers and the tip size. It can be adjusted so that rarely more than one oligomer per cycle is picked up.[8] As a consequence of this low functionalization density no pick up occurs in the majority of the attempts. In this study, we have chosen a tip radius of about 20 nm (MLCT lever C, Veeco Instruments GmbH, Mannheim, Germany) and a high functionalization density so that in each cycle at least one molecule, and in most cases more than one molecule, was picked up and delivered. For a detailed description of this ordered system of unbinding forces and the experimental setup see the Supporting Information (Figure S2).

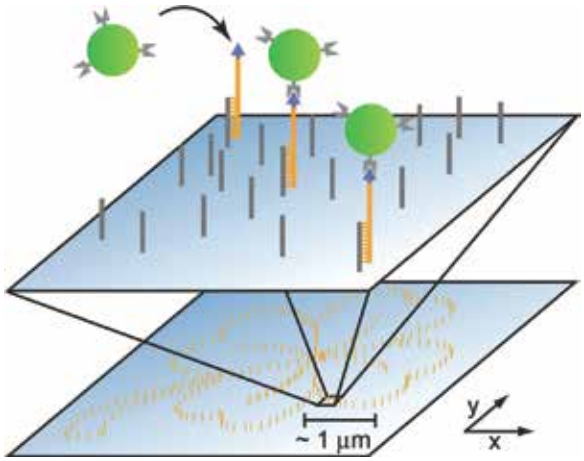

Figure 2. Sketch of the self-assembly of nanoparticles to a defined pattern guided by molecular recognition. SMCP allows the creation of DNA scaffolds of arbitrary shape and size. Here, a 5 μm sized pattern with the shape of a cloverleaf was created by transferring the biotin-modified transfer DNAs one-by-one to the target area. The spacing of binding sites was chosen to be 100 nm. In a second step this DNA scaffold allows for the self-assembly of streptavidin conjugated nanoparticles to form a superstructure.

All transfer steps are monitored online by force extension traces, which have clearly distinguishable fingerprints for each of the unzip or shear processes (see Supporting Information). If needed, each of the individual steps may be corrected or repeated. It should be pointed out here that this hierarchy of binding forces, which is the basis of this single-molecule cut-and-paste surface assembly (SMCP), may be established by a variety of interactions of physical, chemical, or biological nature. We chose DNA here since its properties are conveniently programmed by their sequence and binding geometry. It should also be mentioned that although the AFM potentially has sub-Angström positioning precision, the use of the polymeric spacers that we employ for the attachment of the DNA oligomers to the tip and the surface reduces this precision to the 10 nm range, which for our purposes is easily tolerable.

Following this protocol we now assembled a pattern of attachment points at the target site. We placed biotins 100 nm apart from each other along the outline of a cloverleaf. This is schematically shown in Figure 2. We then incubated the sample with a 500 pM solution of fluorescent nanoparticles (Qdots, streptavidin conjugate starter kit, Invitrogen, California) carrying an average of seven streptavidins, which recognize and selectively bind to biotin.[17] Although some spots of the written pattern may consist of more than one biotin because of the chosen high cut-and-paste efficiency, binding of more than one nanoparticle is unlikely because of their large size (about 20 nm) and their low concentration. We followed the binding process online by fluorescence microscopy in TIRF excitation. As can be seen in the picture series in Figure 3, the nanoparticles gradually assembled on the scaffold and finally decorated the outline of the cloverleaf. We encourage the reader to watch the movie of this nanoparticle attachment to the DNA scaffold published in

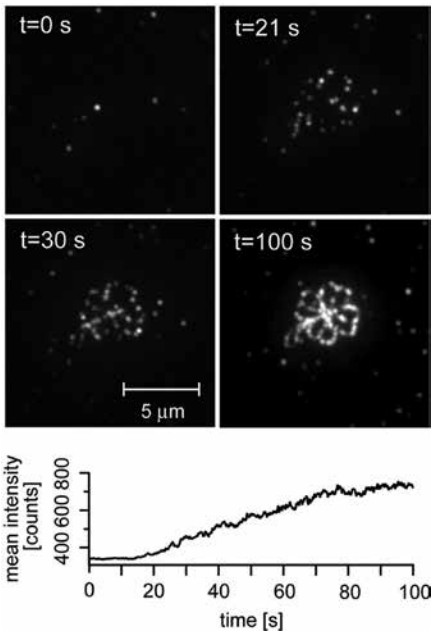

Figure 3. Time evolution of the nanoparticle superstructure formation. At time $t = 0$, streptavidin conjugated nanoparticles were incubated on the sample at a concentration of 500 pM. After approximately 20 s, the particles are close to the surface and start to specifically bind to the biotin-DNA scaffold until saturation is reached. The binding kinetics was followed by plotting the mean intensity of the observed area against the time (bottom). After 100 s the formation was completed.

the Supporting Information, as it demonstrates this process in a much clearer way.

This self-assembly process on the predefined scaffold is completed within minutes. Because of the specific binding between biotin and streptavidin and the low concentration of only 500 pM of the nanoparticles, nonspecific adhesion was negligible as can be seen in Figure 3. It is interesting to note that not all of the positions light up, although our transfer protocols corroborate that a biotin was deposited at these optical voids. A comparison of AFM images (not shown here) with the fluorescence images demonstrated that nanoparticles had bound at these positions. Obviously those nanoparticles had been optically inactive, a phenomenon that has been frequently described in the literature.[18,19]

For demonstration purposes, we rewrote the pattern in different sizes and allowed different nanoparticles to assemble on them (see Figure 4). Again a sizable fraction of the nanoparticles was optically inactive. In the assembly of the red pattern, thermal drift caused a slight distortion of the pattern, but even the scale bar could be trustfully assembled. Since for this study we always used the biotin−streptavidin interaction as the coupler, only single component structures were assembled. However, since a multitude of couplers with orthogonal affinities is available, the assembly of multicomponent structures would be straightforward.[20−23]

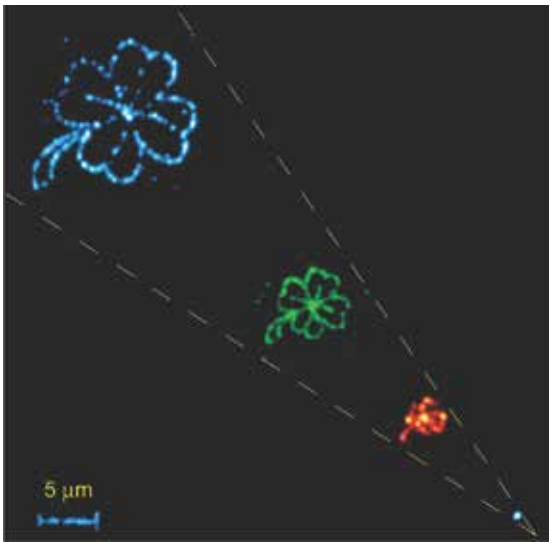

Figure 4. Nanoparticle superstructures of different sizes and compounds. To show the possibility to create freely programmable architectures from different compounds, the superstructure was scaled down and built with nanoparticles of different size. For the first cloverleaf (10 μm, blue), we used nanoparticles emitting at a wavelength of 525 nm, for the second one (5 μm, green) particles emitting at 565 nm, and for the third one (2.5 μm, red), already close to the limit of optical resolution, particles emitting at a wavelength of 705 nm. Please note that the 5 μm scalebar also represents a nanoparticle superstructure. The images are standard deviation maps of the recorded movies.

Nanoparticle self-assembly guided by specific molecular interactions has in the past been very successfully used to design complex structures with novel functions promising a rich field of new applications.[24−29] Here we have expanded this concept by a written scaffold and demonstrated that molecule-by-molecule assembly of a binding pattern combined with the self-assembly of semiconductor nanoparticles guided by molecular interactions is a straightforward and very general means to create nanoparticle superstructures.[30] Whereas the assembly of planar nanoparticle structures of arbitrary design can easily be assembled this way, an expansion into the third dimension appears challenging but achievable. Covalent cross-linking of the DNA oligomers after hybridization can be employed to stabilize the scaffold, and multifunctionality of the nanoparticles attachment sites may be used to build subsequent layers of structures. This could lead to a new dimension of complexity and novel effects.

Acknowledgment. We thank A. Fornof, H. Gumpp, H. Clausen-Schaumann, W. Parak, and P. Tinnefeld for helpful discussions. This work was supported by the German Science Foundation, FUNS, and the Nanosystems Initiative Munich (NIM).

Note Added after ASAP Publication: This paper was published ASAP on October 1, 2008. Author affiliations and Acknowledgment were updated. The revised paper was reposted on October 8, 2008.

Supporting Information Available: This material is available free of charge via the Internet at http://pubs.acs.org.

References

(1) Park, S. Y.; Lytton-Jean, A. K. R.; Lee, B.; Weigand, S.; Schatz, G. C.; Mirkin, C. A. *Nature* **2008**, *451* (7178), 553–556.
(2) Shevchenko, E. V.; Ringler, M.; Schwemer, A.; Talapin, D. V.; Klar, T. A.; Rogach, A. L.; Feldmann, J.; Alivisatos, A. P. *J. Am. Chem. Soc.* **2008**, *130* (11), 3274.
(3) Nykypanchuk, D.; Maye, M. M.; van der Lelie, D.; Gang, O. *Nature* **2008**, *451* (7178), 549–552.
(4) Mirkin, C. A.; Letsinger, R. L.; Mucic, R. C.; Storhoff, J. J. *Nature* **1996**, *382* (6592), 607–609.
(5) Alivisatos, A. P.; Johnsson, K. P.; Peng, X. G.; Wilson, T. E.; Loweth, C. J.; Bruchez, M. P.; Schultz, P. G. *Nature* **1996**, *382* (6592), 609–611.
(6) Maye, M. M.; Nykypanchuk, D.; van der Lelie, D.; Gang, O. *Small* **2007**, *3* (10), 1678–1682.
(7) Mirkin, C. A. *Inorg. Chem.* **2000**, *39* (11), 2258–2272.
(8) Kufer, S. K.; Puchner, E. M.; Gumpp, H.; Liedl, T.; Gaub, H. E. *Science* **2008**, *319* (5863), 594–596.
(9) Duwez, A. S.; Cuenot, S.; Jerome, C.; Gabriel, S.; Jerome, R.; Rapino, S.; Zerbetto, F. *Nat. Nanotechnol.* **2006**, *1* (2), 122–125.
(10) Binnig, G.; Quate, C. F.; Gerber, C. *Phys. Rev. Lett.* **1986**, *56* (9), 930–933.
(11) Radmacher, M.; Fritz, M.; Hansma, H. G.; Hansma, P. K. *Science* **1994**, *265* (5178), 1577–1579.
(12) Radmacher, M.; Tillmann, R. W.; Fritz, M.; Gaub, H. E. *Science* **1992**, *257* (5078), 1900–1905.
(13) Steigerwald, M. L.; Alivisatos, A. P.; Gibson, J. M.; Harris, T. D.; Kortan, R.; Muller, A. J.; Thayer, A. M.; Duncan, T. M.; Douglass, D. C.; Brus, L. E. *J. Am. Chem. Soc.* **1988**, *110* (10), 3046–3050.
(14) Rief, M.; Clausen-Schaumann, H.; Gaub, H. E. *Nat. Struct. Biol.* **1999**, *6* (4), 346–349.
(15) Strunz, T.; Oroszlan, K.; Schafer, R.; Guntherodt, H. J. *Proc. Natl. Acad. Sci. U.S.A.* **1999**, *96* (20), 11277–11282.
(16) Morfill, J.; Kuhner, F.; Blank, K.; Lugmaier, R. A.; Sedlmair, J.; Gaub, H. E. *Biophys. J.* **2007**, *93* (7), 2400–2409.
(17) Mann, S.; Shenton, W.; Li, M.; Connolly, S.; Fitzmaurice, D. *Adv. Mater.* **2000**, *12* (2), 147–150.
(18) Kuno, M.; Fromm, D. P.; Hamann, H. F.; Gallagher, A.; Nesbitt, D. J. *J. Chem. Phys.* **2000**, *112* (7), 3117–3120.
(19) Kuno, M.; Fromm, D. P.; Johnson, S. T.; Gallagher, A.; Nesbitt, D. J. *Phys. Rev. B* **2003**, *67* (12).
(20) Lacoste, T. D.; Michalet, X.; Pinaud, F.; Chemla, D. S.; Alivisatos, A. P.; Weiss, S. *Proc. Natl. Acad. Sci. U.S.A.* **2000**, *97* (17), 9461–9466.
(21) Gerion, D.; Parak, W. J.; Williams, S. C.; Zanchet, D.; Micheel, C. M.; Alivisatos, A. P. *J. Am. Chem. Soc.* **2002**, *124* (24), 7070–7074.
(22) Sperling, R. A.; Pellegrino, T.; Li, J. K.; Chang, W. H.; Parak, W. J. *Adv. Funct. Mater.* **2006**, *16* (7), 943–948.
(23) Levy, R.; Wang, Z. X.; Duchesne, L.; Doty, R. C.; Cooper, A. I.; Brust, M.; Fernig, D. G. *ChemBioChem* **2006**, *7* (4), 592–594.
(24) Bek, A.; Jansen, R.; Ringler, M.; Mayilo, S.; Klar, T. A.; Feldmann, J. *Nano Lett.* **2008**, *8* (2), 485–490.
(25) Clapp, A. R.; Medintz, I. L.; Uyeda, H. T.; Fisher, B. R.; Goldman, E. R.; Bawendi, M. G.; Mattoussi, H. *J. Am. Chem. Soc.* **2005**, *127* (51), 18212–18221.
(26) Huang, Y.; Duan, X. F.; Cui, Y.; Lauhon, L. J.; Kim, K. H.; Lieber, C. M. *Science* **2001**, *294* (5545), 1313–1317.
(27) Parak, W. J.; Gerion, D.; Pellegrino, T.; Zanchet, D.; Micheel, C.; Williams, S. C.; Boudreau, R.; Le Gros, M. A.; Larabell, C. A.; Alivisatos, A. P. *Nanotechnology* **2003**, *14* (7), R15–R27.
(28) Brennan, J. L.; Hatzakis, N. S.; Tshikhudo, T. R.; Dirvianskyte, N.; Razumas, V.; Patkar, S.; Vind, J.; Svendsen, A.; Nolte, R. J. M.; Rowan, A. E.; Brust, M. *Bioconjugate Chem.* **2006**, *17* (6), 1373–1375.
(29) Zhou, D.; Piper, J. D.; Abell, C.; Klenerman, D.; Kang, D. J.; Ying, L. *Chem. Commun. (Cambridge, U.K.)* **2005**, (38), 4807–9.
(30) Pellegrino, T.; Kudera, S.; Liedl, T.; Munoz Javier, A.; Manna, L.; Parak, W. J. *Small* **2005**, *1* (1), 48–63.

NL8018627

Supplementary Information

Nanoparticle Self-Assembly on a DNA-Scaffold written by Single-Molecule Cut-and-Paste

E.M. Puchner, S.K. Kufer, M. Strackharn, S. Stahl and H.E. Gaub*

Chair for Applied Physics, Center for Nanoscience and Center for Integrated Protein Science Munich,

Ludwig-Maximilians-Universität Munich,

Amalienstr. 54, 80799 Munich

*To whom correspondence should be addressed.
Email: gaub@lmu.de

Sample Preparation
Depot and target areas were prepared on a cover slip as described in [1]. Briefly, cover slips were amino functionalized and covalently modified with NHS-PEG-maleimide (M = 5000 g/mol, Nektar, Huntsville, Alabama, USA). After rinsing with H_2O, a PDMS flow chamber with two channels was mounted on one cover slip. Both channels were connected to a peristaltic pump. The anchor oligomers for the depot and target area were reduced using TCEP solution (Pierce, Rockford, Illinois, USA) in order to generate free mercaptans. The left channel (depot area) was rinsed for 1 h with a 10 µM solution of depot anchor oligomers and the right one (target area) with a 10 µM solution of target anchor oligomers. Afterwards both channels were rinsed with H_2O to remove all non-covalently bound oligomers. The left channel (depot area) was rinsed with a 1 µM solution of transfer DNA dissolved in saline sodium citrate (SSC) buffer (150 mM NaCl, 15 mM sodium citrate, pH 7) for 1 h. All oligomers used in this study were synthesized from IBA (IBA GmbH, Göttingen, Germany) and of HPLC-grade. After rinsing the depot channel for 5 min with SSC buffer to remove all non-hybridized transfer DNA, the PDMS flow chamber was removed and the cover slip was dried in a nitrogen stream. Finally the cover slip was mounted to the AFM-TIRF sample holder and immersed in SSC buffer.

AFM Measurements
All SCMP experiments were performed with a custom build AFM [2] at room temperature in SSC buffer (Fig. S1). Silicon nitride cantilevers (MLCT-AUHW, Veeco Probes, Camarillo, California, USA) were amino functionalized and covalently modified with NHS-PEG-maleimide (M = 5000 g/mol, Nektar, Huntsville, Alabama, USA) as described in [1]. The spring constant of the DNA modified cantilever was calibrated in solution using the equipartition theorem [3,4]. This method yielded a spring constant of about 15 pN/nm and a resonance frequency of 1.24 kHz for the cantilevers used in this study. The tip was withdrawn from the surface at a speed of 1500 nm/s until it was 2 µm above the surface. The protocol for the SMCP as well as the data recording was programmed using Igor Pro 5.03 (Wave Metrics, Lake Oswego, Oregon, USA). An Asylum Research controller, which provides ADC and DAC channels as well as a DSP board, was used for setting up feedback loops. Cantilever positioning for pickup and delivery was controlled in closed-loop operation. The precision was set to ±4 nm.

Total Internal Reflection Fluorescence (TIRF) Microscope
Single-molecule fluorescence microscopy was carried out in TIRF excitation (Fig. S1). Fluorescence excitation of nanoparticles was performed by a 532 nm, 75 mW DPSS laser (Crystalaser, Nevada, USA) and by a 473nm, 100 mW DPSS laser (Laser Quantum, UK) through a 100x/1.49 oil immersion objective lens (Nikon CFI Apochromat TIRF, Japan), where the collimated laser beam is focused in the back focal plane of the objective lens such that the beam is totally reflected at the cover slip. Fluorescence light is either split by color with a commercial Dual View (Optical Insights, Arizona, USA) with Brightline HC 582/75 (Semrock, New York, USA) and ET 700/75 (Chroma, Vermont, USA) as emission filters for the green and red channel respectively and a dichroic mirror with a cut-off wavelength of 630 nm (630DCLP) when using 532 nm excitation or filtered by a emission filter HQ 525/50 (Chroma, Vermont, USA) when using 473 nm excitation wavelength. The emitted light is detected by a 512 x 512 pixel back-illuminated EMCCD camera (DU-897, Andor, Belfast, Ireland). Time series where recorded in frame-transfer mode with an integration time of 100 ms per frame. The EMCCD chip was typically operated at a temperature of -75°C and an electron multiplication gain of 300x was used. The magnification was 96, i.e. 125 nm are

imaged to one pixel.

The SMCP force system

The probe of an atomic force microscope (AFM) was used to assemble individual single stranded DNA (ssDNA) oligomers one by one in aqueous solutions at room temperature. The oligomers were stored on well-defined depot areas, picked up with the tip of an AFM cantilever and reassembled with nanometer precision on a spatial distinct target area. The storage, the pick up and the deposition of the DNA oligomers were realized by using an ordered system of unbinding forces based on DNA interactions.

The dissociation rates of DNA duplexes under load are highly dependent on loading geometries and DNA sequences [5,6]. The geometry, in which the DNA duplex is stretched at opposite 5' and 3' ends, is called "shear mode" [5] (Fig. S2e), whereas the arrangement when double strands are loaded by pulling on the 5' and 3' extremities of one end of the duplex is called "unzip mode" [7] (Fig. S2a). These two geometries are well distinguishable concerning their dissociation properties under load.

The rupture forces of DNA duplexes loaded in unzip mode are independent both of the length of the DNA sequence and the loading rate, but vary for G-C and A-T interactions. G-C pairing results in a dissociation force of 20 pN whereas A-T gives 10 pN [6]. The dissociation forces for DNA duplexes loaded in shear geometry depend both on the length and sequence of the DNA and the loading rate [5].

To store the transfer DNA in the depot, a 30 base pair (bp) long anchor sequence with mixed G-C and A-T is used (Fig. S2a). The transfer DNA has in addition to this 30 bp anchor sequence a 20 bp handle sequence for pick up. The AFM-tip is covalently modified with a DNA oligomer, which is complementary to the handle sequence and forms a duplex if tip approaches the depot area (Fig. S2b). If the tip is retracted from the depot, the anchor sequence is loaded in unzip mode whereas the handle sequence is loaded in shear mode. Although the 30 bp anchor sequence is longer than the 20 bp handle sequence, its unbinding probability under load is much higher than for the handle sequence so that the transfer DNA is picked up (Fig. S2c, Fig. 4).

After translocation of the transfer DNA to its target site the cantilever is moved down. Since the target area is covalently modified with DNA oligomers that are complementary to the anchor sequence a 30 bp duplex in shear geometry is formed (Fig S2d). As the dissociation force of duplexes in shear geometry depends on the length of the DNA sequence the shorter handle sequence ruptures first and the transfer DNA is attached to the target site (Fig. S2e, Fig. 4). The DNA sequences of the oligomers used in this study are shown in Fig. S3.

Hybridization of fluorescent nanoparticles to the DNA scaffold

For the hybridization to the DNA-biotin scaffold, the following fluorescent semiconductor nanoparticles were used:
Invitrogen, Germany, streptavidin conjugate, 1 μM solution, Qdot 525 (colored blue), Qdot 565 (colored green), and Qdot 705 (colored red). The nanoparticles were incubated on the written DNA-biotin pattern at a final concentration of 500 pM in 0.1x SSC buffer. After about one minute, the self assembly process of nanoparticles to the pattern was complete.

imaged to one pixel.

The SMCP force system
The probe of an atomic force microscope (AFM) was used to assemble individual single stranded DNA (ssDNA) oligomers one by one in aqueous solutions at room temperature. The oligomers were stored on well-defined depot areas, picked up with the tip of an AFM cantilever and reassembled with nanometer precision on a spatial distinct target area. The storage, the pick up and the deposition of the DNA oligomers were realized by using an ordered system of unbinding forces based on DNA interactions.

The dissociation rates of DNA duplexes under load are highly dependent on loading geometries and DNA sequences [5,6]. The geometry, in which the DNA duplex is stretched at opposite 5' and 3' ends, is called "shear mode" [5] (Fig. S2e), whereas the arrangement when double strands are loaded by pulling on the 5' and 3' extremities of one end of the duplex is called "unzip mode" [7] (Fig. S2a). These two geometries are well distinguishable concerning their dissociation properties under load.

The rupture forces of DNA duplexes loaded in unzip mode are independent both of the length of the DNA sequence and the loading rate, but vary for G-C and A-T interactions. G-C pairing results in a dissociation force of 20 pN whereas A-T gives 10 pN [6]. The dissociation forces for DNA duplexes loaded in shear geometry depend both on the length and sequence of the DNA and the loading rate [5].

To store the transfer DNA in the depot, a 30 base pair (bp) long anchor sequence with mixed G-C and A-T is used (Fig. S2a). The transfer DNA has in addition to this 30 bp anchor sequence a 20 bp handle sequence for pick up. The AFM-tip is covalently modified with a DNA oligomer, which is complementary to the handle sequence and forms a duplex if tip approaches the depot area (Fig. S2b). If the tip is retracted from the depot, the anchor sequence is loaded in unzip mode whereas the handle sequence is loaded in shear mode. Although the 30 bp anchor sequence is longer than the 20 bp handle sequence, its unbinding probability under load is much higher than for the handle sequence so that the transfer DNA is picked up (Fig. S2c, Fig. 4).

After translocation of the transfer DNA to its target site the cantilever is moved down. Since the target area is covalently modified with DNA oligomers that are complementary to the anchor sequence a 30 bp duplex in shear geometry is formed (Fig S2d). As the dissociation force of duplexes in shear geometry depends on the length of the DNA sequence the shorter handle sequence ruptures first and the transfer DNA is attached to the target site (Fig. S2e, Fig. 4). The DNA sequences of the oligomers used in this study are shown in Fig. S3.

Hybridization of fluorescent nanoparticles to the DNA scaffold
For the hybridization to the DNA-biotin scaffold, the following fluorescent semiconductor nanoparticles were used:
Invitrogen, Germany, streptavidin conjugate, 1 μM solution, Qdot 525 (colored blue), Qdot 565 (colored green), and Qdot 705 (colored red). The nanoparticles were incubated on the written DNA-biotin pattern at a final concentration of 500 pM in 0.1x SSC buffer. After about one minute, the self assembly process of nanoparticles to the pattern was complete.

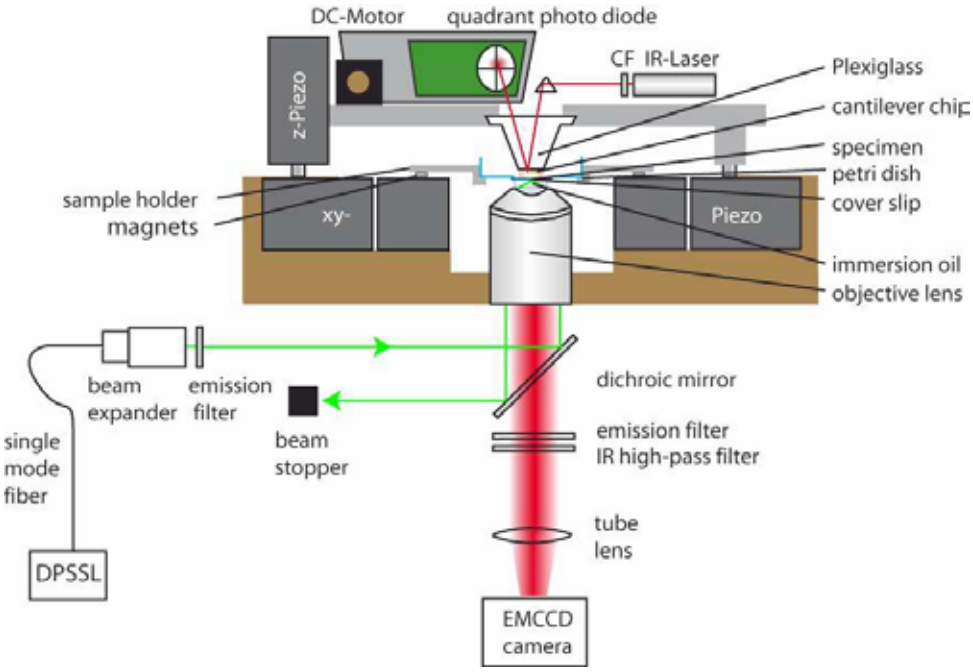

Fig. S1. Experimental setup. A custom built AFM, which is moveable in z direction via a piezo, is combined with an inverted microscope for objective-type TIRF excitation. The cover slip with the depot- and target areas on top is glued into a drilled petri dish. The petri dish is placed in a sample holder, which is fixed through magnets on x-y piezo scanner.

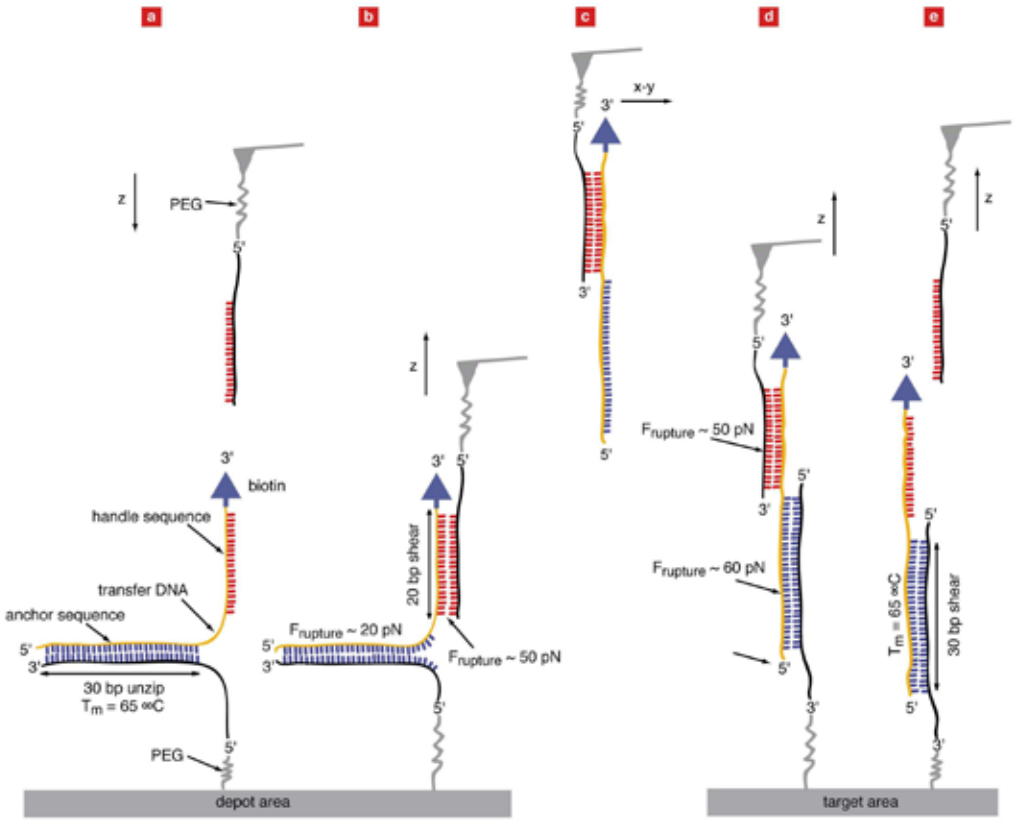

Fig. S2. Schematic illustration of the hierarchical force system. (a) To prevent unspecific adsorption, polyethylenglycol (PEG) molecules are covalently attached to the depot area. DNA oligomers, complementary to the anchor sequence of the transfer DNA, are covalently bound with their 5' end to these PEG molecules. Transfer DNA oligomers, which were modified with biotin labels at the 3' end, are hybridized to this anchor sequences. The tip of an AFM cantilever is also covalently modified with PEG molecules and a single DNA oligomer, which is complementary to the handle sequence of the transfer DNA. (b) When the tip is in contact with the surface a duplex between the transfer DNA and the cantilever DNA is formed. When the tip is retracted, the anchor sequence is loaded in unzip mode and the handle sequence in shear mode. As the unbinding probability for the anchor sequence is higher, the transfer DNA is picked up. (c and d) The target site is also covalently modified with PEG molecules. DNA oligomers, complementary to the anchor sequence of the transfer DNA, are bound with their 3' end to the PEG molecules. After translocation, the tip is moved down and a duplex is formed. When the tip is retracted, the handle and the anchor sequences are loaded in shear mode, but this time the shorter handle sequence ruptures first and the transfer DNA is attached to its target site. The tip is now in its initial state and the cycle can be repeated over and over again.

Fig. S3. Oligomers used in this study. The transfer DNA is 80 bp long and has a biotin label at its 3' end. The 30 bp long sequence on the 5' end is used to anchor the transfer DNA both to the depot and to the target site. The 20 bp long sequence on the 3' end is used as a handle for pick up. All oligomers were synthesized and purified (HPLC-grade) form IBA (IBA GmbH, Göttingen, Germany).

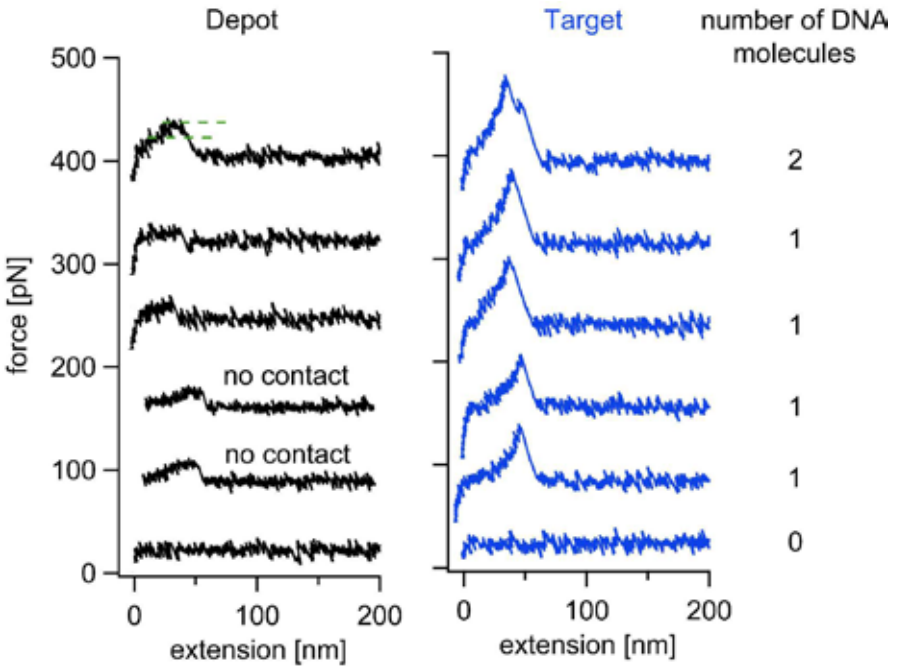

Fig. S4. Typical force extension traces of the depot and target region. In the depot region, the transfer DNA oligomer is separated from the depot oligomer in the zipper geometry. This separation process results in a force plateau of about 18 pN. As indicated, the transfer oligomers can also be picked up without contacting the surface. In the target region the transfer oligomer is separated from the tip oligomer in the shear geometry. Here, the force extension traces follows the elasticity of the PEG-spacer and the DNA until they are separated at forces of about 50 pN. For each cut-and-paste cycle, the number DNA oligomers which were picked up and delivered, can be counted. As an example we show traces where two, one and no DNA molecule was detected.

movie S5. Hybridization of nanoparticles to the DNA scaffold. (separate download)

References:

1. Kufer, S.K., Puchner, E.M., Gumpp, H., Liedl, T. & Gaub, H.E. Single-Molecule Cut-and-Paste Surface Assembly. Science 319, 594-596 (2008).

2. Kühner, F., Lugmaier, R., Mihatsch, S. & Gaub, H.E. Print your atomic force microscope. Rev. Sci. Instrum. 78 (2007).

3. Florin, E.L. et al. Sensing specific molecular interactions with the atomic force microscope. Biosensors and Bioelectronics 10, 895-901 (1995).

4. Butt, H.-J. & Jaschke, M. Calculation of thermal noise in atomic force microscopy. Nanotechnology 6, 1-7 (1995).

5. Strunz, T., Oroszlan, K., Schafer, R. & Guntherodt, H.J. Dynamic force spectroscopy of single DNA molecules. Proceedings of the National Academy of Sciences of the United States of America 96, 11277-11282 (1999).

6. Rief, M., Clausen-Schaumann, H. & Gaub, H.E. Sequence-dependent mechanics of single DNA molecules. Nat Struct Biol 6, 346-349 (1999).

7. Levinthal, C. & Crane, H.R. On the Unwinding of DNA. PNAS 42, 436-438 (1956).

4. Rubinstein, R.H.C. Polymer Physics. Oxford University Press (2005).

5. Oesterhelt, F., Rief, M. & Gaub, H.E. Single molecule force spectroscopy by AFM indicates helical structure of poly(ethylene-glycol) in water. New Journal of Physics 1 (1999).

6. Smith, S.B., Cui, Y.J. & Bustamante, C. Overstretching B-DNA: The elastic response of individual double-stranded and single-stranded DNA molecules. Science 271, 795-799 (1996).

Publikation 2

Optically monitoring the mechanical assembly of single molecules.

Kufer, S. K.; Strackharn, M.; Stahl, S. W.; Gumpp, H.; Puchner, E. M.; Gaub, H. E.; Nat Nanotechnol **2009**, 4 (1), 45-49.

nature nanotechnology

LETTERS

CORRECTED ONLINE: 8 DECEMBER 2008
PUBLISHED ONLINE: 23 NOVEMBER 2008 | DOI: 10.1038/NNANO.2008.333

Optically monitoring the mechanical assembly of single molecules

Stefan K. Kufer[1], Mathias Strackharn[1], Stefan W. Stahl[1], Hermann Gumpp[1], Elias M. Puchner[1,2] and Hermann E. Gaub[1]*

Bottom-up assembly at the level of individual molecules requires a combination of utmost spatial precision and efficient monitoring. We have previously shown how to 'cut-and-paste' single molecules[1], and other groups have demonstrated that it is possible to beat the diffraction limit in optical microscopy[2–4]. Here we show that a combination of single-molecule cut-and-paste surface assembly[1], total internal reflection fluorescence microscopy and atomic force microscopy[5–8] can be used to deposit individual fluorophores in well-defined nanoscale patterns and also to monitor the process in real time with nanometre precision. Although the size of the pattern is well below the optical resolution of the microscope, the individual dyes are identified by localizing the centroids and detecting the photobleaching of the fluorophores. With this combination of methods, individual dyes or labelled biomolecules can be arranged at will for specific functions, such as coupled fluorophore systems or tailored enzyme cascades, and monitored with nanoscale precision.

Objects smaller than the diffraction limit of an imaging system are projected as blurry spots with the size of a Rayleigh disc. However, the centre position of individual fluorophors can be determined with nanometre precision, and the precision is only limited by the number of photons collected from the object[9–12]. Multiple emitters within a diffraction-limited spot may also be localized if their individual contributions to the overall signal can be discriminated either spectrally or by other means. In recent years various techniques, subsumed under the expression super-resolution imaging (SRI), have been developed, which use different methods to extract one high-resolution image from a series of low-resolution images[13–19].

Impressive proof-of-principle experiments for SRI have been reported in the literature, where samples were designed with different fluorophores on defined positions[13,15,16,19]. Predominantly DNA duplexes with modified bases were used as molecular rulers for this purpose. We recently introduced a new means to assemble individual nanoscale functional units, which we term single-molecule cut-and-paste (SMCP). It combines the precision of atomic force microscopy (AFM) with the selectivity of DNA hybridization. Here, we have used this technique to assemble a two-dimensional pattern of individual fluorophores, which we then localized by SRI.

The SMCP system used here makes use of a transfer DNA with an anchor and a handle oligomer carrying a single Cy3 dye molecule. The anchor oligo provides a thermodynamically stable attachment of the transfer DNA in both the depot and the target area. The handle oligo allows pick up of the transfer DNA with the AFM tip and repositioning of the transfer DNA from the depot to the target. The binding geometry and overlap length of the oligomers were chosen such that this cut-and-paste process could be operated in cycles. (See Supplementary Information for details of the underlying hierarchical system of the unbinding forces.)

Figure 1 shows the step-by-step deposition of a single fluorophore that had previously been picked up from the depot area. When the tip is lowered towards the target site (Fig. 1a, black curve), the anchor oligomer hybridizes with a complementary strand. When the tip is withdrawn from the surface, both duplexes are loaded in shear mode, but the shorter handle duplex ruptures first, and the transfer system remains at the target site (Fig. 1b). As force–distance curves of both pick-up and deposition process are recorded, the process can be validated with these characteristic AFM fingerprints (Fig. 1a).

With microfluorescence only a very low background signal is detected when the tip is far away from the surface (Fig. 1c). When the tip penetrates the evanescence excitation field, a strong fluorescence signal from the dye molecule is detected in the green channel of the camera, while the tip is visible in both the red and the green detection channels[20]. When the tip is withdrawn, the signal from the tip vanishes, but the dye emits constantly until it bleaches in a single step. See Supplementary Information, Movie M1, for a detailed demonstration of this deposition event, and Movie M2 for an animation of the SMCP process. The intensity–time trace in Fig. 1d clearly shows the deposition of a single molecule. This bleaching step size in fluorescence intensity remains the same throughout a large number of experiments. Together with the clear signature in the single-molecule force scans during deposition it shows unambiguously that SMCP provides exquisite control of the deposition of individual fluorophores.

The position of this single molecule can now be located by fitting Gaussians to the intensity distribution. To evaluate the mechanical stability of our combined instrument, the fluorophore position of each frame was plotted in Fig. 2a. As can be seen from Fig. 2b,c no systematic drift of the molecule is observed and the standard deviation for the 100 ms localization was determined to be $\pm$13 nm. By summing all images, the signal-to-noise ratio could be improved drastically. This molecule, which remained active for more than 8 s, could thus be located with a precision better than $\pm$1.4 nm. This value is a benchmark for the accuracy with which we can determine the position of a single fluorophore.

Next, the spatial precision of the SMCP process was examined. As was pointed out by Smalley in his dispute with Drexler[21], 'complete' mechanical control over an assembly process at the single-molecule level is hardly possible because of two intrinsic fundamental limitations commonly referred to as the fat and sticky finger problem. SMCP makes use of this seeming limitation in that it uses the selective 'stickiness' between the DNA oligomers used for transfer and assembly. However, the spatial precision of the paste process is then limited by the size of the DNA oligomer, by the

[1]Centre for Nanoscience and Physics Department, University of Munich, Amalienstrasse 54, 80799 Munich, Germany, [2]Centre for Integrated Protein Science Munich, Butenandtstrasse 5 - 13, 81377 Munich, Germany; *e-mail: Gaub@LMU.de

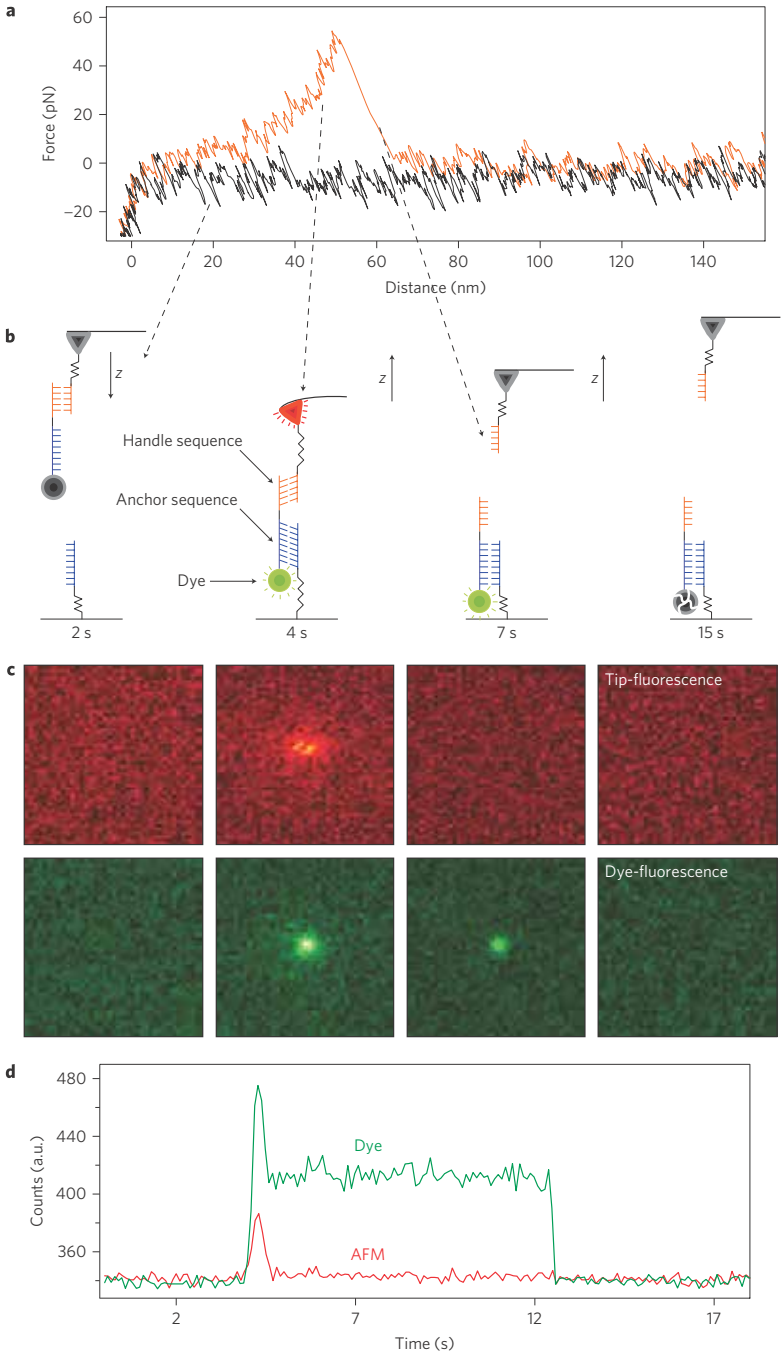

Figure 1 | Monitoring the deposition of a single molecule by AFM and TIRF microscopy. a, A typical force–distance curve of the deposition process. The tip is lowered until it contacts the surface (black curve) and a DNA duplex forms. As the tip retracts, the force increases gradually until the short handle sequence ruptures (red curve). **b**,**c**, As long as the tip is far away from the surface (**b**, 2 s), no fluorescence is detectable (**c**). When the tip penetrates the evanescent excitation field (**b**, 4 s), a strong signal is detected in both the red and green channels (**c**). When the cantilever retracts (**b**, 7 s), the fluorescence from the tip (red) vanishes but the transfer DNA (green) remains anchored and emits photons until it photobleaches (**c**). **d**, Intensity–time traces at the deposition site.

functionalization density of the target area, and by the rotational mobility of the polyethylene glycol (PEG)-spacers used for the covalent attachment of the oligomers to the surfaces. A sketch of this situation is provided in Fig. 3a.

Experimentally, the SMCP precision and the long-term stability of the setup were determined by successively depositing molecules at different positions on the target area. However, because in our setup only the sample is moved, the position of the deposited

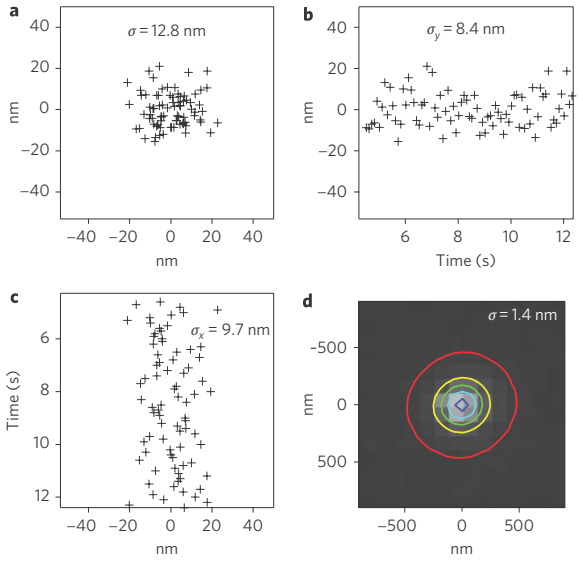

Figure 2 | Localizing single molecules with nanometre precision. **a**, During the lifetime of a single fluorophore deposited in Fig. 1, each frame was fitted with two-dimensional Gaussians. **b**,**c**, Temporal development of the centroid coordinates. **d**, Because the position of the dye is drift-free (**b**,**c**), an average intensity image of this period was summed and fitted with a single Gaussian. The accuracy of the position obtained from the optical part of the instrument was determined to be ±1.4 nm.

molecules relative to the optical axis of the instrument remained constant. For each deposition process a movie was recorded, and the positions of the pasted molecules were determined as described above. The positions of nine single fluorophores deposited in this way in intervals of five minutes are shown in Fig. 3c. The spatial uncertainty of the experiment presented in Fig. 3c arises first from the SMCP process itself, but also from the spatial drift of the setup (Fig. 3d,e). The systematic thermal drift shown in this particular example was chosen to highlight the advantage of our procedure to isolate potential artifacts. An estimate of the SMCP process itself can be given by subtracting the drift (see lines in Fig. 3d,e), resulting in a precision of the y-position of ±11 nm. Under the given conditions of spacer length and anchor density this value can be seen as a benchmark for the precision of deposition. This value agrees well with the predictions of the simple model depicted in Fig. 3a,c, which is the result of the calculation given in the Supplementary Information.

To demonstrate the possibility of assembling and resolving a pattern comprising several single fluorophores we pasted six spots at a distance of 1 μm from one another (Fig. 4a). Each spot was assembled in nine SMCP cycles, as outlined in Fig. 4a. However, on average, a fluorophore was deposited only at every second attempt. Our goal was to identify the location of the pasted molecules by optical means. The intensity-time trace of the 16-pixel diffraction-limited spot no. 4 is shown in Fig. 4b. The stepwise decay with an exponential envelope is a clear indication for uncorrelated subsequent single fluorophore photobleaching. This stepwise decay of the overall intensity is also seen in the sequence of images in Fig. 4c. We used the sequential photobleaching of the fluorophores to discriminate between them in the following way. The last plateau arises from the last single fluorophore. Therefore, the

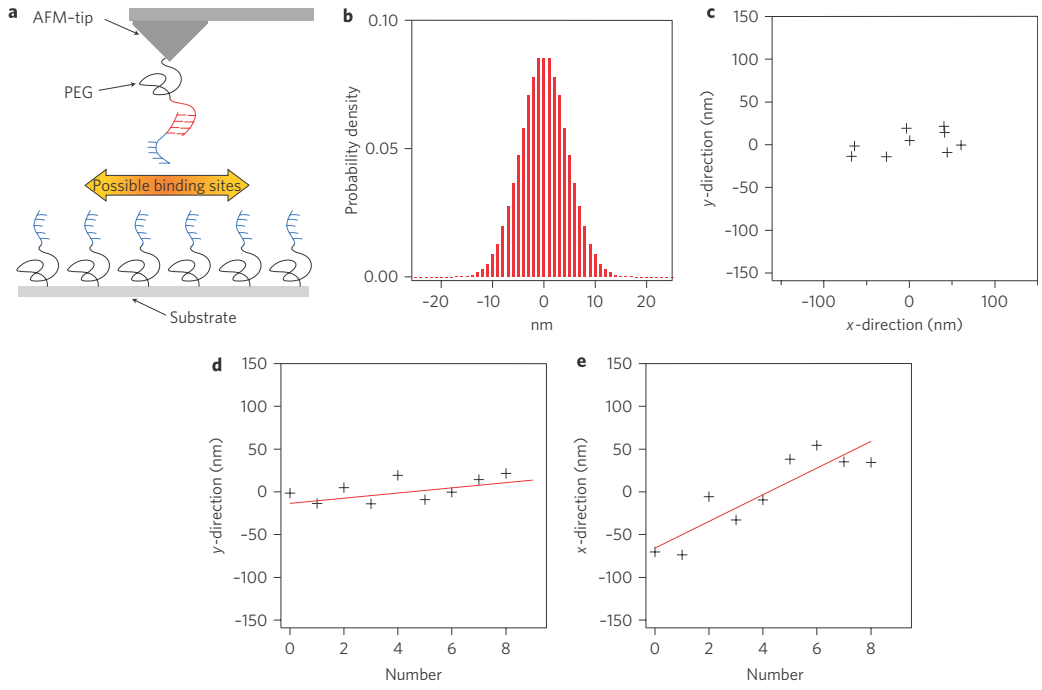

Figure 3 | Positional accuracy of the SMCP process. **a**,**b**, Positional uncertainty occurs when the PEG- and DNA-modified AFM tip probes for potential binding sites. **c**, Uncertainty was measured by successively depositing several single transfer-DNA molecules. The uncertainty of the coordinates of the centroid is determined by both the SMCP process and the spatial drift of the setup. **d**,**e**, To estimate long-term stability, intervals of 5 min between subsequent depositions were chosen and the complete experiment lasted ~45 min. During this time, the instrument drifted laterally and the uncertainty was determined by subtracting this instrumental drift.

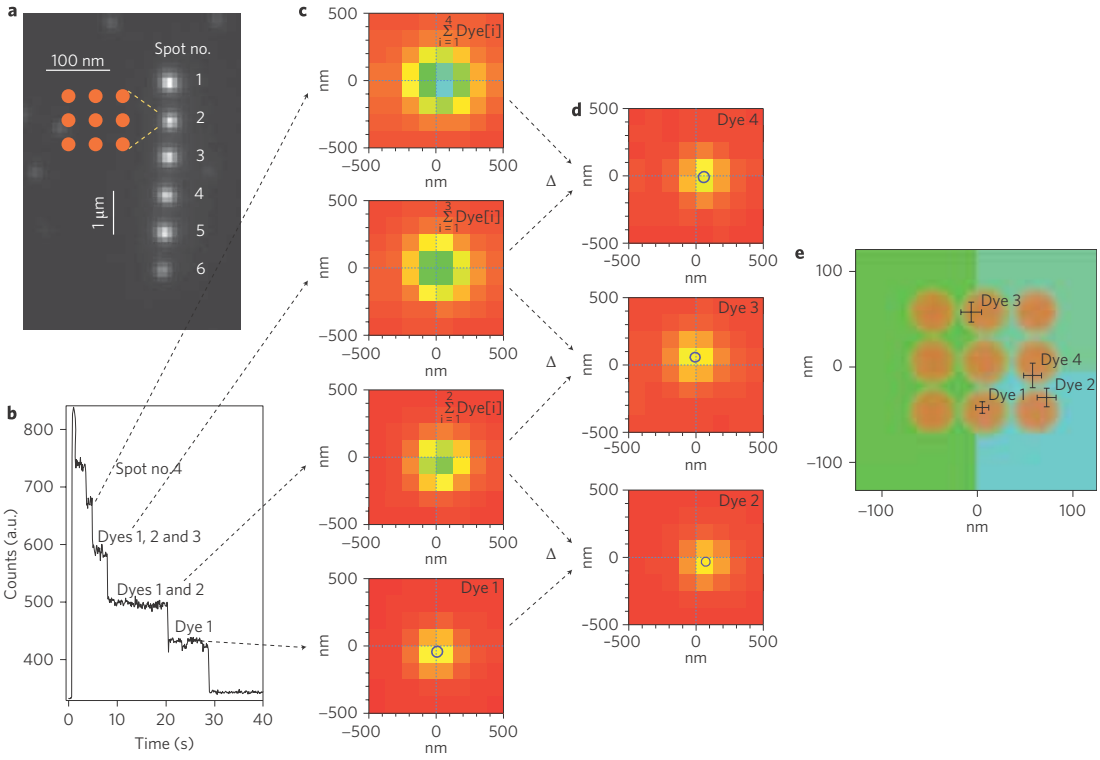

Figure 4 | Determining the position of deposited dyes by photobleaching. a, Fluorescence micrograph of a pattern consisting of six spots at a distance of 1 µm from one another. Each spot was assembled over nine SMCP cycles and deposited as sketched in the inset. **b**, Intensity–time trace of the diffraction-limited spot no. 4. During excitation, the Cy3 labels photobleach and show the typical stepwise decay of single fluorophores. After 20 s only one dye is left. **c**, Average intensity images were calculated for periods of constant signal. **d**, Subsequent images were subtracted to determine the intensity of the photobleached fluorophores, and two-dimensional Gaussians were fitted to each image. **e**, The positions of the four dyes.

centroid of the corresponding image gives its position. The second-to-last plateau arises from the two last fluorophores. We subtracted the image of the last plateau from the image corresponding to the second plateau. The remaining fluorescence distribution must therefore stem from the second-to-last fluorophore, and its centroid was so determined. With this iterative analysis we determined the position of the remaining fluorophores (Fig. 4d). As can be seen in Fig. 4e, the measured positions agree well with the expected positions in the assembly pattern. As can also be seen, the size of the error bars increases with decreasing lifetime of the fluorophore. We therefore restricted our quantitative analysis to the last four molecules. Nevertheless, the precision of the localization of the pasted molecules within the diffraction-limited ensemble by means of SRI turned out to be as good as $\pm$12 nm.

In summary, we have demonstrated that SMCP surface assembly combined with SRI allows the deposition process of single fluorophors to be monitored in real time and also the localization of the deposited molecules with nanometre precision. The precision of the SMCP process was determined to be $\pm$11 nm. This value may be improved considerably by using shorter spacers and with an optimized system of unbinding forces, for example, by using covalent anchor chemistry in the target area. In doing so, patterns of arbitrary shape and with arbitrary numbers of single molecules may be created. Such patterns could be used as test systems for novel SRI techniques, but could also help to investigate dye–dye interactions in a very controlled manner. In this study we have not made use of the potential to assemble different fluorophores in well-defined pattern and to analyse their resulting spectral properties, but such investigations are feasible and are expected to shed new light on the interaction among fluorophores and also between dye molecules and photonic nanostructures or optically active nanoparticles[22,27].

Methods

Sample preparation. Depot and target areas were prepared on a cover slip as described in ref. 1. Briefly, cover slips were amino functionalized and covalently modified with N-hydroxy-succinimide-ester (NHS)–PEG–maleimide (M = 5,000 g mol^{-1}; Nektar). After rinsing with H_2O, a PDMS flow chamber with two channels was mounted on one cover slip. Both channels were connected to a peristaltic pump. The anchor oligomers for the depot and target area were reduced using tris(2-carboxyethyl) phosphine (TCEP) solution (Pierce) in order to generate free mercaptans. The left channel (depot area) was rinsed for 1 h with a 10 µM solution of depot anchor oligomers and the right one (target area) with a 10 µM solution of target anchor oligomers. Afterwards, both channels were rinsed with H_2O to remove all non-covalently bound oligomers. The left channel (depot area) was rinsed with a 1 µM solution of transfer DNA dissolved in saline sodium citrate (SSC) buffer (150 mM NaCl, 15 mM sodium citrate, pH 7) for 1 h. All oligomers used in this study were synthesized by IBA (IBA GmbH) and were of HPLC grade. After rinsing the depot channel for 5 min with SSC buffer to remove all non-hybridized transfer DNA, the PDMS flow chamber was removed and the cover slip was dried in a nitrogen stream. Finally the cover slip was mounted to the AFM–total internal reflection fluorescence (TIRF) sample holder and immersed in SSC buffer.

Total internal reflection fluorescence microscope. Single-molecule fluorescence microscopy was carried out under TIRF excitation. Fluorescence excitation of the Cy3 dyes was performed using a 532 nm, 75 mW DPSS laser (Crystalaser) through a ×100/1.49 oil immersion objective lens (Nikon CFI Apochromat TIRF), with the collimated laser beam focused at the back focal plane of the objective lens such that the beam was totally reflected at the cover slip. Fluorescence light was split by colour with a commercial Dual View (Optical Insights) with Brightline HC 582/75

(Semrock) and ET 700/75 (Chroma) as emission filters for the green and red channels, respectively, and a dichroic mirror with a cutoff wavelength of 630 nm (630DCLP). The emitted light was detected using a 512×512 pixel back-illuminated electron multiplying charge-coupled device (EMCCD) camera (DU-897, Andor). Time series were recorded in frame-transfer mode with an integration time of 100 ms per frame. The EMCCD chip was typically operated at a temperature of −75 °C and an electron multiplication gain of ×300 was used. The magnification was 96; that means one pixel is equivalent to a distance of 125 nm.

AFM measurements. All SCMP experiments were performed with a custom-built AFM[23] at room temperature in SSC buffer. Silicon nitride cantilevers (MLCT-AUHW, Veeco Probes) were amino functionalized and covalently modified with NHS–PEG–maleimide (M = 5,000 g mol^{-1}; Nektar) as described in ref. 24. The spring constant of the DNA-modified cantilever was calibrated in solution using the equipartition theorem[25,26]. This method yielded a spring constant of 12.9 pN nm^{-1} and a resonance frequency of 1.24 kHz for the cantilever used in this study. The tip was withdrawn from the surface at a speed of 1,500 nm s^{-1} until it was 2 μm above the surface. The protocol for the SMCP as well as the data recording was programmed using Igor Pro 5.03 (Wave Metrics). An Asylum Research controller, which provides analog-to-digital converter (ADC) and digital-to-analog converter (DAC) channels as well as a DSP board, was used for setting up feedback loops. Cantilever positioning for pickup and delivery was controlled in closed-loop operation. The precision was set to ±4 nm.

Data analysis. Fluorescence images were analysed with Igor Pro 6.01 (Wave Metrics). Intensity–time traces were produced by calculating the average intensity over 4×4 pixels in every frame. Centroid localization of a single molecule was performed by fitting a two-dimensional Gaussian distribution to an 11×11-pixel diffraction-limited image. For localizing the positions of each fluorophore within a cluster, the individual contributions to the intensity images were extracted by calculating an average intensity image for every period of constant signal, then subtracting subsequent images from each other. The differences indicate the average intensities of the contributing fluorophores. The positions of the fluorophores were again determined by fitting two-dimensional Gaussians.

Received 13 June 2008; accepted 22 October 2008; published online 23 November 2008

References

1. Kufer, S. K., Puchner, E. M., Gumpp, H., Liedl, T. & Gaub, H. E. Single-molecule cut-and-paste surface assembly. *Science* **319,** 594–596 (2008).
2. Hell, S. W. & Wichmann, J. Breaking the diffraction resolution limit by stimulated emission: stimulated-emission-depletion fluorescence microscopy. *Opt. Lett.* **19,** 780–782 (1994).
3. Xie, X. S. & Dunn, R. C. Probing single molecule dynamics. *Science* **265,** 361–364 (1994).
4. Dyba, M. & Hell, S. W. Focal spots of size lambda λ/23 open up far-field fluorescence microscopy at 33 nm axial resolution. *Phys. Rev. Lett.* **88,** 163901 (2002).
5. Binnig, G., Quate, C. F. & Gerber, C. Atomic force microscope. *Phys. Rev Lett.* **56,** 930–933 (1986).
6. Hansma, P. K., Elings, V. B., Marti, O. & Bracker, C. E. Scanning tunneling microscopy and atomic force microscopy: application to biology and technology. *Science* **242,** 209–216 (1988).
7. Radmacher, M., Tillmann, R. W., Fritz, M. & Gaub, H. E. From molecules to cells: imaging soft samples with the atomic force microscope. *Science* **257,** 1900–1905 (1992).
8. Duwez, A. S. *et al.* Mechanochemistry: targeted delivery of single molecules. *Nature Nanotech.* **1,** 122–125 (2006).
9. Bobroff, N. Position measurement with a resolution and noise-limited instrument. *Rev. Sci. Instrum.* **57,** 1152–1157 (1986).
10. Thompson, R. E., Larson, D. R. & Webb, W. W. Precise nanometer localization analysis for individual fluorescent probes. *Biophys. J.* **82,** 2775–2783 (2002).
11. Ober, R. J., Ram, S. & Ward, E. S. Localization accuracy in single-molecule microscopy. *Biophys. J.* **86,** 1185–1200 (2004).
12. Yildiz, A. *et al.* Myosin V walks hand-over-hand: single fluorophore imaging with 1.5 nm localization. *Science* **300,** 2061–2065 (2003).
13. Qu, X., Wu, D., Mets, L. & Scherer, N. F. Nanometer-localized multiple single-molecule fluorescence microscopy. *Proc. Natl Acad. Sci. USA* **101,** 11298–11303 (2004).
14. Betzig, E. *et al.* Imaging intracellular fluorescent proteins at nanometer resolution. *Science* **313,** 1642–1645 (2006).
15. Rust, M. J., Bates, M. & Zhuang, X. Sub-diffraction-limit imaging by stochastic optical reconstruction microscopy (STORM). *Nature Methods* **3,** 793–796 (2006).
16. Gordon, M. P., Ha, T. & Selvin, P. R. Single-molecule high-resolution imaging with photobleaching. *Proc. Natl Acad. Sci. USA* **101,** 6462–6465 (2004).
17. Tinnefeld, P. & Sauer, M. Branching out of single-molecule fluorescence spectroscopy: challenges for chemistry and influence on biology. *Angew. Chem. Int. Ed.* **44,** 2642–2671 (2005).
18. Lacoste, T. D. *et al.* Ultrahigh-resolution multicolor colocalization of single fluorescent probes. *Proc. Natl Acad. Sci. USA* **97,** 9461–9466 (2000).
19. Churchman, L. S., Okten, Z., Rock, R. S., Dawson, J. F. & Spudich, J. A. Single molecule high-resolution colocalization of Cy3 and Cy5 attached to macromolecules measures intramolecular distances through time. *Proc. Natl Acad. Sci. USA* **102,** 1419–1423 (2005).
20. Gaiduk, A., Kühnemuth, R., Antonik, M. & Seidel, C. A. M. Optical characteristics of atomic force microscopy tips for single-molecule fluorescence applications. *Chem. Phys. Chem.* **6,** 976–983 (2005).
21. Baum, R. Nanotechnology: Drexler and Smalley make the case for and against 'molecular assemblers'. *Chem. Eng. News* **81,** 37–42 (2003).
22. Bek, A. *et al.* Fluorescence enhancement in hot spots of AFM-designed gold nanoparticle sandwiches. *Nano Lett.* **8,** 485–490 (2008).
23. Kühner, F., Lugmaier, R., Mihatsch, S. & Gaub, H. E. Print your atomic force microscope. *Rev. Sci. Instrum.* **78,** 075105 (2007).
24. Morfill, J. *et al.* B–S transition in short oligonucleotides. *Biophys. J.* **93,** 2400–2409 (2007).
25. Florin, E. L. *et al.* Sensing specific molecular interactions with the atomic force microscope. *Biosen. Bioelectr.* **10,** 895–901 (1995).
26. Butt, H.-J. & Jaschke, M. Calculation of thermal noise in atomic force microscopy. *Nanotechnology* **6,** 1–7 (1995).
27. Puchner, E. M., Kufer, S. K., Strackharn, M., Stahl, S. W. & Gaub, H. E. Nanoparticle self-assembly on a DNA-scaffold written by single-molecule cut-and-paste. *Nano Lett.* **8,** 3692–3695 (2008).

Acknowledgements

We thank P. Tinnefeld and A. Fornof for helpful discussions. This work was supported by the German Science Foundation, the Nanosystems Initiative Munich (NIM) and Functional Nanosystems (FuNS).

Author contributions

S.K.K. and H.E.G. conceived and designed the experiments and co-wrote the paper. S.K.K., M.S. and S.W.S. performed the experiments. S.K.K. and E.M.P. analysed the data. M.S., S.W.S., H.G. and E.M.P. built the AFM–TIRF setup. M.S., S.K.K. and H.E.G. developed the theoretical model of the SMCP spatial uncertainty.

Additional information

Supplementary Information accompanies this paper at www.nature.com/naturenanotechnology. Reprints and permission information is available online at http://npg.nature.com/reprintsandpermissions/. Correspondence and requests for materials should be addressed to H.E.G.

Supplementary information

Optically monitoring the mechanical assembly of single molecules

Stefan K. Kufer[1], Mathias Strackharn[1], Stefan W. Stahl[1], Hermann Gumpp[1], Elias M. Puchner[1,2] and Hermann E. Gaub[1*]

Hierarchical force system for SMCP:
The probe of an atomic force microscope (AFM) was used to assemble individual single stranded DNA (ssDNA) oligomers carrying dye molecules one by one in aqueous solutions at room temperature. The oligomers were stored on well-defined depot areas, picked up with the tip of an AFM cantilever and reassembled with nanometer precision on a spatial distinct target area. The storage, the pick up and the deposition of the DNA oligomers were realized by using an ordered system of unbinding forces based on DNA interactions.

The dissociation rates of DNA duplexes under load are highly dependent of loading geometries and DNA sequences respectively[1, 2]. When the duplex is stretched along its molecular axis, this means that the DNA duplex is loaded at opposite 5' ends or 3' ends, respectively, one speaks of "shear mode"[1] (Fig. S1e). The topological arrangement when double strands are loaded by pulling on the 5' and 3' extremities of one end of the duplex is called "unzip mode"[3] (Fig. S1a). These two geometries are well distinguishable concerning their dissociation properties under load.

The rupture forces for DNA duplexes loaded in unzip mode are independent both of the length of the DNA oligomer and the loading rate, but vary for G-C and A-T interactions. G-C pairing results in a dissociation force of roughly 20 pN whereas A-T gives rise to roughly 10 pN[2]. The dissociation forces for DNA duplexes loaded in shear geometry depend both on the length and the loading rate[1].

To connect the transfer DNA to the depot a 30 base pair (bp) long anchor sequence with mixed G-C and A-T is used (Fig. S1a). The transfer DNA has in addition to this 30 bp anchor sequence a 20 bp handle sequence for pick up. The AFM-tip is covalently modified with a ssDNA strand. Since this strand is complementary to the handle sequence a duplex is formed as the tip approaches the depot area (Fig. S1b). Then the tip is retraced from the depot the anchor sequence is loaded in unzip mode whereas the handle sequence in shear mode. Although the 30 bp anchor sequence is longer than the 20 bp handle sequence, its unbinding probability under load is much higher than for the handle sequence and the transfer DNA is picked up (Fig. S1c).

[1]Center for Nanoscience & Physics Department, University Munich, Amalienstr. 54, 80799 Munich
[2]Center for Integrated Protein Science Munich
* E-mail: Gaub@LMU.de

After translocation of the transfer DNA to its target site the cantilever is lowered towards the surface. Since the target area is covalently modified with ssDNA oligomers that are complementary to the anchor sequence a 30 bp duplex in shear geometry is formed (Fig S1d). As the dissociation force of duplexes in shear geometry depends on the length of the DNA sequence the shorter handle sequence ruptures first and the transfer DNA is attached to the target site (Fig. S1e). It was shown[4] that a length difference of 10 base pairs (bp) is sufficient to make the rupture of the shorter handle duplex more likely by one order of magnitude than the rupture of the longer anchor duplex. The DNA sequences of the oligomers used in this study are shown in Fig. S2. The experimental setup for the SMCP process is shown in Fig. S3.

Calculation of the SCMP lateral uncertainty:
For an estimation of lateral uncertainty the total construct consisting of the transfer DNA attached to the cantilever DNA that again is bound to the tip by a PEG spacer was treated in the model of the freely jointed chain (FJC) as one polymer with the effective Kuhn length b_{eff}, where b_{eff} was obtained by calculating the weighted average Kuhn length of the three sequences. The weighting coefficients are for each sequence respectively the ratio of sequence contour length to the contour length of the total construct:

$$b_{eff} = \frac{l_{PEG}}{l_{tot}} b_{PEG} + \frac{l_{dsDNA}}{l_{tot}} b_{dsDNA} + \frac{l_{ssDNA}}{l_{tot}} b_{ssDNA},$$

with l_i the contour lengths and b_i the Kuhn lengths. The effective number of Kuhn monomers is then given by $N_{eff} = \frac{l_{tot}}{b_{eff}}$.

The FJC model[5] predicts the distribution of end-to-end distances along each axis as

$$P(x_i) = \sqrt{\frac{3}{2\pi N_{eff} {b_{eff}}^2}} \exp\left(-\frac{3{x_i}^2}{2N_{eff}{b_{eff}}^2}\right).$$

As for the estimation of the binding probability $P_{binding}$, we assume that the approach of the tip to the surface is faster then the polymer fluctuations. In this case every conformation in the lower half-space contributes to the binding probability, such that the binding probability along the x-axis when the molecule approaches the surface in z-direction corresponds to

$$P_{binding}(x) = \frac{1}{A_{norm}} P(x) \int_{-\infty}^{0} P(z)dz = P(x),$$

where the normalization constant A_{norm} equals the definite integral because of the normalized function $P(x)$. So the binding probability is described by the Gaussian function $P(x)$.

It is worth stressing the fact that if the approach of the tip is slow compared to the polymer fluctuations the binding probability shrinks to a point like distribution. This is because of the fact that if the tip is approached to a distance that is in the range of the contour length of the polymer, it will bind preferred in the projection point of the tip. That means that the calculated distribution above is the worst case that could happen.

We testet that simple model by simulating the polymer as freely jointed chain with the parameters b_{PEG}=1.1 nm[5], N_{PEG}=27[6], b_{ssDNA}=1.5 nm[7] and N_{DNA}=8[7], and N_{dsDNA}=1 and

b_{dsDNA}=6.8 nm[7]. Fig. S4 shows that the simulation and the FJC model do match in a satisfactory manner.

References:

1. Strunz, T., Oroszlan, K., Schafer, R. & Guntherodt, H.J. Dynamic force spectroscopy of single DNA molecules. *Proceedings of the National Academy of Sciences of the United States of America* **96**, 11277-11282 (1999).
2. Rief, M., Clausen-Schaumann, H. & Gaub, H.E. Sequence-dependent mechanics of single DNA molecules. *Nat Struct Biol* **6**, 346-349 (1999).
3. Levinthal, C. & Crane, H.R. On the Unwinding of DNA. *PNAS* **42**, 436-438 (1956).
4. Albrecht, C. et al. DNA: A Programmable Force Sensor. Science 301, 367-370 (2003).
5. Rubinstein, R.H.C. Polymer Physics. *Oxford University Press* (2005).
6. Oesterhelt, F., Rief, M. & Gaub, H.E. Single molecule force spectroscopy by AFM indicates helical structure of poly(ethylene-glycol) in water. *New Journal of Physics* **1** (1999).
7. Smith, S.B., Cui, Y.J. & Bustamante, C. Overstretching B-DNA: The elastic response of individual double-stranded and single-stranded DNA molecules. *Science* **271**, 795-799 (1996).

Figures:

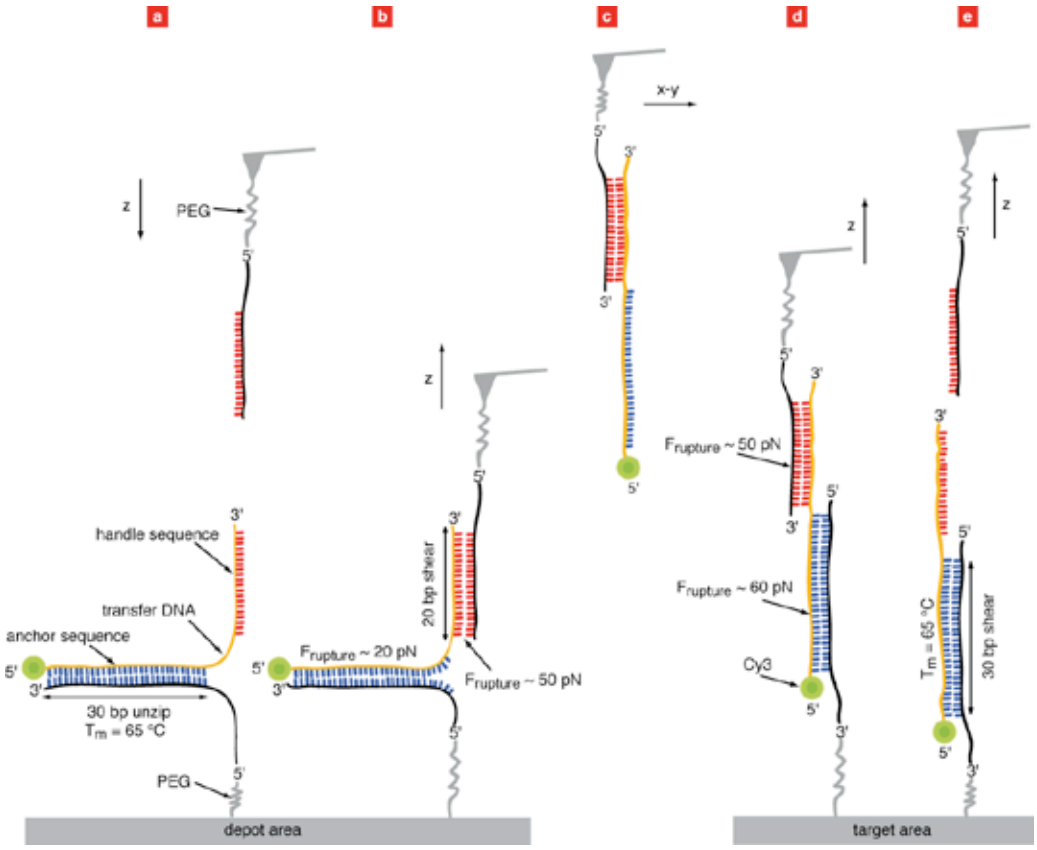

Fig. S1. Schematic illustration of the hierarchical force system. (a) To prevent unspecific adsorption, polyethylenglycol (PEG) molecules are covalently attached to the target area. DNA oligomers, complementary to the anchor sequence of the transfer DNA, are covalently bonded with their 5' end to these PEG molecules. Transfer DNA oligomers, which were modified with Cy3 labels on the 5' end, are hybridized to this anchor sequences. The tip of an AFM cantilever is also covalently modified with PEG molecules and a single DNA oligomer, which is complementary to the handle sequence of the transfer DNA, is bonded covalently with its 5' end to a PEG molecule. (b) When the tip is brought into contact with the surface a duplex between the transfer DNA and the cantilever DNA is formed. When the tip is retracted the anchor sequence is loaded in unzip mode and the handle sequence in shear mode. As the unbinding probability for the anchor sequence is higher, the transfer DNA is picked up. (c and d) The target site is also covalently modified with PEG molecules. DNA oligomers, complementary to the anchor sequence of the transfer DNA, are bonded with their 3' end to the PEG molecules. After translocation the tip is moved down and a duplex is formed. When the tip is retracted the handle and the anchor sequences are loaded in shear mode, but this time the shorter handle sequence ruptures first and the transfer DNA is attached to its target site. The tip is now in its initial state and the cycle could be repeated over and over again.

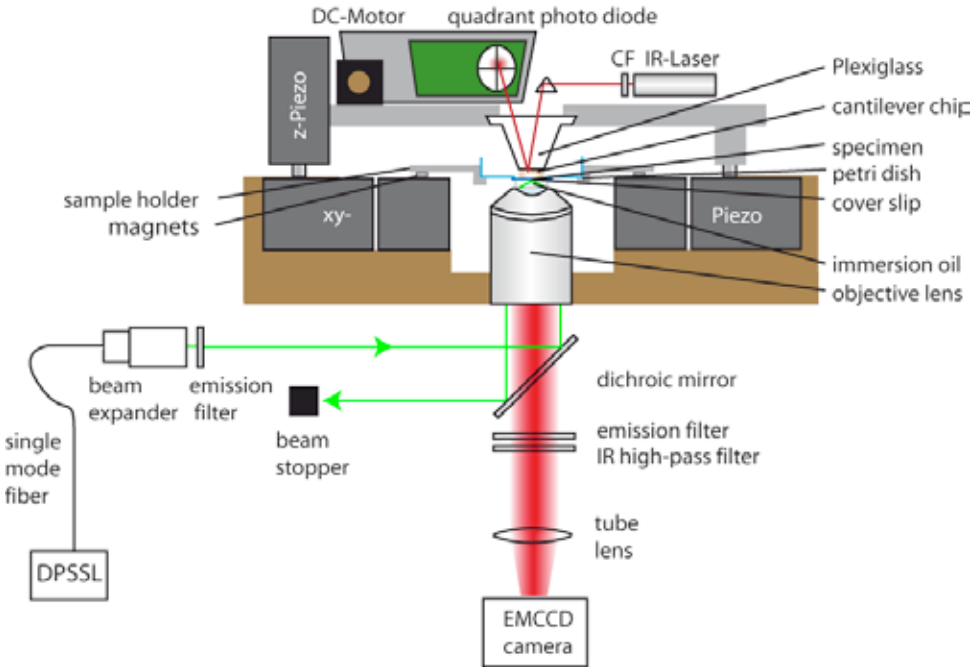

Fig. S3. Experimental setup. A custom built AFM head, which is actuated in z direction via a piezo, is combined with an inverted microscope for objective-type wide-field TIRF excitation. The cover slip with the depot- and target areas on top is glued into a bored petri dish. The petri dish is placed in a sample holder, which is fixed through magnets on x-y piezo scanner.

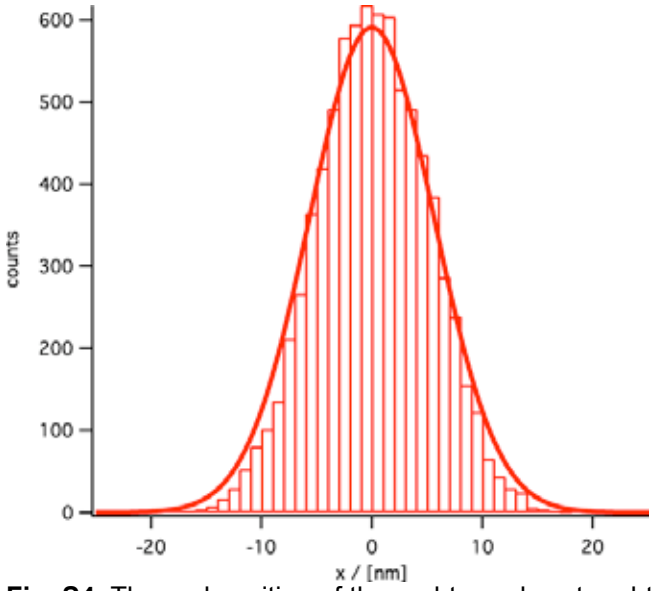

Fig. S4. The end position of the end-to-end vector obtained by simulation of the conjugated polymer in FJC model is shown as histogram, the thick line describes shows the distribution according to the FJC model using an effective Kuhn length an effective monomer number.

Supplementary: (Supplementary.pdf, 340 KB)

The supplementary describes the SMCP force system in detail and provides a simple theoretical model to estimate the precision of the SMCP process.

Movie_M1: (Movie_M1.mov, 1,6 MB)

The movie M1 shows the deposition of a single molecule monitored with single molecule fluorescence microscopy. As long as the tip is far away from the surface (2 s), no fluorescence is detectable. When the tip penetrates the evanescent excitation field (4 s), a strong signal is detected in both the red and green channels. When the cantilever retracts (7 s), the fluorescence from the tip (red) vanishes but the transfer DNA (green) remains anchored and emits photons until it photobleaches.

Movie_M2: (Movie_M2.mov, 2,9 MB)

The movie M2 shows an animation of the SMCP process.

Publikation 3

Ultrastable combined atomic force and total internal reflection fluorescence microscope.

Gumpp, H.; Stahl, S. W.; Strackharn, M.; Puchner, E. M.; Gaub, H. E.; The Review of scientific instruments 2009, 80 (6), 063704.

Ultrastable combined atomic force and total internal fluorescence microscope

H. Gumpp, S. W. Stahl, M. Strackharn, E. M. Puchner,[a] and H. E. Gaub
Chair for Applied Physics and Center for NanoScience, Ludwig-Maximilians-University Munich, Amalienstr. 54, D-80799 Munich, Germany

(Received 7 March 2009; accepted 4 May 2009; published online 22 June 2009)

Combining atomic force microscope (AFM) with other microscopy techniques has expanded the range of potential applications for single molecule investigations dramatically. Particularly hybrid instruments with total internal reflection fluorescence (TIRF) excitation have opened new routes in life sciences. Here we present a novel design for such a hybrid microscope, which overcomes the limitations of conventional combinations caused by their limited mechanical stability. A thorough analysis of the noise spectra and a comparison of the different designs and the different operation modes are given. With this instrument we demonstrate single molecule manipulation by AFM and simultaneous TIRF imaging. © *2009 American Institute of Physics.* [DOI: 10.1063/1.3148224]

I. INTRODUCTION

The atomic force microscope (AFM) has revolutionized nanoscience in many ways. It is now widely used in biophysics as a tool to image nanoscale structures, as well as to measure and apply forces in a well-defined manner.[1–3] While AFM techniques are very precise in terms of spatial and force resolution, even the fastest AFMs currently are orders of magnitude slower in terms of imaging compared to optical methods.[4] On the other hand traditional optical microscopy provides fast readout but is limited by diffraction. Therefore it is obvious that AFM and single molecule fluorescence microscopy are complementing each other in a favorable manner.[5–7] As the AFM is a tool to operate on surfaces, the choice of total internal reflection fluorescence (TIRF) as illumination source for single molecule microscopy is convenient. However positional noise of the sample on the nanometer length scale that could have been neglected in sole single molecule TIRF microscope setups become an issue. Such fluctuations hamper high-precision AFM measurements.

In previous studies we have investigated in great detail the effect of mechanical vibrations of the AFM on the measured unbinding forces of molecular complexes.[8] It is obvious that a fluctuating cantilever, but in the same way a fluctuating sample position, causes force fluctuations in the molecular complex under investigation, which add to the externally applied force. Since bond rupture is a nonequilibrium process, these fluctuations do not average out to zero but reduce the force, which has to be applied externally to break the bond. Particularly when stiff and short handles are used as linkers, fluctuation in the relative distance between tip and sample surface may lead to drastic artifacts.

In optical microscopy, such fluctuations, e.g., caused by vibrations of the microscope, stay often unnoticed since they are below the optical resolution limit. It is particularly the direct coupling of mechanical noise via the oil immersion, which is essential for TIRF, which causes severe problems. Also in high-resolution fluorescence techniques such as 4π-stimulated emission depletion (STED), photo-activated localization microscopy (PALM), or stochastic optical reconstruction microscopy (STORM) such fluctuations remain unnoticed, since their characteristic time typically lies above the integration time of the detectors and thus are averaged out. Not so in mechanical experiments, where such position fluctuations result in force fluctuations which may result in bond ruptures. To cope with this issue we analyzed potential sources of such fluctuations and as a consequence of our analysis developed a very compact microscope setup featuring a solid connection between an immersion objective lens, the AFM, and the sample. By mechanically decoupling the focusing mechanism from the sample and the AFM head, vibrations limiting the force resolution could be eliminated virtually completely.

II. SAMPLE POSITION FLUCTUATIONS IN TIRF MICROSCOPY

Several different methods are commonly used for fluorescence excitation in the evanescent field (TIRF).[9,10] Whereas prism-based systems allow for use of variety of glass substrates and incident angles, and are not limited by the numerical aperture (NA) of the objective lens, combining them with an AFM is difficult. An objective-type TIRF setup installed on an inverted microscope as it was introduced by Tokunaga *et al.*[11] offers the advantage of using an objective lens with high numerical aperture for excitation as well as for collection of emission, therefore leaving the upper half space above the sample free. A scanning probe microscope (SPM) such as the AFM may then be placed above the sample for simultaneous imaging, force measurements, and manipulation of the sample. Several implementations of this concept are already reported in the literature.[5–7,12–15]

Since high NA-objective lenses have very short working distances, objective-type TIRF can only be performed on

[a]Center for Integrated Protein Science Munich.

thin cover slips, with a thickness of up to 0.15 mm. These thin glass substrates are prone to deformation and vibrations, coupling through the system acoustically an even more important mechanically, and through the air, which hampers high-resolution AFM measurements. While sound coupling into the system can be damped effectively by placing the whole setup in a soundproof box, mechanical vibrations are still hard to handle. Oscillations below 100 Hz, as arising from the building, can be effectively damped by active tables, but higher frequencies and especially noise sources inside the microscope itself still have to be eliminated.

A high NA-objective lens needs immersion oil to be operated to match the refractive index of the glass substrate. When using the objective lens for adjusting the focus, as it is done with virtually all commercially available objective-type TIRF setups so far, additional vibrations from, e.g., a focusing piezo are coupled into the glass cover slip. Moreover, moving the objective lens for controlling the focus during the experiment introduces drift mediated by the immersion oil's viscosity. However, for TIRF illumination the focus needs to be adjusted very precisely, because the evanescent field is only a few hundred nanometers in depth. During long measurements temperature changes as well as buffer evaporation may cause the surface to drift out of focus. Hence when operating commercially available focus piezo stages of the objective lens in a closed loop in order to correct for this focus drift, strong vibrations couple into the sample through the immersion oil, thereby making high-resolution AFM experiments virtually impossible.

III. HYBRID TIRF/AFM

In the evolution of SPMs, compact designs, as rigid as possible, have proven to minimize both vibrations and thermal drift. This design principle should provide the best solution for the problems with the mechanical stability discussed above.[16]

We kept our AFM head as short and compact as possible (see Fig. 1). Cantilever deflection is measured with an infrared superluminescent laser diode SLD-37-HP (Superlum Diodes Ltd, Cork, Ireland), which minimizes interferences of the reflected beam and keeps the entire optical spectrum open for fluorescent measurements. Servo motors controlling the z-position of the head and the position of the deflection sensing photodiode allow for automatic compensation of lever and probe drift during long term measurements.

The major difference of the presented setup to yet existing ones is the optimization of the mechanical stability of the sample-cantilever entity. Whereas in conventional microscopes the objective lens is mounted on a revolver and/or focusing piezo, our setup contains a high NA-objective lens, which is rigidly mounted in a massive aluminum block directly connected to the AFM head, as Fig. 1 shows. This way the objective is integrated directly in the AFM head, maximizing the mechanical stability. The sample is located on the cover slip, glued over a hole drilled into the bottom of a Petri dish. The latter is clamped tightly to the xy-piezo scanner by strong magnets in order to be able to move the sample. It is adjusted with micrometer screws for coarse alignment. Modern objective lenses with high NA, such as the Nikon 100× lens (CFI Apo TIRF 100×, NA 1.49, Nikon Inc., Tokyo, Japan) we used here, allow variation in the penetration depth of the evanescent field, depending on the distance of the beam from the rim of the objective lens. This is achieved by shifting the laser orthogonally to the optical axis of the objective lens. This way the penetration depth can be varied between approximately 200–500 nm.

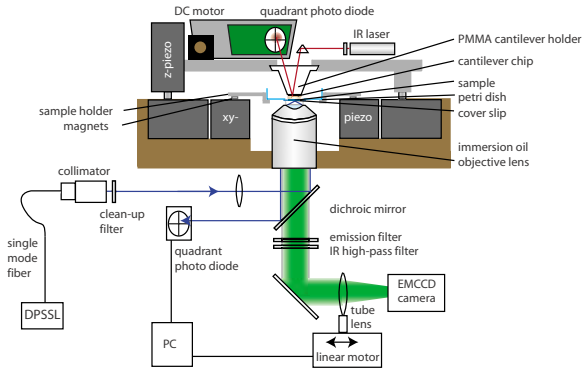

FIG. 1. (Color online) Schematic drawing of the combined AFM/TIRF microscope. TIRF excitation is performed by a diode pulsed solid-state laser coupled to a single-mode fiber. Using a collimator lens and a biconcave lens for focusing the beam on the back focal plane of the objective lens, wide-field TIRF illumination is achieved. Fluorescence emission passes through an appropriate filter set and is collected by the EMCCD camera. The tube lens is used for focusing and therefore mounted on a linear translation stage controlled by a PC that reads the position of the back-reflected beam from a quadrant photo diode. With this feedback a constantly sharp image can be ensured.

Focusing is facilitated by moving the tube lens via a motorized high-accuracy linear translation stage M-605, (Physik Instrumente, Karlsruhe, Germany) which focuses the fluorescence light from the sample onto the chip of the electron multiplying charge coupled device (EMCCD) camera (Andor iXon DU-897, Andor Technology, Belfast, Ireland). This motor is completely mechanically decoupled from the rest of the instrument and does not need to stand on the vibration insulation table.

In order to build a most compact instrument, for the excitation path, the light of a solid-state diode pulsed laser (532 nm DPSS Laser, CrystaLaser, Reno, NV, USA) is coupled into a single-mode optical fiber and used for fluorescence excitation via a compact slider unit consisting of a collimator lens, a clean-up filter, a lens for focusing the beam into the back focal plane of the objective lens, and an adjustable dichroic mirror that directs the light to the sample. This unit can be replaced easily with another one containing an alternative filter set, when working with a different laser. In total internal reflection the back-reflected beam hits a quadrant photo diode, which measures its position. This way a change in the lateral position of the reflected beam and hence a change in distance between the objective lens and the cover slip can be determined. Finally this information can be used for the adjustment of the focus via the tube lens.

By moving the tube lens via the linear translation stage, the relative distance from the charge coupled device chip and therefore the magnification is altered. This effect can be

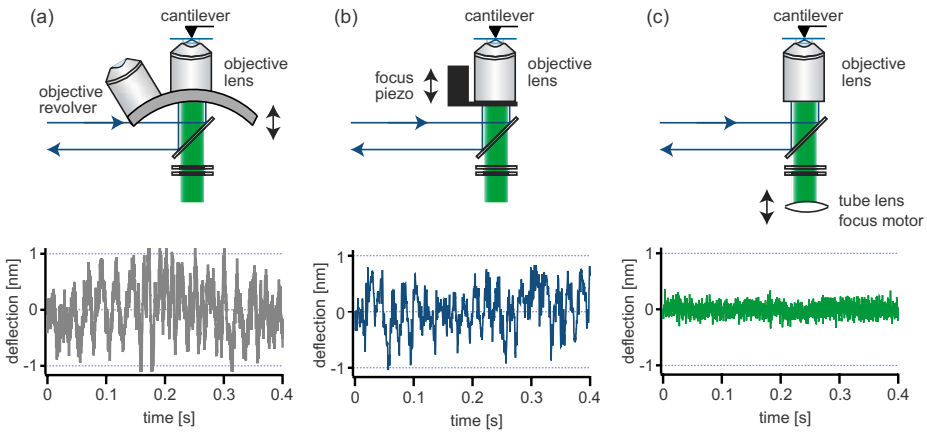

FIG. 2. (Color online) Calculated change in magnification as a function of the tube lens position, respectively, the corresponding sample position for the presented home-built microscope.

quantified by elementary optics, reducing the microscope to a one-lens system. The resulting focal length f and the position of the principal planes H_1 and H_2 are determined by the focal lengths of the objective f_1, the tube lens f_2, and their relative distance d as follows.

$$f = \frac{f_1 f_2}{f_1 + f_2 - d}, \quad H_2 = \frac{d f_2}{f_1 + f_2 - d}.$$

With the given image distance $b = f_2 + x - H_2$ the object distance $g = fb/(b-f)$ and the magnification $M = b/g$ can be calculated for each tube lens position x. Figure 2 shows the results for the described setup. Typical sample drift of 1 μm can be corrected by moving the tube lens by about 10 mm. In this range the magnification changes stay below 0.5%. Even when moving the tube lens by the maximum range of the linear motor ($\pm$25 mm) the change in magnification is below 2.0%. This effect has thus of minor influence on the imaging qualities of the microscope, also in terms of aberration correction.

IV. EXPERIMENTAL RESULTS

In order to compare the setup described above with other combined AFM-TIRF hybrids we measured the height fluctuations of the cover slip. For quantification amplitude spectra were taken with an AFM cantilever contacting the surface. All measurements were performed using a Veeco MLCT-C Cantilever at a contact force of approximately 1 nN. As first reference we used a home-built compact AFM-TIRF microscope with piezo adjustable objective lens. As a second reference a commercially available setup consisting of standard inverted microscope Zeiss Axiovert 200F, (Carl Zeiss AG, Jena, Germany) with a MFP-3D AFM, (Asylum Research, Santa Barbara, CA) and alternatively a Nanowizard II AFM (JPK Instruments, Berlin, Germany) was used. The results are plotted in Figs. 3 and 4 for direct comparison.

The combined conventional setup [Fig. 4(a)] shows the highest noise of all. Since the spectra recorded with the different AFM heads were virtually indistinguishable we conclude that the mechanics of the inverted microscope dominates the resonances. The bridge of the inverted microscope acts as a tuning fork. Vibrations are transduced via the objective revolver through the immersion oil, leading to fluctuations of the sample of approximately 1 nm and more. For high-resolution single molecule force spectroscopy such fluctuations are not tolerable!

Using a piezo driven single objective lens directly attached to the AFM such as in the home-built setup used as reference is an improvement, but as soon as the focusing piezo is operated in closed loop, simultaneous AFM measurement become very noisy [Fig. 4(b)]. Vibrations at the electrical carrier frequency of 50 Hz (and multiples) as well as other resonance frequencies of the instrument become clearly visible. As the spectra in Fig. 3 show, not only in the active focus regulation mode, but even in a passive mode with the feedback switched off, the vibrations in the microscope are coupled through the objective into the sample.

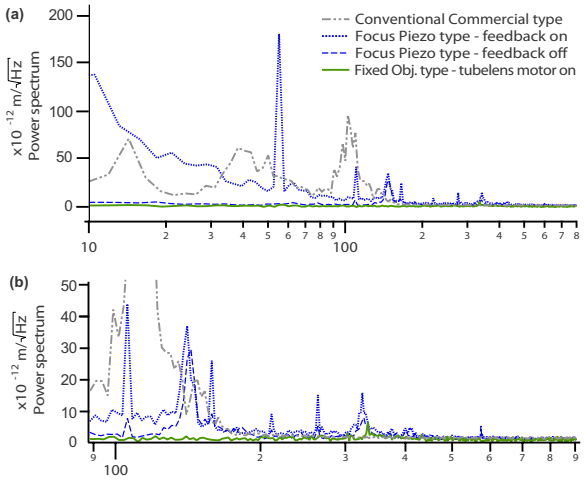

FIG. 3. (Color online) (a) Noise spectra of sample fluctuation recorded on the surface. While the conventional setup shows a broad distribution of frequencies, the home-built microscope with focus piezo exhibits mainly sharp resonance peaks, even when the closed-loop feedback of the focus piezo is switched off. The noise level is drastically reduced in the setup with fixed objective lens even with the tube lens focus motor switched on. A magnified view is given in (b).

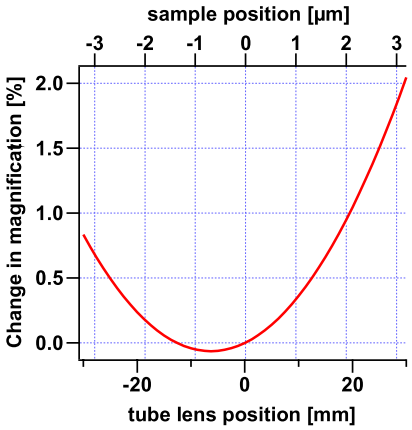

FIG. 4. (Color online) Comparison of the different setups and corresponding height fluctuations of the cover slip surface taken by contacting the surface of the cover slip with the AFM cantilever tip. (a) represents the combination of a standard inverted microscope and a commercial AFM head, (b) shows a setup with objective lens focus piezo, and (c) the new approach with moveable tube lens for focusing.

Moreover, adjusting the focus by moving the objective lens introduces drift that gets especially disturbing when performing experiments over hours.

In contrast, when operating the new setup with fixed objective but moveable tube lens cover slip vibrations are reduced to a minimum, while a sharply focused optical image is assured at all times [Fig. 4(c)]. Spectra that were taken while readjusting the focus position are virtually indistinguishable from those with fixed focus since the movable tube lens is mechanically decoupled from the AFM/sample part.

The combined AFM-TIRF instrument presented here was successfully used for simultaneous single molecule experiments such as single molecule cut-and-paste procedures as described in Ref. 17. Using molecular handles with hierarchical forces fluorescently labeled biomolecules were picked up from a depot, transported, and deposited with about 10 nm precision to a target area (Fig. 5). Figure 5(b) shows the rupture force curves measured on the depot area (left) and the target area (right), which exhibit very small noise comparable to a stand-alone AFM. The focusing mechanism described above made it possible to obtain sharp images of single fluorophores [Figs. 5(c) and 5(d)] at all times while allowing for high-resolution force spectroscopy in parallel for many hours.

V. CONCLUDING REMARKS

During day-to-day use, this combined TIRF-AFM setup proved to be a versatile instrument for many kinds of single molecule experiments.[17–19] The compact design with decoupled focusing succeeded in reaching a maximum of force resolution on the AFM side, while at the same time assuring a constantly sharp image for state-of-the-art single molecule microscopy.

Although we only show here only the combination of TIRF microscopy and AFM force spectroscopy, the principle of the setup described above can also be applied to any combinations of optical and SPMs where high sensitivity and

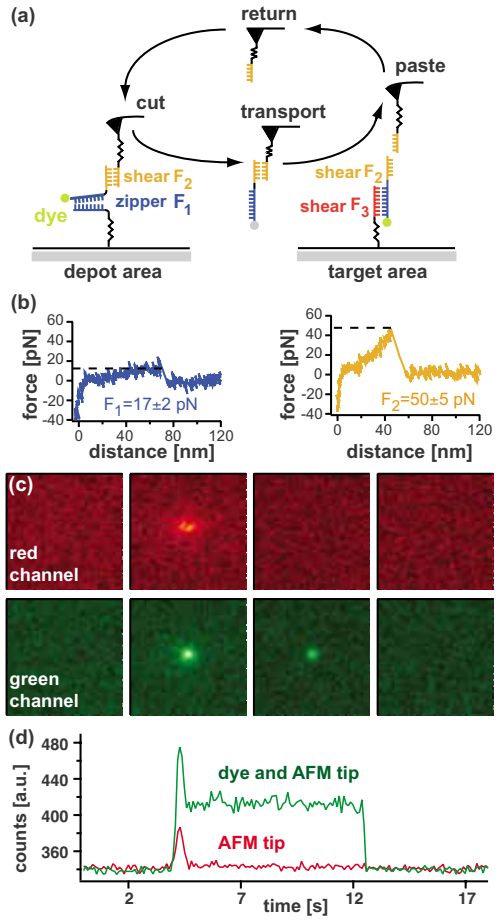

FIG. 5. (Color online) Single molecule cut-and-paste experiment performed using the combined TIRF-AFM microscope. (a) Fluorescently labeled DNA strands are transported by the AFM using a specific handle sequence on the tip and an anchor sequence on the cover slip surface. (b) High-resolution force spectra (d) and single molecule fluorescence time traces could be recorded simultaneously for many hours.

nanometer resolution is required. If no laser is used for TIRF excitation of the sample, or the laser's wavelength would interfere with the measurements, an IR laser could be used instead for determination of the cover slip distance by measuring the position of the totally reflected beam. Looking ahead, future AFM heads could already include an objective lens built in. This would not only allow for placing them directly on any (commercial) inverted microscope, but also would lower the AFM's center of mass, hence making it even more inert to interfering vibrations.

ACKNOWLEDGMENTS

We thank Ferdinand Kühner, Matthias Erdmann, and Jan Opfer for helpful discussions. This work was supported by the Nanosystems Initiative Munich (NIM) and the Stiftung Volkswagenwerk.

[1] A. Engel and H. E. Gaub, Annu. Rev. Biochem. **77**, 127 (2008).
[2] E. M. Puchner, A. Alexandrovich, A. L. Kho, U. Hensen, L. V. Schäfer, B. Brandmeier, F. Gräter, H. Grubmüller, H. E. Gaub, and M. Gautel, Proc. Natl. Acad. Sci. U.S.A. **105**, 13385 (2008).

[3] M. Rief, M. Gautel, and H. E. Gaub, Adv. Exp. Med. Biol. **481**, 129 (2000).
[4] P. K. Hansma, G. Schitter, G. E. Fantner, and C. Prater, Science **314**, 601 (2006).
[5] A. Hards, C. Zhou, M. Seitz, C. Bräuchle, and A. Zumbusch, ChemPhysChem **6**, 534 (2005).
[6] C. G. Morgan and A. C. Mitchell, J. Microsc. **222**, 48 (2006).
[7] L. Peng, B. J. Stephens, K. Bonin, R. Cubicciotti, and M. Guthold, Microsc. Res. Tech. **70**, 372 (2007).
[8] F. Kuhner and H. E. Gaub, Polymer **47**, 2555 (2006).
[9] D. Axelrod, N. L. Thompson, and T. P. Burghardt, J. Microsc. **129**, 19 (1983).
[10] D. Axelrod, J. Biomed. Opt. **6**, 6 (2001).
[11] M. Tokunaga, K. Kitamura, K. Saito, A. H. Iwane, and T. Yanagida, Biochem. Biophys. Res. Commun. **235**, 47 (2006).
[12] T. Funatsu, Y. Harada, H. Higuchi, M. Tokunaga, K. Saito, Y. Ishii, R. D. Vale, and T. Yanagida, Biophys. Chem. **68**, 63 (1997).
[13] A. Trache and G. A. Meininger, J. Biomed. Opt. **10**, 064023 (2005).
[14] A. Valbuena, J. Oroz, A. M. Vera, A. Gimeno, J. Gómez-Herrero, and M. Carrión-Vázquez, Rev. Sci. Instrum. **78**, 113707 (2007).
[15] T. Yamada, R. Afrin, H. Arakawa, and A. Ikai, FEBS Lett. **569**, 59 (2004).
[16] J. B. Thompson, B. Drake, J. H. Kindt, J. Hoskins, and P. K. Hansma, Nanotechnology **12**, 394 (2001).
[17] S. K. Kufer, E. M. Puchner, H. Gumpp, T. Liedl, and H. E. Gaub, Science **319**, 594 (2008).
[18] E. M. Puchner, S. K. Kufer, M. Strackharn, S. W. Stahl, and H. E. Gaub, Nano Lett. **8**, 3692 (2008).
[19] S. K. Kufer, M. Strackharn, S. W. Stahl, H. Gumpp, E. M. Puchner, and H. E. Gaub, Nat. Nanotech. **4**, 45 (2008).

Publikation 4

Resolving Single-Molecule Assembled Patterns with Superresolution Blink-Microscopy.

Cordes, T.†; Strackharn, M. †; Stahl, S. W.; Summerer, W.; Steinhauer, C.; Forthmann, C.; Puchner, E. M.; Vogelsang, J.; Gaub, H. E.; Tinnefeld, P.; Nano Lett 2010, 10 (2), 645-651.

† Die Autoren haben gleichermaßen zu dieser Publikation beigetragen.

NANO LETTERS

pubs.acs.org/NanoLett

Resolving Single-Molecule Assembled Patterns with Superresolution Blink-Microscopy

Thorben Cordes,† Mathias Strackharn,† Stefan W. Stahl, Wolfram Summerer, Christian Steinhauer, Carsten Forthmann, Elias M. Puchner, Jan Vogelsang, Hermann E. Gaub, and Philip Tinnefeld*

Applied Physics—Biophysics and Center for NanoScience, Ludwig-Maximilians-Universität, Amalienstrasse 54, D-80799 München, Germany

ABSTRACT In this paper we experimentally combine a recently developed AFM-based molecule-by-molecule assembly (single-molecule cut-and-paste, SMCP) with subdiffraction resolution fluorescence imaging. Using "Blink-Microscopy", which exploits the fluctuating emission of single molecules for the reconstruction of superresolution images, we resolved SMCP assembled structures with features below the diffraction limit. Artificial line patterns then served as calibration structures to characterize parameters, such as the labeling density, that can influence resolution of Blink-Microscopy besides the localization precision of a single molecule. Finally, we experimentally utilized the adjustability of blink parameters to demonstrate the general connection of photophysical parameters with spatial resolution and acquisition time in superresolution microscopy.

KEYWORDS Superresolution microscopy, single-molecule cut-and-paste, superresolution calibration, single-molecule fluorescence, blink-microscopy, atomic force microscope (AFM)

Modern fluorescence microscopy techniques localize the position of individual molecules with nanometer precision,[1] and by temporally separating the fluorescence of the emitters allow subdiffraction resolution imaging of complex samples such as biological specimen.[2−7] The so-called Blink-Microscopy belongs to this class of techniques[7] that can find a broad range of novel applications in cell biology as well as material sciences. This in turn has raised fundamental questions on the interplay between fluorophore density and achievable resolution as a function of the specific parameters of the method and the fluorescent probes used.

A thorough validation of novel superresolution microscopy techniques requires well-defined samples with programmable positions of individual fluorophores. Prominent examples for bottom-up approaches to assemble such structures are DNA-origami,[8,9] dip-pen nanolithography,[10] nanopipette deposition,[11] or a "one-by-one" assembly, for example, single-molecule cut-and-paste (SMCP) surface assembly.[12−14] In this paper, we combine SMCP surface assembly with superresolution microscopy based on the subsequent localization of single fluorophores termed Blink-Microscopy. We used SMCP to create structures with subwavelength size features and used Blink-Microscopy to resolve these structures. We then assembled calibration patterns by SMCP and used them to clarify questions regarding blink parameters, achievable resolution, and maximal resolvable fluorophore density. In particular, we experimentally demonstrate the trade-off between spatial resolution and acquisition time of Blink-Microscopy and related approaches.[7,15,16]

SMCP is based on the bottom-up assembly of DNA-oligomers and offers a spatial precision down to a few nanometers for placing single molecules (see Figure 1a,b).[13] The units to be assembled, here fluorophore-labeled DNA, are picked up with an AFM tip from a depot and transferred to a target area (Figure 1, see Supporting Information, Material and Methods for details). The directionality of the process is provided by a hierarchical force system and the selectivity of DNA hybridization. The bond of the transfer DNA to the DNA immobilized at the cantilever tip is stronger than the one to the DNA in the depot area. DNA immobilized in the target area, finally, is mechanically most stable. As this process may be repeated several thousand times with the same AFM tip, SMCP allows the assembly of arbitrary structures in two dimensions. Since the small molecules are often assembled on soft surfaces, it is difficult to resolve the structures from their topology. Previous attempts to monitor the positions of molecules placed at subwavelength distances were limited to only a few single molecules.[13]

On the other hand, superresolution fluorescence microscopy has tremendously evolved over the last years starting out with stimulated emission depletion (STED) microscopy.[17,18] More recent techniques are based on the subsequent localization of single molecules and utilize the fact that the position of a single emitter, detected in a wide-field microscope, can be determined with nanometer precision. To this end the fluores-

* To whom correspondence should be addressed. E-mail: philip.tinnefeld@lmu.de. Fax: +49 89 2180 2005.

†These authors contributed equally to this work.

Received for review: 11/8/2009
Published on Web: 12/17/2009

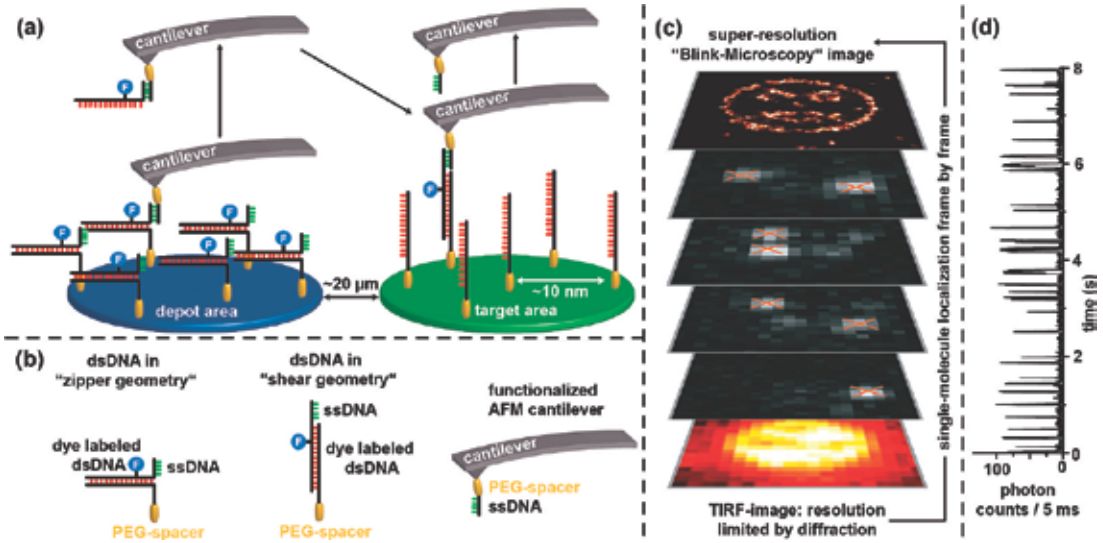

FIGURE 1. (a) Schematic illustration of single-molecule cut-and-paste and (b) corresponding caption. (c) Illustration of superresolution microscopy based on the subsequent localization of "blinking" fluorophores. (d) Fluorescent transient of a single immobilized ATTO655 molecule in aqueous PBS-buffer obtained by confocal microscopy (addition of 50 μM ascorbic acid in the presence of oxygen, excitation at 640 nm with 4 kW/cm^2).

cence of the molecules within the area of one point-spread-function is separated in time by switching all except one molecule into a nonfluorescent dark state (Figure 1c). This switching is achieved, for example, using photoswitchable fluorophores (PALM, STORM, FPALM, dSTORM)[3−6,19,20] or generic metastable dark states of the fluorophores such as radical ion states (Blink-Microscopy, GSDIM).[7,16,21−23] In Blink-Microscopy, for example, continuous ON/OFF-switching of the fluorophores is controlled by electron-transfer reactions. The environment of the fluorophore provides reductant molecules that induce the formation of radical anion states with a lifetime of nanoseconds to minutes.[7,16,24] The lifetime of these metastable OFF-states can be controlled by the oxidant concentration that restores the fluorophore in the fluorescent singlet manifold. The number of counts per cycle (ON-counts) is controlled by the reductant concentration and the ON-time is additionally adjusted by varying the excitation intensity. Blinking in single-molecule fluorescence transients reflects this redox cycle (Figure 1d).[16] Figure 1c illustrates the process of reconstructing superresolution images from movies of blinking molecules in which each single molecule is localized using a Gaussian fit.

For techniques that rely on the subsequent localization of single molecules, resolution is not clearly defined and a thorough characterization has not been performed due to the lack of calibration structures. The main factor in terms of resolution is the localization precision of single molecules, which is closely related to the number of photons detected per ON-state and the signal-to-noise ratio.[25] However, other factors that have not yet been included in a formula contribute to the achievable resolution of superresolution techniques such as the label size, the molecular and labeling density (e.g., the Nyquist criterion has to be met),[15] and the fraction of molecules that are actually (photo)activated and not photobleached. In addition, for techniques with spontaneous formation of the fluorescent form, the ratio of OFF- to ON-times (τ_{off}/τ_{on}) limits the number of fluorophores that can actually be colocalized within one diffraction limited area.[7] While this limitation obviously applies to Blink-Microscopy and related realizations of superresolution microscopy,[7,21−23] it is also important for techniques that apply photochromic molecules due to common spontaneous activation of, for example, fluorescent proteins and cyanine dyes or in case of the two wavelengths for switching and readout are used simultaneously.[26] Hitherto, the resolving power of superresolution microscopy has commonly been demonstrated with comparably undefined filamentous proteins such as actins and microtubules that were stained in vitro or in fixed cells. Test and calibration systems are required that have a defined structure with a known number of fluorophores to quantify the factors influencing resolution and to make the different techniques comparable with each other.

Recently, the use of dye-labeled DNA-origami as a nanoscopic distance ruler serving as a calibration standard for superresolution microscopy was established.[9] Here, two fluorophores with designed distance were suggested for calibrating superresolution microscopes. In contrast to this work, we now created structures by the complementary SMCP approach to demonstrate that complex structures, which are not resolvable by conventional microscopy, can be resolved utilizing Blink-Microscopy. In detail, the flexibility of SMCP was used to assemble complex structures with more than a hundred fluorophores that served for a characterization of parameters that influence resolution of

DOI: 10.1021/nl903730r | *Nano Lett.* **2010,** *10,* 645-651

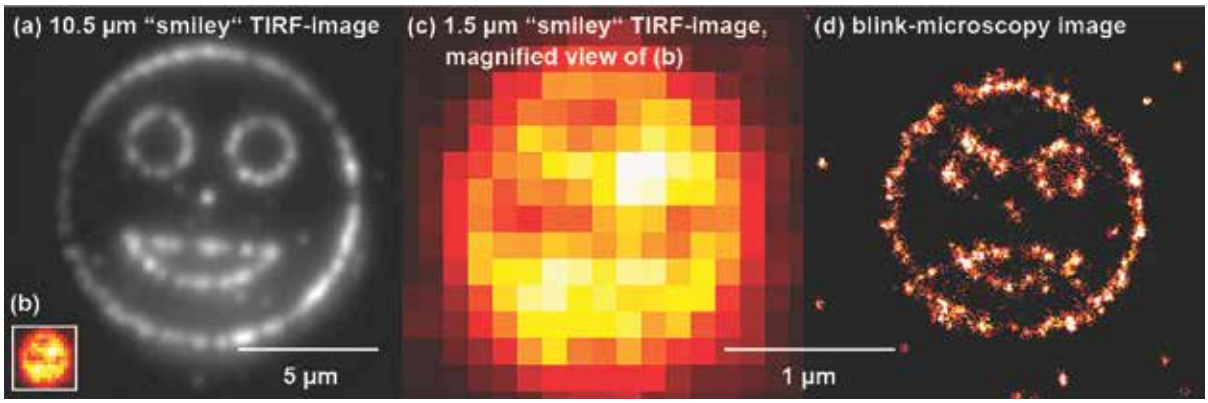

FIGURE 2. Images of patterns assembled by single-molecule cut-and-paste. (a) TIRF-image of a 10.5 μm diameter smiley (~650 transport-DNA labeled with the fluorophore Cy3; experiment conducted in PBS-buffer, 532 nm excitation with ~0.25 kW/cm^2) and (b) TIRF image of a 1.5 μm diameter smiley from another experiment as inset (~125 transported DNA labeled with the fluorophore ATTO655; experiment conducted in PBS-buffer, 50 μM AA as reductant, ambient oxygen as oxidant, 647 nm excitation with ~ 50 kW/cm^2). Scale bar for both panels (a,b) is 5 μm. (c,d) Magnified TIRF image and corresponding superresolution image of the smiley from inset panel (b) with 1.5 μm diameter; please note the smaller size of the scale bar of 1 μm corresponding to panels (c,d).

Blink-Microscopy. For example, line patterns were created to characterize the trade-off between spatial and temporal resolution of superresolution methods that separate the fluorophore emission of single emitters in time.

First, we assembled structures such as a smiley and visualized the patterns with fluorescence microscopy. Figure 2a shows an image of a smiley structure with a diameter of 10.5 μm. For this image an approximate number of 650 DNA-oligomers and attached Cy3-fluorophores were transported. All details of the structure, for example, eyes, nose, and mouth could be clearly resolved utilizing total-internal-reflection fluorescence (TIRF) microscopy.

In another experiment with the dye ATTO655 we reduced the size of the assembled smiley by a factor of ~7 down to 1.5 μm diameter, resulting in a structure with subwavelength size features. In contrast to the data in Figure 2a, no details of this smiley (Figure 2b, inset), except its circular structure, could be resolved (Figure 2b,c). Subdiffraction resolution images were subsequently recorded utilizing Blink-Microscopy. For recording these images, the oxazine dye ATTO655 was used in combination with 50 μM ascorbic acid (AA) in the presence of oxygen. Under these conditions, ATTO655 showed continuous blinking (see Figure 1d and ref 16) allowing a superresolution image to be obtained. Figure 2d clearly reveals all details of the smiley with eyes, nose, and mouth. A few gaps in the image are related to a significant fraction of inactive molecules among the transported fluorophores. In contrast to Cy3, we found that a fraction of ATTO655 fluorophores degraded during a drying step of the surface preparation procedure (see Supporting Information for details on sample preparation). The data presented in Figure 2 already demonstrates that Blink-Microscopy is a valuable tool for studying the nanomechanical assembly of SMCP on a length-scale below 200 nm.

Next, SMCP was utilized for a quantitative characterization of parameters that determine resolution for Blink-Microscopy and related approaches.[21,22] For isolated single immobilized ATTO655, that is, molecules which are not located in a distinct pattern (see points in Figures 2 and 3), OFF-times were determined to $\tau_{off} = 430$ ms, ON-times were ~2−3 ms with 800 ± 400 ON-counts under the applied buffer conditions (aerated PBS with 50 μM AA; for further details see Supporting Information). Those single molecules could be localized with a precision of 20 ± 4 nm, in accordance with theoretical expectations (a discussion of the experimentally observed versus theoretically expected resolution is found in the Supporting Information and ref 27).

When assembling line-structures with SMCP (Figure 3), we found an experimental width of a single line of 56 ± 16 nm. This value was derived from ~40 lines with 500 nm length, where each line consisted of several ATTO655 fluorophores assembled at 15 nm separation. The standard deviations were determined from Gaussian fits of a projection of the localization frequency at a single coordinate onto the *x*-axis, which results in histograms such as depicted in Figure 3c,j. This larger line width of 56 nm compared to the localization precision of single molecules of 20 nm is related to noise of the SMCP process. With a nominal tip diameter of ~20 nm and a flexible polymer handle that induces an uncertainty of ±10 nm,[13] we estimated the spatial accuracy of SMCP, which is directly related to the physical width of the assembled line to 40 nm. The SMCP-precision was caused by a denser functionalization of the cantilever compared to previous experiments.[13] Together with the optical localization precision of Blink-Microscopy of 20 nm, the expected measured line width by Blink-Microscopy was of the order of ~60 nm, a value that is in neat accordance with the experimentally determined width of a single line of 56 ± 16 nm.

DOI: 10.1021/nl903730r | *Nano Lett.* **2010,** *10,* 645-651

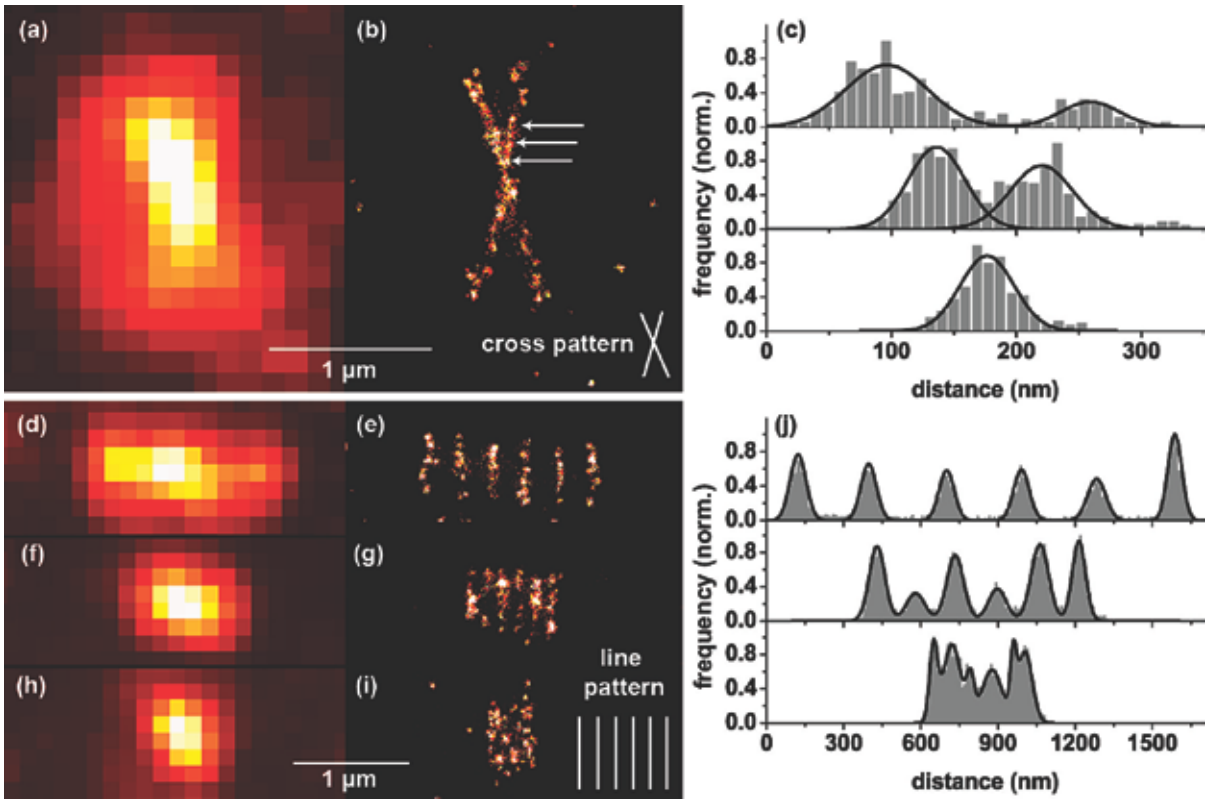

FIGURE 3. Examples of Blink-Microscopy images of subdiffraction patterns assembled by SMCP (PBS containing 50 μM AA as reductant, ambient oxygen served as oxidant). (a,b) TIRF and superresolution image of a cross pattern consisting of two lines (1.5 μm length) intersecting at an angle of 35°. The cross pattern consists of ~180 fluorophores. Panel (c) shows the corresponding histograms of single-molecule localizations at marked positions, at the positions indicated in panel (b). These histograms show that line distances of 160 nm (upper panel) and 80 nm (middle part) were clearly resolved, whereas in the range of the line-width (50 nm, lower part) the lines were no longer distinguishable. (d–i) Line grids consisting of a pattern of six parallel lines (0.5 μm length, representing ~150 active fluorophores) with decreasing spacing between the lines. Panels (d,e) show a TIRF and a superresolution image of a line grid with 300 nm spacing, (f,g) show data for 150 nm spacing, and (h,i) show data of a line grid with 75 nm spacing. Corresponding histograms of single-molecule localizations for the different superresolution images of the line grids are displayed in panel (j).

The combination of SMCP and Blink-Microscopy was then used for an actual calibration and characterization of (i) spatial resolution and (ii) resolvable fluorophore density. Therefore two different types of calibration structures were assembled with ATTO655 labeled DNA and subsequently imaged with superresolution microscopy to resolve the assembled structure. Figure 3 shows the TIRF (a) and corresponding superresolution image (b) of a "cross pattern" consisting of two lines with 1.5 μm length, intersecting at an angle of 35°. The superresolution image (Figure 3b) clearly reveals the fine-structure of the cross pattern that is not resolved in the TIRF-image (Figure 3a). The cross pattern was analyzed by taking horizontal slices of single-molecule localizations as shown in Figure 3c. Arrows in Figure 3b mark the different positions where histograms were taken. The depicted histograms were generated by a projection of the absolute number of single-molecule localizations of the respective pixel onto the horizontal axis. Histograms at the different positions reveal that a peak to peak distance of 160 nm (Figure 3c, upper panel) and 80 nm (Figure 3c, middle panel) between the lines was easily resolved. The histogram corresponding to the lowest arrow (Figure 3c, lower panel) in Figure 3b shows that in the range of the line-width of ~50–60 nm the two lines are no longer distinguishable. These data show that the achievable resolution when assembling and imaging line patterns is in the range of ~50–60 nm due to combined errors from SMCP and Blink-Microscopy.

The cross-pattern allows a qualitative estimate of the achievable spatial resolution of SMCP assembled lines. When several lines are close together the fluorophore density within one diffraction-limited area that is within 310 nm FWHM (full width at half-maximum) in our microscope increases. This leads to an increasing probability that two fluorophores emit simultaneously and deteriorate resolution. Blink-Microscopy offers an easy way to react to higher fluorophore density since the ON-counts and OFF-times are independently tunable through variation of the concentrations of reductant and oxidant, respectively.[16] At higher

DOI: 10.1021/nl903730r | *Nano Lett.* **2010,** *10,* 645-651

oxidant concentration, the OFF-times are shortened and the number of molecules that can be independently localized decreases. The advantage, however, is the fast recording time with fast blinking since more molecules could be localized within a shorter period of time. Vice versa, the OFF-times can be extended to react to the fluorophore density of the sample and the structural details to be resolved by decreasing the oxidant concentration. The τ_{off}/τ_{on}-ratio thereby is the central parameter that determines the resolvable fluorophore density. In order to quantify this trade-off of spatial and temporal resolution experimentally,[7,15] we assembled patterns consisting of six parallel lines with a variable spacing between them. The size of the grids was always greater than the size of the PSF, so that the grid-size is effectively infinite for an observation volume in the middle of the grid. The spacing between the lines was varied between 300 and 50 nm thereby increasing the fluorophore density. Subsequently, superresolution blink-images were recorded to check whether the respective line grid could be resolved at a given ratio of τ_{off}/τ_{on}. We defined a line grid resolved, if all the lines within the structure were clearly separated, i.e., six separate peaks with the appropriate spacing were observed in the histograms. Subsequently, we varied the OFF-times using different oxidant concentrations in order to experimentally study the trade-off between spatial and temporal resolution.

Figure 3 shows three line grids with a spacing of 300 nm (Figure 3d,e and associated histogram in the upper panel of Figure 3j), 150 nm (Figure 3f,g and associated histogram in the middle panel of Figure 3j) and 75 nm (Figure 3h,i and associated histogram in the lower panel of Figure 3j). With TIRF-microscopy, none of the grids was resolved as expected for the line-spacing and pixel-size of the TIRF-image of 137 nm. The superresolution images (Figure 3e,g,h) and the associated histograms (Figure 3j, 50 μM AA in the presence of oxygen, ratio of $\tau_{off}/\tau_{on} = 200$) reveal that the grids are resolved utilizing Blink-Microscopy; all histograms show six peaks at average distances of 292 ± 12 nm for the 300 nm line grid (Figure 3j, upper panel), 157 ± 7 nm for the 150 nm line grid (Figure 3j, middle panel), and 71 ± 15 nm for the 75 nm line grid (Figure 3j, lower panel).

Next, we quantified the fluorophore density for different line grids using the following approximation. In the case of aerated PBS with 50 μM AA and no 1,1′-dimethyl-4,4′-bipyridinium dichloride hydrate (methyl viologen, MV) present, the average number of localizations for a single-molecule over 8000 frames was 35 ± 16. A typical line grid, as shown in Figure 3, was characterized by 3000−4000 localizations over 8000 frames which translates into a maximal number of ∼150 active fluorophores per grid. Note that this approximation incorporates the fact that the spot-finding algorithm discards ∼25% of all localized events. This means that a single line with a length of 1 μm typically consists of ∼50 active fluorophores. Using this approximation, we estimated the fluorophore density in molecules per μm^2 for different line grids; a line grid with 300 nm spacing shows a density of ∼150 fluorophores/μm^2, a grid of 200 nm ∼250 fluorophores/μm^2, a grid of 150 nm spacing contains ∼300 fluorophores/μm^2, a grid of 100 nm spacing contains ∼500 fluorophores/μm^2, a grid of 75 nm spacing contains ∼650 fluorophores/μm^2, and finally a 50 nm grid contains 1000 fluorophores/μm^2.

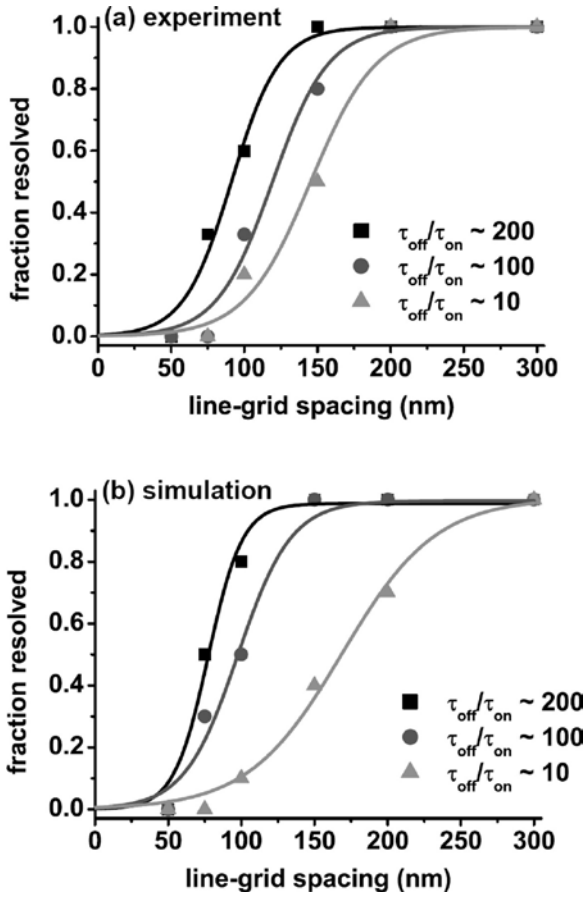

FIGURE 4. (a) Experimental values of the resolved line grid fraction for different ratios of τ_{off}/τ_{on}. The data were fitted with sigmoidal functions $y(x) = 1 - 1/(1 + e^{(x-a)/b})$ with a and b as free parameters. Further details about the statistics of the experiments and the determination of ON- and OFF-times can be found in the Supporting Information. (b) Similar results and associated fit functions of Monte Carlo-Simulations; for details, see Supporting Information.

To quantify the achievable number of resolved fluorophores per PSF-width in terms of "resolvable line grid fraction", which is the number of resolved line grids divided by the total number of measured line grids, similar experiments as depicted in Figure 3 were repeated several times. On average four line grids per spacing were analyzed (see Table S1 in Supporting Information for details). Thereby, care was taken to compare only those line grids bearing a similar number of active fluorophores. Figure 4 shows the

DOI: 10.1021/nl903730r | Nano Lett. 2010, 10, 645-651

fraction of resolved line grids for different line-spacings together with sigmoidal fits for different values of τ_{off}/τ_{on}. The reversal point indicates the line grid spacing where 50% of the line grids were resolved for a certain τ_{off}/τ_{on}-ratio.

Starting with a ratio of τ_{off}/τ_{on} ~200 (Figure 4, black; concentration of the oxidant MV = 0 μM) shows that down to a line grid spacing of 150 nm (~300 fluorophores/μm^2) all grids were resolved while significant fractions of line grids with 100 and 75 nm spacing, corresponding to ~500−650 fluorophores/μm^2, are still resolved. Grids with 50 nm spacing and a fluorophore density of 1000 fluorophores/μm^2 cannot be resolved. A sigmoidal fit reveals that a fraction of 50% is resolved at a grid-size of 91 ± 3 nm (Figure 4, black) corresponding to an estimated fluorophore density of ~530 fluorophores/μm^2. Since this value is close to the measured line-width discussed above, this resolution and also the density of fluorophores that can be resolved are mainly influenced by other parameters than the τ_{off}/τ_{on}-ratio of ~200. The resolution in our experiments was shown to be spatially limited to ~50−60 nm, which makes it impossible for us to resolve structures with 50 nm grid-size even with infinite τ_{off}/τ_{on}-ratio.

Subsequently, the same experiments were conducted at different concentrations of the oxidant MV, that is, at different τ_{off}/τ_{on}-ratios. Reducing this ratio to τ_{off}/τ_{on} ~100 by adding 10 μM MV to the buffer significantly alters the observed behavior (Figure 4, red). While the acquisition time can be reduced by the factor the ON-OFF duty cycle is reduced, only smaller fractions of the 150, 100, and 75 nm line grids were resolved and the reversal point is found at 119 ± 5 nm corresponding to an estimate of ~400 fluorophores/μm^2. This change is directly related to the lower number of fluorophores that could be colocalized at shorter OFF-times and experimentally demonstrates the trade-off of a lower spatial resolution at increased time resolution.

At a τ_{off}/τ_{on}-ratio of ~10, that is, a concentration of MV = 250 μM, the fraction of resolved grids decreases and shifts the turning point to 145 ± 6 nm corresponding to ~300 fluorophores/μm^2 in accordance with the proposed relation.

It is not trivial to access and quantify the parameters that describe this resolution change. This is because the spot finding and localization algorithm in the analysis software uses intensity thresholds, an area size- as well as a circularity-criterion for the selected spots.[7] Accordingly, the algorithm was often able to detect and discard spots when two molecules were simultaneously fluorescent within a diffraction limited area. We carried out Monte Carlo simulations to emulate the measurements and to be able to compare our measurements with expectations. Therefore 8000 video-frames of blinking dyes, which exhibit comparable emission properties as those recorded experimentally, were generated. In these simulations, molecules were placed in analogous line patterns with the SMCP precisions determined above (for details see Supporting Information). The simulated data sets were evaluated utilizing the same analyzing software as for the experimental data and yielded graphs and fit functions depicted in Figure 4b. The theoretical values where 50% of the line grids could be resolved were derived from sigmoidal fits, 77 ± 4 nm for τ_{off}/τ_{on} ~200, 98 ± 5 nm for τ_{off}/τ_{on} ~100, and 170 ± 10 nm for τ_{off}/τ_{on} ~10. These values show a slightly larger spread than the experimental values. They, however, support the idea that the resolution is limited by the physical line widths rather than the τ_{off}/τ_{on}-ratio for the smallest grids. The simulations further demonstrate that after a thorough photophysical characterization of the probes used for superresolution microscopy the imaging speed can be adapted to the desired resolution and thus be optimized to the specific problem.

In conclusion, we presented a combination of a recently established method for the bottom-up assembly of artificial structures (SMCP) and superresolution Blink-Microscopy. Superresolution microscopy served to image subdiffraction features in smiley-, cross-, and line grid-patterns created by SMCP that are difficult to characterize by other methods. Subsequently, we used patterns created by SMCP to experimentally demonstrate the trade-off of acquisition speed and spatial resolution of superresolution techniques that rely on the subsequent localization of single molecules. The adjustability of the blinking in Blink-Microscopy allowed adapting the photophysical parameters to achieve the desired spatial resolution at optimized acquisition rate. Accordingly, SMCP one-by-one assembled patterns turn out to be valuable structures for the characterization and calibration of superresolution microscopes. Simulations of the line grid structures complement the analysis and will be helpful to optimize algorithms used for single-molecule identification and localization.

Finally, this work shows the great potential of combining the complementary techniques of single-molecule assembly and superresolution microscopy. It is envisioned to create biochemical networks and enzyme cascades via SMCP whose interactions and functioning will then be accessible using superresolution fluorescence microscopy.

Acknowledgment. The authors thank Dominik Ho for stimulating discussions. This work was supported by the DFG (Inst 86/1051-1), the Volkswagen Foundation, the Biophotonics III Program of the BMBF/VDI (grant 13N9234), the Nanosystems Initiative Munich, and the Elitenetzwerk Bayern.

Supporting Information Available. Details of material and methods, sample preparation, single-molecule cut-and-paste, TIRF-microscopy and superresolution Blink-Microscopy, confocal microscopy; additional results from confocal microscopy and statistics of the resolved line grid fraction. This material is available free of charge via the Internet at http://pubs.acs.org.

REFERENCES AND NOTES

(1) Yildiz, A.; Forkey, J. N.; McKinney, S. A.; Ha, T.; Goldman, Y. E.; Selvin, P. R. *Science* **2003**, *300* (5628), 2061–2065.
(2) Hell, S. W. *Science* **2007**, *316* (5828), 1153–1158.

DOI: 10.1021/nl903730r | *Nano Lett.* **2010,** *10,* 645-651

(3) Betzig, E.; Patterson, G. H.; Sougrat, R.; Lindwasser, O. W.; Olenych, S.; Bonifacino, J. S.; Davidson, M. W.; Lippincott-Schwartz, J.; Hess, H. F. *Science* **2006**, *313* (5793), 1642–1645.
(4) Rust, M. J.; Bates, M.; Zhuang, X. *Nat. Methods* **2006**, *3* (10), 793–5.
(5) Hess, S. T.; Girirajan, T. P.; Mason, M. D. *Biophys. J.* **2006**, *91* (11), 4258–72.
(6) Heilemann, M.; van de Linde, S.; Schuttpelz, M.; Kasper, R.; Seefeldt, B.; Mukherjee, A.; Tinnefeld, P.; Sauer, M. *Angew. Chem., Int. Ed.* **2008**, *47* (33), 6172–6176.
(7) Steinhauer, C.; Forthmann, C.; Vogelsang, J.; Tinnefeld, P. *J. Am. Chem. Soc.* **2008**, *130* (50), 16840–16841.
(8) Rothemund, P. W. *Nature* **2006**, *440* (7082), 297–302.
(9) Steinhauer, C.; Jungmann, R.; Sobey, T. L.; Simmel, F. C.; Tinnefeld, P. *Angew. Chem., Int. Ed.* **2009**, *48* (47), 8870–8873.
(10) Piner, R. D.; Zhu, J.; Xu, F.; Hong, S.; Mirkin, C. A. *Science* **1999**, *283* (5402), 661–3.
(11) Rodolfa, K. T.; Bruckbauer, A.; Zhou, D. J.; Korchev, Y. E.; Klenerman, D. *Angew. Chem., Int. Ed.* **2005**, *44* (42), 6854–6859.
(12) Kufer, S. K.; Puchner, E. M.; Gumpp, H.; Liedl, T.; Gaub, H. E. *Science* **2008**, *319* (5863), 594–596.
(13) Kufer, S. K.; Strackharn, M.; Stahl, S. W.; Gumpp, H.; Puchner, E. M.; Gaub, H. E. *Nat. Nanotechnol.* **2009**, *4* (1), 45–9.
(14) Puchner, E. M.; Kufer, S. K.; Strackharn, M.; Stahl, S. W.; Gaub, H. E. *Nano Lett.* **2008**, *8* (11), 3692–5.
(15) Shroff, H.; Galbraith, C. G.; Galbraith, J. A.; Betzig, E. *Nat. Methods* **2008**, *5* (5), 417–23.
(16) Vogelsang, J.; Cordes, T.; Forthmann, C.; Steinhauer, C.; Tinnefeld, P. *Proc. Natl. Acad. Sci. U.S.A.* **2009**, *106* (20), 8107–12.
(17) Hell, S. W. *Nat. Methods* **2009**, *6* (1), 24–32.
(18) Klar, T. A.; Jakobs, S.; Dyba, M.; Egner, A.; Hell, S. W. *Proc. Natl. Acad. Sci. U.S.A.* **2000**, *97* (15), 8206–8210.
(19) Sharonov, A.; Hochstrasser, R. M. *Proc. Natl. Acad. Sci. U.S.A.* **2006**, *103* (50), 18911–18916.
(20) Lemmer, P.; Gunkel, M.; Weiland, Y.; Muller, P.; Baddeley, D.; Kaufmann, R.; Urich, A.; Eipel, H.; Amberger, R.; Hausmann, M.; Cremer, C. *J. Microsc.* **2009**, *235* (2), 163–71.
(21) Folling, J.; Bossi, M.; Bock, H.; Medda, R.; Wurm, C. A.; Hein, B.; Jakobs, S.; Eggeling, C.; Hell, S. W. *Nat. Methods* **2008**, *5* (11), 943–5.
(22) van de Linde, S.; Kasper, R.; Heilemann, M.; Sauer, M. *Appl. Phys. B* **2008**, *93* (4), 725–731.
(23) Flors, C.; Ravarani, C. N.; Dryden, D. T. *ChemPhysChem* **2009**, *10* (13), 2201−2204.
(24) Vogelsang, J.; Kasper, R.; Steinhauer, C.; Person, B.; Heilemann, M.; Sauer, M.; Tinnefeld, P. *Angew. Chem. Int. Ed.* **2008**, *47*, 5465–5469.
(25) Thompson, R. E.; Larson, D. R.; Webb, W. W. *Biophys. J.* **2002**, *82* (5), 2775–2783.
(26) Egner, A.; Geisler, C.; von Middendorff, C.; Bock, H.; Wenzel, D.; Medda, R.; Andresen, M.; Stiel, A. C.; Jakobs, S.; Eggeling, C.; Schonle, A.; Hell, S. W. *Biophys. J.* **2007**, *93* (9), 3285–90.
(27) Bossi, M.; Folling, J.; Belov, V. N.; Boyarskiy, V. P.; Medda, R.; Egner, A.; Eggeling, C.; Schonle, A.; Hell, S. W. *Nano Lett.* **2008**, *8* (8), 2463−2468.

DOI: 10.1021/nl903730r | *Nano Lett.* **2010,** *10,* 645-651

Supporting information for the manuscript

Resolving single-molecule assembled patterns with superresolution blink-microscopy

*Thorben Cordes,[1] Mathias Strackharn,[1] Stefan W. Stahl, Wolfram Summerer, Christian Steinhauer, Carsten Forthmann, Elias M. Puchner, Jan Vogelsang, Hermann E. Gaub, and Philip Tinnefeld**

Applied Physics – Biophysics & Center for NanoScience, Ludwig-Maximilians-Universität, Amalienstr. 54, D-80799 München, Germany

[1]These authors contributed equally to this work.

*Corresponding author, philip.tinnefeld@lmu.de; fax: +49 89 2180 2005

1. Material and methods

1.1. Single-molecule cut-and-paste (SMCP)

Sample-preparation: Depot and target area were prepared on circular cover slides, all details of the procedure can be found in refs. [1-3]. The slides were amino silanized and functionalized with N-hydroxy-succinimide-ester (NHS)-PEG-maleimide (M = 5000 g/mol, Rapp Polymere, Tübingen, Germany 50 mM). Subsequently, a PDMS flow chamber with two channels, connected to a peristaltic pump, was mounted on the cover slip. One channel (depot area) was rinsed for 1 h with a 10 mM solution of depot anchor oligomer while the other channel (target area) was rinsed with a 10 mM

solution of the target oligomer. Subsequently, the depot area was additionally rinsed with a 1 µM solution of transport oligomer dissolved in phosphate buffered saline (PBS) (depot oligomer: HS-5'-TTTTTTTTTAAGTAGCTATTCGAACTATAGCTTAAGGCAGTCAA-3'; transport oligomer: 5'-TTTTTGACGTCCTTAAGCTATAGTTCGAATAGCTACTTTT*TTTTTTCATCGATAAGCTTGAT ATCGAATTCCTGCAGTTTTT-3' with T* = T-ATTO655; target oligomer: 5'-AGTAGCTATTCGAACTATAGCTTAAGGACGTCTTTTTTTTTT-3'-SH). All oligomers were of HPLC grade and were synthesized by IBA (IBA, Göttingen, Germany). Thiol-modified oligomers were reduced with TCEP before coupling to PEG to generate free mercaptans. For usage in the SCMP experiment the cover slide was rinsed with PBS buffer and placed in a custom-made sample-holder.

The SMCP-setup: All SMCP experiments were performed on a custom-built AFM at room temperature in PBS buffer. Cantilevers (Veeco MSCT and Olympus BL-AC40) were covalently functionalized with NHS-PEG-maleimide (M = 5000 g/mol) and a DNA oligomer (HS-5'-TTTTTTTTTTCTGCAGGAATTCGATATCAA-3') that is able to hybridize with the transport oligomer. Spring constants of the cantilever were determined in solution by the equipartition theorem [4], with typical values of 13 pN/nm for the MSCT-C and 70 pN/nm for the BL-AC40. To transport DNA molecules, the tip and the sample were controlled in closed loop operation with a MFP-3D controller (Asylum Research, Santa Barbara, CA, USA). Software control of the SMCP process was performed in custom-made Igor Pro 5.03 (Wave Metrics).

For experiments with ATTO655 attached to the transport DNA, SMCP was performed with a cantilever with high functionalization density to transport 2-5 strands at a time. As only a fraction of 10-20% of the transported DNA-strands showed detectable emission, this was necessary to achieve a sufficient number of active fluorophores in the assembled pattern. The high number of in-active fluorophores was most likely caused by the drying process of the cover-slide within the preparation procedure and no such degradation was noticed for Cy3.

TIRF-imaging with Cy3: Imaging with transported Cy3 dyes was performed under TIRF excitation at 532 nm with at 75 mW DPSS laser (Crystalaser, Reno, USA) through an oil immersion objective (100×, NA 1.49, CFI Apochromat TIRF, Nikon, Japan). The laser was focused on the back-focal plane of the objective, the fluorescence light was filtered by a Brightline 582/75 and imaged onto a back-illuminated EMCCD camera (128x128 pixel, Andor Ixon DV-860). More details concerning all different aspects of SMCP are found in refs. [1-3].

1.2. TIRF-Imaging with ATTO655 and superresolution blink-microscopy

Fluorescence imaging was conducted on an inverted microscope (Olympus IX-71) in objective type total-internal-reflection fluorescence (TIRF) configuration. Images were collected with a back-illuminated EMCCD camera (128x128 pixel, Andor Ixon DU-860-CS0). Excitation was at 650 nm with 300 mW (single mode diode laser XTL, Toptica) and filtered by a clean-up filter (Brightline HC 650/13, AHF Analysentechnik); the beam was coupled into an oil-immersion objective (UPlanSApo 100×, NA 1.40, Olympus) using a dual-band beamsplitter (z532/658rpc, AHF, Analysentechnik). The illumination area of 600 μm^2 was approximately twice the size of the observation area of ~300 μm^2. An image magnification of ~160 fold – corresponding to a pixel size of 137 nm – was achieved by additional lenses. The fluorescent sample light was spectrally filtered by an emission filter (HQ 700/75 M, AHF Analysentechnik).

Blink-microscopy images were collected on the same setup under the following experimental conditions and without oxygen removal: 50 µM ascorbic acid (AA) were added to phosphate-buffered saline (PBS) with variable amounts, i.e. 0-250 µM, of N,N-methylviologen (MV). Under these conditions approximately N_{on} = 800 ± 400 counts were detected from a single ATTO655 molecule per on-time in the wide-field setup. According to ref. [5] the localization precision is given by ~FWHM/$(N_{on}/2)^{1/2}$ with FWHM ~310 ± 18 nm for our setup. We excluded noise arising from

background light and camera readout which suggests a theoretical localization precision of 16 nm.[6] The experimental value of 20 ± 4 nm is slightly higher – a fact that may be explained by polarization effects [7] and the internal labeling of ATTO655 to DNA. The dye molecule was separated from the PEG-linker on the surface by ~35 double-stranded base-pairs. The typical laser power for imaging was 300 mW (~50 kW/cm^2) and 4000-16000 frames were recorded at frames rates of 250-1000 Hz. The laser power was adjusted for ON-times corresponding to the integration time of the camera of ~1-4 ms.

The image reconstruction used for superresolution imaging was conducted with custom-made software as described in refs. [8]. Briefly, the first frames of the movie, typically frames 20-150, were discarded as most of the molecules were in the active state after starting laser excitation. Subsequently, the spot-finding algorithm analyses the movie frame by frame involving a lower and upper threshold. Each intensity pattern in the respective frame is then compared to its environment (commonly 7 × 7 pixels): In the case a certain contrast value (typically 2) is reached, the spot was considered for further analysis. To exclude events with two molecules being active within one diffraction limited area and to remove events when the two-dimensional Gaussian did not converge the indentified spots needed to fulfill a circularity criterion – commonly, ~25% of all events were discarded. Two-dimensional Gaussian fitting yields the position of the emitting molecule – a histogram of all molecule positions yields the superresolution image as shown in Figures 1-3 (main text).

1.3. Confocal microscopy

Fluorescent transients from single immobilized ATTO655 molecules were recorded in a home-built confocal scanning microscope. ATTO655 molecules were immobilized according to published procedures utilizing similar procedures as for SMCP-sample preparation.[1-2] Excitation at 640 nm (spectral width ~2 nm) was based on a supercontinuum laser source (SuperK Extreme, Koheras, Denmark) in combination with acousto-optical tunable filters (AOT-Fnc-VIS, AA Optoelectronic). The laser beam was coupled into an oil-immersion objective (60×, NA 1.35, UPLSAPO60X0, Olympus)

after passing a single-mode fiber, resulting in an average excitation intensity of 4 kW/cm^2. The emitted fluorescence was collected by the same objective and spatially filtered by a 50 µm pinhole. After a bandpass filter (HQ 700/75 M, AHF Analysentechnik) fluorescence was detected on an avalanche photodiode (APD, SPCM-AQR-14; Perkin Elmer).

The photophysical properties of the transport DNA from SMCP were investigated according to ref. [9]. For this purpose a constant amount of AA (50 µM) and varying amounts of MV (0-250 µM) were added to PBS-buffer. At each MV concentration ~40 single-molecule transients were recorded. Subsequently, autocorrelation analysis was employed to extract ON- and OFF-times from each single-molecule. A detailed description of the data-evaluation is found in ref. [9].

2. Results

2.1. Blinking properties of transport DNA: ATTO655

As shown in refs. [9-11] oxazine dyes show a strong dependence of their fluorescent properties on their environment (linker-structure, pH-value, oxidant- and reducer-concentration). For a determination of specific ON- and OFF-times of ATTO655 bound to the transport DNA – needed for a quantitative estimation of the resolution enhancement (see Figure 4, main text) – we recorded the blinking kinetics as shown in Figure S1. The experiments were conducted on a confocal microscope as described above. Autocorrelation analysis revealed that the addition of 50 µM AA to aerated PBS buffer leads to frequent blinking of ATTO655 with an OFF-time duration of τ_{off} = (430 ± 90) ms. As expected, the ON-counts remain constant within experimental error (data not shown) while τ_{off} reduces with increasing MV concentration (Figure S1). Further relevant OFF-times for superresolution measurements are τ_{off} = (180 ± 35) ms at 10 µM MV and τ_{off} = (14 ± 10) ms at 250 µM MV.

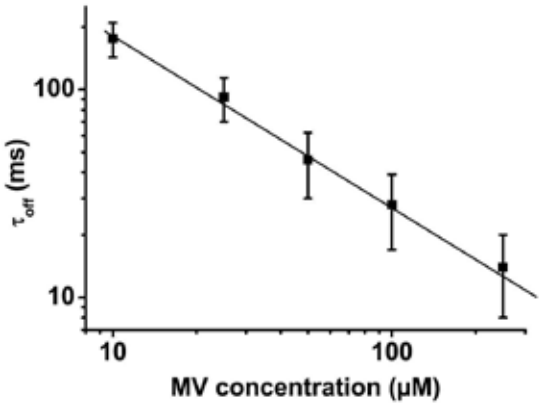

Figure S1: Double-logarithmic representation of the OFF-times of the investigated transport-DNA labeled with ATTO655 measured on a confocal microscope according to ref. [9]. For this purpose single transport DNA-strands were immobilized as described in the SCMP-section. The solid line is drawn to guide the eye.

2.2. Line grid analysis and resolved line grid fraction

In the main text an overview of the resolved line grid fraction in form of Figure 4 is given. Here, the dependence between the τ_{off}/τ_{on}-ratio and the achievable resolution, i.e., the actual number of fluorophores that can be resolved within the size of one PSF – in terms of resolved line grid fraction – is presented. Table S1 summarizes the fractions of resolved grids with respect to the numbers of measured line grids (see also Figure 4 in the main text).

Table S1: Resolved line grid fraction: actual number of resolved line grids (first number) and number of measured line grids (second number) together with the resulting resolved fraction (third number). The actual fraction is also displayed in Figure 4, main text. The values are given for a constant concentration of AA (50 µM) and varying concentrations of the oxidant MV ([MV] = 0-250 µM) for different line grid spacings (50-300 nm).

Line grid spacing	[MV] = 0 µM	[MV] = 10 µM	[MV] = 250 µM
300 nm	4 of 4; 1.0	3 of 3; 1.0	4 of 4; 1.0
200 nm	4 of 4, 1.0	3 of 3; 1.0	3 of 3; 1.0
150 nm	5 of 5; 1.0	4 of 5; 0.8	2 of 4; 0.5
100 nm	4 of 7; 0.6	3 of 6; 0.33	1 of 5; 0.2
75 nm	2 of 6; 0.33	0 of 5; 0.0	0 of 3; 0.0
50 nm	0 of 3; 0.0	0 of 3; 0.0	not determined

2.3. Monte Carlo Simulations of line grid resolved by blink-microscopy

For a detailed comparison of the experimental values from Table S1 with theory, the line grids assembled by SMCP were simulated by Monte Carlo Simulations. A description of the simulation procedure is given in ref. [8]. The simulations generated videos of 8000 frames with blinking dyes that exhibit comparable emission properties as those recorded experimentally with the EMCCD camera: ON-times were fixed to 2.5 ms with 800 ON-counts. The lines also included the experimentally determined error for the line-width and consisted of a comparable number of active fluorophores (~150). The generated videos were analyzed with the same custom-made software as described in the experimental section.

Table S2: Theoretical values of the resolved line grid fraction: actual number of resolved line grids (first number) and number of measured line grids (second number) together with the resulting resolved fraction (third number). The actual fraction is also displayed in Figure 4, main text. The values are given for a constant ON-time of 2.5 ms and varying off-time durations for different line grid spacings (50-300 nm).

Line grid spacing	τ_{off} = 400 ms	τ_{off} = 200 ms	τ_{off} = 20 ms
300 nm	5 of 5; 1.0	5 of 5; 1.0	5 of 5; 1.0
200 nm	5 of 5, 1.0	5 of 5; 1.0	7 of 10; 0.7
150 nm	5 of 5; 1.0	5 of 5; 1.0	4 of 10; 0.4
100 nm	8 of 10; 0.8	5 of 10; 0.5	1 of 10; 0.1
75 nm	5 of 10; 0.5	3 of 10; 0.3	0 of 5; 0.0
50 nm	0 of 5; 0.0	0 of 5; 0.0	0 of 5; 0.0

3. References:

1. Kufer, S.K., et al., *Single-molecule cut-and-paste surface assembly.* Science, 2008. 319(5863): p. 594-6.
2. Kufer, S.K., et al., *Optically monitoring the mechanical assembly of single molecules.* Nat Nanotechnol, 2009. 4(1): p. 45-9.
3. Puchner, E.M., et al., *Nanoparticle self-assembly on a DNA-scaffold written by single-molecule cut-and-paste.* Nano Lett, 2008. 8(11): p. 3692-5.
4. Butt, H.J. and M. Jaschke, *Calculation of thermal noise in atomic force microscopy.* Nanotechnology, 1995. 6: p. 1-7.
5. Bossi, M., et al., *Multicolor Far-Field Fluorescence Nanoscopy through Isolated Detection of Distinct Molecular Species.* Nano Letters, 2008. 8(8): p. 2463-8.
6. Thompson, R.E., D.R. Larson, and W.W. Webb, *Precise nanometer localization analysis for individual fluorescent probes.* Biophys J, 2002. 82(5): p. 2775-83.
7. Enderlein, J., E. Toprak, and P.R. Selvin, *Polarization effect on position accuracy of fluorophore localization.* Opt Express, 2006. 14(18): p. 8111-20.
8. Steinhauer, C., et al., *Superresolution microscopy on the basis of engineered dark states.* J Am

Chem Soc, 2008. 130(50): p. 16840-1.
9. Vogelsang, J., et al., *Controlling the fluorescence of ordinary oxazine dyes for single-molecule switching and superresolution microscopy.* Proc Natl Acad Sci U S A, 2009. 106(20): p. 8107-12.
10. Vogelsang, J., T. Cordes, and P. Tinnefeld, *Single-molecule photophysics of oxazines on DNA and its application in a FRET switch.* Photochem Photobiol Sci, 2009. 8(4): p. 486-96.
11. Vogelsang, J., et al., *A reducing and oxidizing system minimizes photobleaching and blinking of fluorescent dyes.* Angew Chem Int Ed Engl, 2008. 47(29): p. 5465-9.

Publikation 5

Peptide-Antibody Complex as Handle for Single-Molecule Cut & Paste.

Strackharn, M.; Stahl, S. W.; Severin, P. M.; Nicolaus, T.; Gaub, H. E.; Chemphyschem 2011,

CHEMPHYSCHEM

DOI: 10.1002/cphc.201100765

Peptide–Antibody Complex as Handle for Single-Molecule Cut & Paste

Mathias Strackharn,[a] Stefan W. Stahl,[b] Philip M. D. Severin,[a] Thomas Nicolaus,[a] and Hermann E. Gaub*[a]

Feynman is frequently quoted for having foreseen that individual atoms may be arranged one-by-one to form functional assemblies.[1] The seminal work by Don Eigler and colleagues[2,3] convincingly proved the validity of these concepts: functional assemblies of atoms forming quantum corrals showed emergent novel properties. In the life sciences, Hans Kuhn realized rather early that for many multistep biological reactions, not only the sequence but also the arrangement of the individual enzymes plays a crucial role. He envisaged that in order to investigate their interaction, novel approaches would be needed: he wished to have "…molecular pliers to pick and place individual enzymes to create functional assemblies with designed properties."[4] The application of bottom-up strategies to assemble biomolecular complexes, however, turned out to be rather challenging. A quite vivid dispute was fought in a series of papers between Smalley and Drexler on where these difficulties arise from and whether fundamental limitations prevent a molecule for molecule assembly of biomolecules in electrolyte ambient and at physiologic temperatures.[5] With the development of single-molecule cut-and-paste (SMC&P) we overcame these difficulties and provided a platform technology for the assembly of biomolecules at surfaces.[6] It combines the Å-positioning precision of atomic force microscopy (AFM)[7,8] with the selectivity of DNA hybridization to pick individual molecules from a depot chip and to arrange them on a target site by pasting the molecules one-by-one.[9] The advanced methods of single-molecule fluorescence detection[10–14] allowed us to localize the pasted molecules with nanometer accuracy and to show that the deposition accuracy is presently only limited by the length of the spacers used to couple the DNA handles and anchors to tip and construction site, respectively.[15]

In the various SMC&P implementations realized to date, the system of hierarchical binding forces was built from DNA duplexes of suitable geometry and sequence. Since one of the major goals, which spurs the development of the SMC&P technology, is the ability to arrange proteins, for example, in enzymatic networks of predefined composition and proximity, molecular anchors and handles should ultimately be of such a kind that they can be co-expressed with the proteins, for example, as tags on a protein chip. As a first step in this direction, we chose in this Communication a peptide–antibody complex to replace the DNA-based handle complex in the conventional SMC&P design. This single-chain antibody, which is part of a larger family, was selected by the Plückthun group to recognize a 12 aa long segment of a polypeptide chain with picomolar affinity.[16] In previous studies we had investigated by single-molecule force spectroscopy and molecular dynamics (MD) simulations several different peptides and antibodies and investigated the influence of the attachment site on the unbinding mechanisms.[17,18] We could confirm that the antibody (when covalently attached at the C-terminal end) stays intact when the peptide is pulled out of the binding pocket. Herein, we used this antibody immobilized at the AFM cantilever tip to pick up a fluorescently labeled transfer DNA–peptide chimera via its peptide tag and paste it on the target site of the chip.

Using a microspotter, we deposited microdroplets of a DNA solution onto a pretreated glass surface resulting in approximately 50 μm-sized spots with a distance of 70 μm (see Supporting Information, Figure 1). The ssDNA was allowed to covalently bind to the surface via PEG spacers. One drop contained ssDNA with a reactive 5′ end. The resulting spot later on forms the depot. The other drop contained DNA with a reactive 3′ end and the resulting spot forms the target. The depot area was then loaded with a complementary ssDNA strand, which was extended at the 3′ end by a 13-amino-acid-long handle peptide and labeled at the 5′ end with an atto647N fluorophore. For simplicity, this construct is called transfer strand. Single-chain antibodies were covalently attached via PEG spacers to the AFM cantilever tip (see Figure 1a for a cartoon of the SMC&P process).

To pick up an individual DNA strand, the AFM tip was lowered at the depot area, allowing the antibody at the tip to bind to the peptide at the end of the DNA strand to be transferred. Upon retract, typically the force gradually increased and finally dropped as shown in Figure 1b, where the force is plotted as a function of the distance. We chose the functionalization density of the tip and the surface such that typically only in every second attempt we found this characteristic force curve, indicating that exactly one DNA strand was picked up. In the majority of the other 50% of the attempts we found no measurable force upon retract, indicating that no molecule was picked up. In these cases, we repeated the pick-up cycle. Only in very rare cases (<2%) did we find higher values for the unbinding force, indicating that more than one molecule was picked up.

[a] M. Strackharn, P. M. D. Severin, T. Nicolaus, Prof. Dr. H. E. Gaub
Center for Nanoscience and Department of Physics
University of Munich, Amalienstrasse 54
80799 München (Germany)
Fax: (+49) 89-2180-2050
E-mail: gaub@lmu.de

[b] S. W. Stahl
Center for Integrated Protein Science (CIPSM)
Center for Nanoscience and Department of Physics
University of Munich, Amalienstrasse 54
80799 München (Germany)

Supporting information for this article is available on the WWW under http://dx.doi.org/10.1002/cphc.201100765.

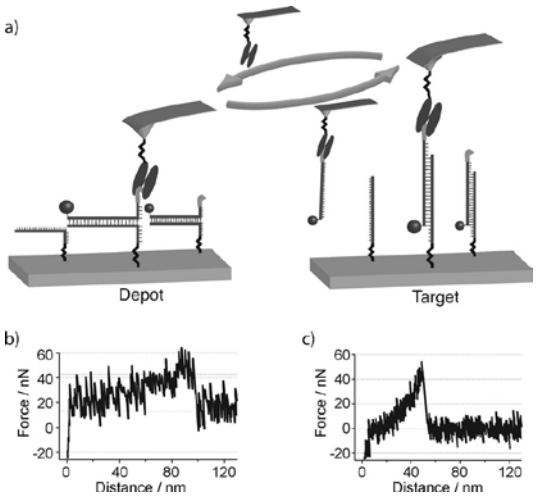

Figure 1. a) Schematic representation of a typical SMC&P cycle. A single-chain antibody fragment is covalently bound to the cantilever tip. When lowered to the depot area surface, the antibody binds to a peptide at the end of a DNA strand, which is attached to the surface via 40 bp in zipper mode. When the tip is pulled back, the basepairs open up one by one. The transfer construct remains attached to the cantilever and may be transferred to the target area. Here, the cantilever is lowered again such that the DNA part of the construct binds to the DNA target anchor. When the cantilever is retracted, this time the DNA bases are loaded in shear geometry and the antibody–peptide bond yields. The transfer construct remains in the target area and the cantilever can be used for the next transfer cycle again. b,c) Force-distance graphs of typical rupture events in the depot (b) and target (c) areas.

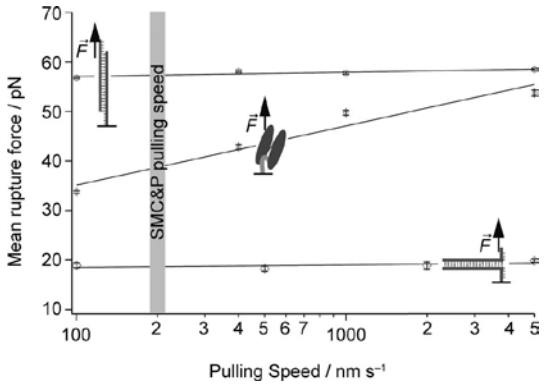

Figure 2. Dependency of the mean rupture force on the pulling speed. The mean rupture force for opening the 40 bp DNA in shear geometry is nearly 60 pN. The mean rupture force of the peptide–antibody complex is significantly lower than that of the DNA in shear geometry and shows a logarithmic dependence on the loading rate. The 40 bp DNA in unzip geometry opens at a mean rupture force of around 20 pN. Error bars depict fitting errors from fitting the force distributions. Highlighted is the pulling speed chosen for the deposition process.

The AFM tip was now moved to a chosen position in the target area and gradually lowered, allowing the transfer strand to hybridize to the target DNA. Upon retract again, the force-versus-distance curve was recorded. A typical example is given in Figure 1c. As can be seen, the force peaks at a much higher value, typically at 40 pN. Since this value is much lower than the force required to break the DNA shear bond, we conclude with a high certainty that the transfer DNA was deposited in the target area. Details of the probabilities for the rupture of bonds in series are given elsewhere.[19]

To corroborate that the force required to unzip the anchor duplex is lower than the binding force of the peptide–antibody complex and that the latter is lower than the force required to unbind the DNA duplex in shear geometry we investigated the bond strength of the three complexes in a separate series of experiments. Since unbinding forces depend in a first-order approximation given by the Bell–Evans model on the logarithm of the force loading rate,[20] we varied the latter by one and a half orders of magnitude. The result is depicted in Figure 2. For the lowest curve, the unbinding force of the depot–transfer duplex was measured under conditions where both were covalently attached to tip and sample surface via PEG spacers. Note that the depot strand was attached at its 5′ end and the transfer strand was attached at the 3′ end, mimicking the geometry during pickup. For the red curve, the peptide was attached to the sample surface, allowing the antibody, which was covalently attached to the tip, to bind the peptide in exactly the same geometry as during pick up. As can be seen, both lines differ drastically in their slopes, but more important for the issues discussed here, the force required to unzip the two DNA strands is significantly lower than that required to break the peptide–antibody bond for the entire range of pulling speeds. Since the curve of the antibody–peptide complex lies significantly below the curve recorded for the DNA duplex in shear geometry (note that the target strand was now attached with the 3′ end to the surface), it is predominantly the peptide–antibody complex that ruptures in the deposition process. From this graph we chose the optimum pulling speed window around 200 nm sec^{-1} for the SMC&P experiments described below.

In parallel to the SMC&P experiments, we followed the deposition process of the individual molecules microscopically in total internal fluorescence excitation. Details of the device are given elsewhere,[21] but it is important to note that the custom-built combined AFM–TIRF microscope was optimized for vibrational stability, which is essential to avoid the coupling of mechanical noise into the AFM via the immersion fluid required for high NA optical microscopy. Figure 3a shows a micrograph taken at the beginning of the deposition process in the target region. In Figure 3b the left image shows the scattered light from the tip and the emission of the fluorophore. The second image depicts the same spot after the tip has left the evanescent zone, leaving only the deposited fluorophore visible (a movie of this process is provided in the Supporting Information). With standard techniques, the position of this fluorophore was then determined with an accuracy of 1.4 nm.

After the deposition of the transfer strand in the target area, the tip is again in its original state and therefore ready to pick up another transfer strand from the storage area. Since the antibody–peptide bond is reversible, this pick-up and deposit

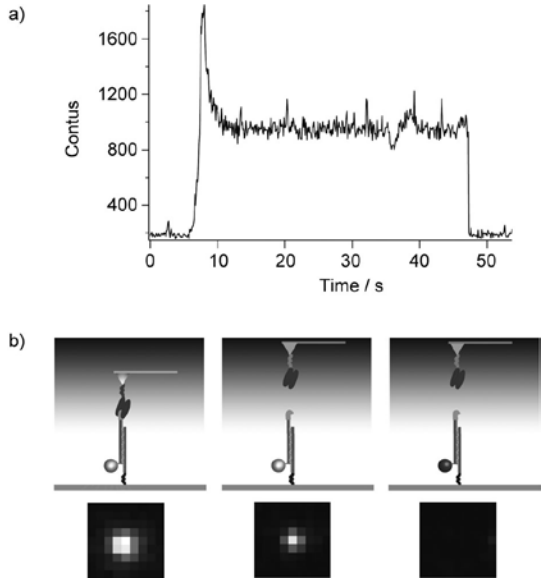

Figure 3. Deposition of a single DNA–peptide construct. The loaded cantilever is lowered towards the target area, where the DNA–peptide construct is deposited, when the lever is withdrawn. a) Fluorescence timetrace and b) cartoon of the process. When the cantilever enters the evanescent field of the TIR illumination, fluorescence from the dye-labeled construct and scattered light from the cantilever tip contribute to the signal, whereas after retraction of the cantilever, only fluorescence of the dye molecule is measured. No signal is measured after photobleaching of the dye.

or—in other words—molecular cut-and-paste process may be carried out for many cycles, allowing one molecule after the other to be transferred, unless damage to the antibody occurs during the forced unbinding of the antibody–peptide complex. To demonstrate that the antibody–peptide complex is robust and very well suited as handle complex at the AFM tip, we assembled the molecular pattern depicted in Figure 4 from approximately 600 transfer strands in a molecule-by-molecule copy-and-paste process. This convincingly demonstrates that the hierarchical force system, which is a prerequisite for SMC&P, may well be realized based on peptides or protein modules for anchor and/or handle groups. One may as well envisage covalent or organometallic coupling schemes[22,23] or even external modulation of the interaction forces by externally controlled Coulomb interactions[24] to expand the toolbox for single-molecule assembly.

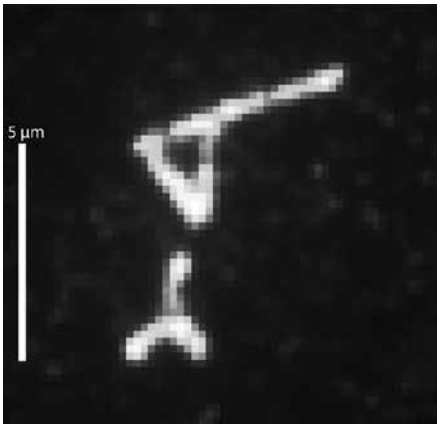

Figure 4. The robustness of the SMC&P process is demonstrated by the molecule-by-molecule assembly of a microscopic pattern showing a cantilever and an antibody. The pattern is assembled from approximately 600 molecules.

Experimental Section

All measurements described in the manuscript were carried out with a custom-designed combined AFM/TIRF microscope described in detail elsewhere.[21] We provide a detailed description of AFM measurements, TIRF microscopy, single-chain antibody fragment preparation, peptide synthesis, surface preparation, microstructuring with a microplotter, and oligomer sequences in the Supporting Information.

Acknowledgements

This work was supported by the Volkswagen foundation, the Nano Initative Munich and the German Science Foundation (SFB 863).

Keywords: biophysics · nanostructures · scanning probe microscopy · single-molecule studies · TIRF microscopy

[1] R. P. Feynman, *Eng Sci* **1960**, *23*, 22–36.
[2] M. F. Crommie, C. P. Lutz, D. M. Eigler, *Science* **1993**, *262*, 218–20.
[3] T. A. Jung, R. R. Schlittler, J. K. Gimzewski, H. Tang, C. Joachim, *Science* **1996**, *271*, 181–184.
[4] H. Kuhn, *Verhandlungen der Schweizerischen Naturforschenden Gesellschaft* **1965**, 245–266.
[5] R. Baum, *Chem. Eng. News* **2003**, *81*, 37–42.
[6] S. K. Kufer, E. M. Puchner, H. Gumpp, T. Liedl, H. E. Gaub, *Science* **2008**, *319*, 594–6.
[7] G. Binnig, C. F. Quate, C. Gerber, *Phys. Rev. Lett.* **1986**, *56*, 930–933.
[8] B. Drake, C. B. Prater, A. L. Weisenhorn, S. A. C. Gould, T. R. Albrecht, C. F. Quate, D. S. Cannell, H. G. Hansma, P. K. Hansma, *Science* **1989**, *243*, 1586–1589.
[9] E. M. Puchner, S. K. Kufer, M. Strackharn, S. W. Stahl, H. E. Gaub, *Nano Lett.* **2008**, *8*, 3692–5.
[10] W. E. Moerner, L. Kador, *Phys. Rev. Lett.* **1989**, *62*, 2535–2538.
[11] T. Schmidt, G. J. Schutz, W. Baumgartner, H. J. Gruber, H. Schindler, *Proc. Natl. Acad. Sci. USA* **1996**, *93*, 2926–9.
[12] R. D. Vale, T. Funatsu, D. W. Pierce, L. Romberg, Y. Harada, T. Yanagida, *Nature* **1996**, *380*, 451–3.
[13] A. Zurner, J. Kirstein, M. Doblinger, C. Bräuchle, T. Bein, *Nature* **2007**, *450*, 705–8.
[14] G. Seisenberger, M. U. Ried, T. Endress, H. Buning, M. Hallek, C. Bräuchle, *Science* **2001**, *294*, 1929–32.
[15] S. K. Kufer, M. Strackharn, S. W. Stahl, H. Gumpp, E. M. Puchner, H. E. Gaub, *Nat Nanotechnol* **2009**, *4*, 45–9.
[16] C. Zahnd, S. Spinelli, B. Luginbuhl, P. Amstutz, C. Cambillau, A. Pluckthun, *J Biol Chem.* **2004**, *279*, 18870–7.
[17] J. Morfill, J. Neumann, K. Blank, U. Steinbach, E. M. Puchner, K. E. Gottschalk, H. E. Gaub, *J. Mol. Biol.* **2008**, *381*, 1253–66.
[18] J. Morfill, K. Blank, C. Zahnd, B. Luginbuhl, F. Kuhner, K. E. Gottschalk, A. Pluckthun, H. E. Gaub, *Biophys. J.* **2007**, *93*, 3583–90.
[19] G. Neuert, C. H. Albrecht, H. E. Gaub, *Biophys. J.* **2007**, *93*, 1215–23.

[20] F. Kühner, H. E. Gaub, *Polymer* **2006**, *47*, 2555 – 2563.
[21] H. Gumpp, S. W. Stahl, M. Strackharn, E. M. Puchner, H. E. Gaub, *Rev. Sci. Instrum.* **2009**, *80*, 063704.
[22] B. M. Gaub, C. Kaul, J. L. Zimmermann, T. Carell, H. E. Gaub, *Nanotechnology* **2009**, *20*, 434002.
[23] P. Knochel, S. Z. Zimdars, S. X. M. du Jourdin, F. Crestey, T. Carell, *Org. Lett.* **2011**, *13*, 792 – 795.
[24] M. Erdmann, R. David, A. R. Fornof, H. E. Gaub, *Nat. Chem.* **2010**, *2*, 745 – 9.

Received: September 29, 2011
Published online on December 19, 2011

CHEMPHYSCHEM

Supporting Information

Peptide–Antibody Complex as Handle for Single-Molecule Cut & Paste

Mathias Strackharn,[a] Stefan W. Stahl,[b] Philip M. D. Severin,[a] Thomas Nicolaus,[a] and Hermann E. Gaub*[a]

cphc_201100765_sm_miscellaneous_information.pdf

Supplementary Information

Peptide:Antibody Complex as Handle for Single-Molecule Cut & Paste

Mathias Strackharn[1,*], Stefan W. Stahl[1,2], Philip M. D. Severin[1] Thomas Nicolaus[1], and Hermann E. Gaub[1]

[1] Center for Nanoscience and Department of Physics, University of Munich, Amalienstraße 54, 80799 Munich, Germany

[2] Center for Integrated Protein Science (CIPSM), Munich, Germany

[*] mathias.strackharn@physik.uni-muenchen.de

All measurements described in the manuscript were carried out with a custom designed combined AFM/TIRF microscope described in detail in [21]. Here twe provide the description of those parts and procedures, which are relevant to the experiments described in the main text:

AFM measurements

The spring constants of the DNA modified cantilevers were calibrated in solution using the equipartition theorem [25],[26]. For the single-molecule force spectroscopy BL-AC40TS-C2 levers (Olympus, Tokyo, Japan) and for SMC&P experiments MLCT-AUHW levers (Bruker, Camarillo, USA) were used. The protocol for the functional assembly as well as the data recording was programmed using Igor Pro (Wave Metrics, Lake Oswego, USA) and an Asylum Research MFP3D controller (Asylum Research, Santa Barbara, USA), which provides ACD and DAC channels as well as a DSP board for setting up feedback loops. Cantilever positioning for pick-up and delivery was controlled in closed-loop operation. The typical cycle time for one functional assembly process lies between 2 and 3 seconds depending on the sample orientation and the

traveling distance between depot and target area. The positioning feedback accuracy is ±3 nm however long term deviations may arise due to thermal drift. Extension velocities are set to 2 μm/s in the depot area and 200 nm/s in the target area. Force spectroscopy data was converted into force-extension curves and the most probable rupture force was obtained using a the program IGOR Pro 6.22 (Wave Metrics, Lake Oswego, USA) and a set of custom-made procedures. Rupture forces for each retraction speed were plottet in histograms and fitted with Gaussians to determine the most probable rupture forces.

TIRF microscopy

The fluorescence microscopy measurements were carried out with objective-type TIRF excitation on a microscope that was especially designed for a stable combination of AFM with TIRFM [21]. We excited with a fiber-coupled 637 nm diode laser (iBeam smart, TOPTICA, München, Germany) through a 100x/1.49 oil immersion objective lens (Nikon CFI Apochromat TIRF, Japan). As excitation filter, beam splitter, and emission filter a BrightLine HC 615/45, a Raman RazorEdge 633 RS, and a Chroma ET 685/70 (AHF, Tübingen, Germany) were used respectively. Images were taken with a back-illuminated EMCCD camera (DU-860D, Andor, Belfast, Ireland). Fluorescence image sequences were taken at 10 Hz frame rate, gain 150, 1 MHz readout rate in frame transfer mode. The camera was operated at -75 °C.

Preparation of the C11L34 single chain antibody fragment

The C11L34 single chain antibody fragment was prepared as described in [18]. The scFv construct harbored a C-terminal His tag followed by a Cys to allow for site-specific immobilization and was obtained by periplasmic expression in *E. coli* SB536. C11L34 was purified by Ni^{2+} and immobilized antigen affinity chromatography according to standard protocols. The concentration was adjusted to 2.5 mg/ml in storage buffer containing 50 mM sodium phosphate, pH 7.2, 50 mM NaCl and 10 mM EDTA.

Preparation of GCN4 peptides

GCN4 peptides with the sequence CYHLENEVARLKK were synthesized manually in syringe reaction chambers. 0.05 g Wang resin (Iris, Marktredwitz, Germany) were incubated with 10 eq (of the maximal loading capacity of the resin) Fmoc-L-Lys(Boc)-OH (Iris, Marktredwitz, Germany) for 4 h. The incubation was repeated for another 4 h. For the measurement of the resin loading 500 μl of DMF (Sigma, Taufkirchen, Germany) wih 20 % Piperidine (Fluka, St. Gallen, Switzerland) were added to 3 mg of the resin. The solution was shaken for 1 h, the 3 ml DMF were added. By measuring the extinction at 300 nm of a 1:10 dilution with DMF with 20% Piperidine the resin loading was determined. Remaining hydroxyl groups on the Wang resin were blocked by esterification with acetic anhydride. All other Fmoc-protected amino acids (Iris, Marktredwitz, Germany) were added by applying the following procedure: 10 eq amino acid and 100 eq HOBT (Fluka, St. Gallen, Switzerland) were dissolved in DMF, 10 eq DIC (Fluka, St. Gallen, Switzerland) was added and the solution was shaken for 1 h. Then 10 eq DIPEA (Fluka, St. Gallen, Switzerland) were added and solution was shaken for 1h again. The process was once repeated. Then then the resin was washed with 10 ml DMF, 10 ml DCM, 10 ml Ether and 6 ml DMF, again. Fmoc protection groups were removed by incubating the resin in DMF with 20 % Piperidine for 20 min twice. The resin was then flushed with 10 ml DMF, 10 ml DCM (Carl Roth, Karlsruhe, Germany), 10 ml Ether (Sigma, Taufkirchen, Germany) and 6 ml DMF. The peptide was finally separated from the resin by 3 h shaking in 50 μl p-Thiocresol (Fluka, St. Gallen, Switzerland), 50 μl Thioanisol (Fluka, St. Gallen, Switzerland) and 300 μl TFA (Sigma, Taufkirchen, Germany). The solution was transferred into a centrifuge tube, where the peptide was precipitated with 10 ml Ether at -80 °C. The solution was centrifuged at 4 °C and 4600 g and the pellet was washed in Ether six times. Finally the pellet was resolved in a 3:1 ddH_2O/tertButanol (Sigma, Taufkirchen, Germany) solution and lyophilized.

Preparation of cantilevers

Cantilevers (MLCT, Bruker, Camarillo, USA) were always oxidized in a UV-ozone Cleaner (UVOH 150 LAB, FHR Anlagenbau GmbH, Ottendorf-Okrilla, Germany). For single molecule force spectroscopy experiments and single molecule deposition they were silanized with 3-aminopropydimethylethoxysilane (ABCR, Karsruhe, Germany), baked at 80 °C, pre-incubated with sodium borate buffer (pH 8.5), PEGylated with NHS-PEG-Maleimide (MW 5000, Rapp Polymere, Tübingen, Germany), and washed with ddH2O. According to the experiment type either C11L34 antibodies at a concentration of 2.5 mg/ml or reduced thiolated transfer DNA at a concentratioin of 10 μM was bound to the pegylated cantilevers at 8 °C for 2 h. Cantilevers were then washed with PBS buffer. In case of the SMC&P experiment, where molecules were assembled to the pattern of a cantilever with antibody at the tip, the cantilever was silanized with (3-Glycidoxypropyl)trimethoxysilane (ABCR, Karlsruhe, Germany), baked at 80 °C for 30 min and incubated overnight at 8 °C with 1mg/ml aminodextrane (D1861, Invitrogen, Carlsbad, USA) in sodium borate buffer (pH 8.5). NHS-PEG-Mal was then applied to the cantilever, which was then washed in ddH_2O. Subsequently C11L34 antibodies at a concentration of 2.5 mg/ml were bound to the pegylated cantilevers at 8 °C for 2 h. The cantilever was finally washed with PBS.

Preparation of cover glass surfaces

Cover glass slips were sonicated in 50% (v/v) 2-propanol and ddH2O for 15 min and thoroughly rinsed with ddH2O. They were then oxidized in 50% (v/v) sulfuric acid and hydrogen peroxide (30%) for 45 min and were then again well rinsed with ddH2O. The oxidized cover glass slips were silanized with a mixture of 2% 3-aminopropyldimethylethoxysilane, 90% EtOH, 8% ddH2O for 1 h. Cover glasses were thoroughly rinsed with pure EtOH first and ddH2O afterwards, and were baked at 80 °C for 30 min. After 30 min soaking in 50 mM sodium borate buffer, pH 8.5 the cover glasses were treated with 50 mM NHS-PEG-maleimide (MW 5000) in the sodium borate buffer for 1 h and then rinsed with ddH2O.

In case of the SMC&P experiments depot and target oligomers were reduced, purified and dissolved again. The reduced thiolated depot and target oligomers were deposited with a microplotter (GIX, Sonoplot, Middleton, USA), nonbound DNA was washed away with ddH_2O. Transfer oligomers were deposited on top of the depot area. Nonbound transfer strands were washed away with 4xPBS buffer. (Details on the microstructuring process are given in the following section.) The sample was then covered with 50 mM sodium borate buffer, pH 8.5, 500 mM NaCl, 10 mM TCEP for 30 min for deprotonation of amines and quenching of unreacted maleimides. The sample was then rinsed with 50 mM sodium borate buffer, pH 8.5, 500 mM NaCl and incubated for 1h with 10 mM NHS-PEG-Mal dissolved in 50 mM sodium borate buffer, pH 8.5, 500 mM NaCl. It was washed with PBS, then reduced GCN4 peptides at a concentration of 100 μM in 50 mM sodium phosphate buffer, pH 7.2, 250 mM NaCl, 10 mM EDTA were added for 1 h. The sample was rinsed again with PBS.

For single molecule force spectroscopy reduced thiolated depot or target oligomers or the reduced GCN4 peptide was bound to the pegylated cover glass slips and the sample was thoroughly rinsed with water.

Structuring surfaces with a Microplotter

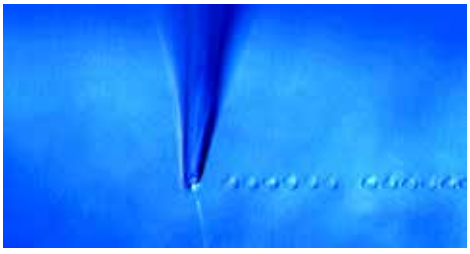

Due to the limited travel range of the AFM, the depot and target area have to be created in a distance of several micometers. For this reason these areas are produced by micro-structuring the cover glass with a microplotter (GIX, Sonoplot, Middleton, USA). A standard glass capillary (World Precision Instruments, Inc.) with an inner diameter of 30 μm was used, which results in spots of the diameter of 45 μm to 50 μm on the cover glass

(dispenser voltage 3V and 0.1 s dispensing time). The prepared DNA Oligomer solutions (see previous section) were plotted on the pegylated cover glass in two 800 μm long lines for depot and target, which were separated by a 20 μm to 30 μm broad gap.

After plotting the depot line, the cover glass was rinsed with 5 ml (4x PBS) directly in the sample holder without moving it. In a second step, the transfer strand was plotted onto the depot line. Operating experience showed that in the case of hybridizing DNA via Microplotter a contact time (capillary on the cover slide) of around 20 s per spot optimized the density of hybridized transfer strands. Afterwards the sample was rinsed as before. In a last step, the target strand was plotted in same manner as the depot.

Oligomer sequences

thiolated depot oligomer

5' SH - TTT TTT CAT GCA AGT AGC TAT TCG AAC TAT AGC TTA AGG ACG TCA A

thiolated target oligomer

5' CAT GCA AGT AGC TAT TCG AAC TAT AGC TTA AGG ACG TCA ATT TTT - SH

transfer oligomer with amine and Atto647N

5' (Atto647N) - TTG ACG TCC TTA AGC TAT AGT TCG AAT AGC TAC TTG CAT GTT TTT TTT - NH_2

thiolated transfer oligomer

5' TTG ACG TCC TTA AGC TAT AGT TCG AAT AGC TAC TTG CAT GTT TTT TTT - SH

1. H. Gumpp, S. W. Stahl, M. Strackharn, E. M. Puchner, H. E. Gaub, Ultrastable combined atomic force and total internal reflection fluorescence microscope [corrected]. *The Review of scientific instruments* **80**, 063704 (Jun, 2009).
2. E. Florin, Sensing specific molecular interactions with the atomic force microscope. *Biosensors and Bioelectronics* **10**, 895 (1995).
3. H. J. Butt, M. Jaschke, Calculation of thermal noise in atomic-force microscopy. *Nanotechnology* **6**, 1 (1995).

4. J. Morfill *et al*., Affinity-matured recombinant antibody fragments analyzed by single-molecule force spectroscopy. *Biophys J* **93**, 3583 (Nov 15, 2007).

5. A. Krebber *et al*., Reliable cloning of functional antibody variable domains from hybridomas and spleen cell repertoires employing a reengineered phage display system. *J Immunol Methods* **201**, 35 (Feb 14, 1997).

6. H. Bothmann, A. Pluckthun, Selection for a periplasmic factor improving phage display and functional periplasmic expression. *Nat Biotechnol* **16**, 376 (Apr, 1998).

7. J. Hanes, L. Jermutus, S. Weber-Bornhauser, H. R. Bosshard, A. Pluckthun, Ribosome display efficiently selects and evolves high-affinity antibodies in vitro from immune libraries. *Proc Natl Acad Sci U S A* **95**, 14130 (Nov 24, 1998).

Publikation 6

Functional Assembly of Aptamer Binding Sites by Single-Molecule Cut-and-Paste.

Strackharn, M.; Stahl, S. W.; Puchner, E.M.; Gaub, H. E.; Nano Lett 2012,

NANO LETTERS

Letter

pubs.acs.org/NanoLett

Functional Assembly of Aptamer Binding Sites by Single-Molecule Cut-and-Paste

Mathias Strackharn,[†] Stefan W. Stahl,[‡] Elias M. Puchner,[§] and Hermann E. Gaub*[,†]

[†]Center for Nanoscience and Department of Physics, University of Munich, Amalienstraße 54, 80799 Munich, Germany

[‡]Center for Integrated Protein Science (CIPSM), Munich, Germany

Supporting Information

ABSTRACT: Bottom up assembly of functional molecular ensembles with novel properties emerging from composition and arrangement of its constituents is a prime goal of nanotechnology. By single-molecule cut-and-paste we assembled binding sites for malachite green in a molecule-by-molecule assembly process from the two halves of a split aptamer. We show that only a perfectly joined binding site immobilizes the fluorophore and enhances the fluorescence quantum yield by several orders of magnitude. To corroborate the robustness of this approach we produced a micrometer-sized structure consisting of more than 500 reconstituted binding sites. To the best of our knowledge, this is the first demonstration of one by one bottom up functional biomolecular assembly.

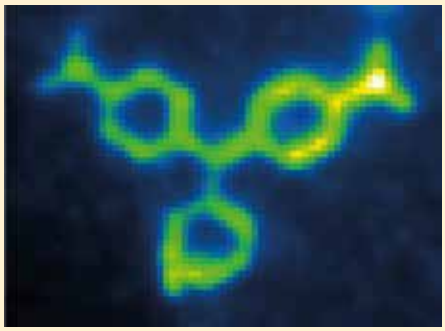

KEYWORDS: *Functional assembly, RNA aptamer, single-molecule cut-and-paste, single-molecule fluorescence, single-molecule force spectroscopy, atomic force microscope (AFM)*

Feynman is frequently quoted for having foreseen that individual atoms may be arranged one by one to form functional assemblies, moreover that covalent reactions between them may then provide a unique way to synthesize new molecules atom by atom.[1] The seminal work by Eigler and colleagues[2,3] convincingly proved the validity of these concepts: functional assemblies of atoms forming quantum corrals showed emergent novel properties. The application of these strategies to biomolecules, however, turned out to be much more challenging. A quite vivid dispute was fought in a series of papers between Smalley and Drexler on where these difficulties arise and whether fundamental limitations prevent the molecule for molecule assembly of biomolecules in electrolyte ambient at physiologic temperatures.[4] Hans Kuhn had realized early on that for many multistep biological reactions not only the sequence but also the arrangement of the individual enzymes plays a crucial role. He envisaged that in order to investigate their interaction, novel approaches would be needed; he wished to have molecular pliers to pick up and place individual enzymes to create functional assemblies with designed properties.[5]

With the development of single-molecule cut-and-paste (SMC&P), we provided a platform technology for the assembly of biomolecules at surfaces.[6] It combines the Å-positioning precision of the AFM[7,8] with the selectivity of DNA hybridization to pick up individual molecules from a depot area and arrange them at a construction site one by one.[9] We localized the pasted molecules with nanometer accuracy by single molecule fluorescence and showed that the deposition accuracy is presently limited by the length of the spacers used to couple the DNA handles and anchors to the tip and construction site, respectively.[10] We assembled structures with dimensions below the Abbé diffraction limit and imaged them by superresolution Blink-microscopy.[11] We thoroughly validated SMC&P and proved it to be a robust technology with the potential of high throughput. In this paper, we take the next important step and demonstrate the functional assembly of a biomolecular complex with a novel emergent property from individual building blocks one by one at a chosen position on a surface (see Figure 1).

Malachite green (MG) is a well-established red-emitting fluorophore whose quantum yield is known to depend strongly on the rotational degrees of freedom of its phenyl rings.[12,13] An increase in the quantum yield up to several orders of magnitude upon binding of this molecule to either BSA films,[14] specific antibody binding pockets[15] or suitable RNA structures[16,17] was reported in the literature. Particularly interesting appears the work by Kolpashchikov[18] where it was shown that a MG-aptamers may be split in two and used as DNA sensors with single mismatch resolution. Neither of the two aptamer halves was reported to improve the quantum yield of MG significantly, but both halves combined form a complete binding pocket and enhance the MG fluorescence by more than 3 orders of magnitude (cf. Supporting Information).

Received: February 1, 2012
Revised: March 28, 2012

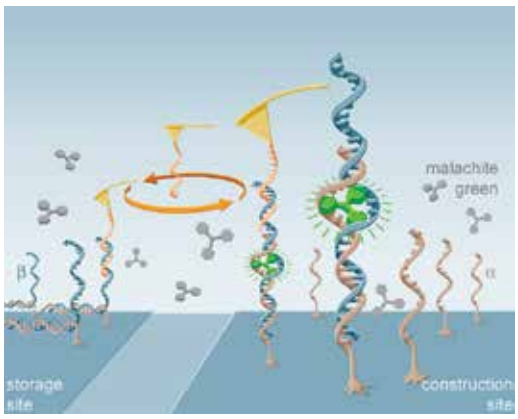

Figure 1. Schematics of the assembly of functional binding sites produced by SMC&P from individual α- and β-chains of a split malachite green aptamer. At the construction site, α-chains were covalently anchored at the 3′ end via PEG-spacers. At the storage site, β-chains were hybridized with a 40 bp overlap to an anchor oligo, which was covalently bound via its 5′ end to the surface. The other end of the β-strand had been extended by a 20 bases handle sequence, compatible to the corresponding handle oligo at the AFM cantilever tip. For transport, this handle oligo was brought into contact with a β-strand, allowing the two strands to hybridize. Upon retraction of the cantilever, the anchor oligo in unzip geometry yields and the β-strand is moved to the construction site, where it is positioned such that it hybridizes with an α-strand to form a complete MG binding site. Upon retraction of the tip, the handle sequence in shear geometry yields and the tip is free to pick up the next β-strand. When malachite green is bound in the fully assembled aptamer, its quantum yield is increased by more than 3 orders of magnitude, resulting in a bright fluorescence of the complex.

In order to directly compare the emission of individual MG aptamer complexes consisting of one α- and one β-strand each to that of Cy5 molecules under identical excitation and detection conditions, we covalently bound a very dilute layer (<1/5 μm^2) of β-strands with a thiol group at the 3′ end to a glass surface and then hybridized them with α-strands carrying one Cy5 label at the 3′ end. We identified individual Cy5 molecules by TIRF microscopy[19] and localized them by fitting Gauss functions to the intensity distributions. Once the Cy5 molecules were irreversibly photobleached (Figure 2 trace a) we added a 50 nM solution of MG and recorded the emission again. Now an intermittent signal was recorded. The fluorescent MG molecules were also localized to ensure that fluorescence from Cy5 and MG were collocalized (cf. Supporting Information). Trace b in Figure 2 shows a typical example of the intermittent emission pattern that we measured for extended periods of time up to several minutes. Note that the baseline of the MG emission is within an error bar of 10% indistinguishable from that of the bleached Cy5, which means that at the given concentration the free MG in solution does not significantly contribute to the measured fluorescence. It is not clear yet whether this pulsing fluorescence is caused by a change in the electronic structure of MG (e.g., population of triplet states) or by conformational changes in the molecular MG-aptamer complex (e.g., binding/unbinding of MG). It may as well reflect slow modes of the hybridization dynamics of the aptamer binding pocket. MG in the aptamer binding pocket might also become photobleached and replaced by intact MG

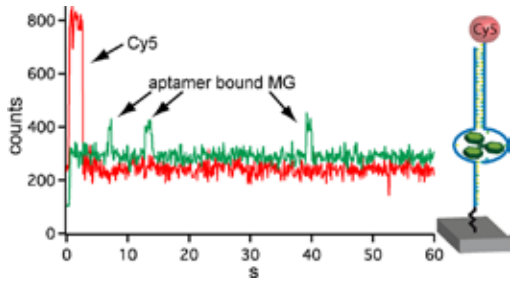

Figure 2. Typical fluorescence emission traces of individual molecules. In red, the emission of an individual Cy5 label at the 3′ end of an α-strand of the split MG-aptamer. After several seconds, the Cy5 is photobleached irreversibly and the emission drops to the background level. We then added 50 nM malachite green to the buffer solution and recorded the emission from the same aptamer under otherwise identical conditions (green trace). We measured a slightly increased background level and an intermittent fluorescence pattern with pulse durations of typically 3 ± 1 s. The typical height of the pulses was only one-fifth of the Cy5 emission. The insert depicts the molecular construct.

during these traces. Detailed future studies will be required to further elucidate these interesting phenomena.

Having verified that hybridization of the aptamer leads to a marked increase in the MG fluorescence at the surface, we assembled $\alpha\beta$-aptamer arrangements by SMC&P. We modified the split aptamers such that we were able to handle and reassemble them one by one to form fully functional MG binding sites. We used different areas on a cover glass for storage and construction sites (see Figure 1) and used a functionalized AFM tip to pick up individual β-aptamer strands from the depot side and to paste them in the construction site at a given position. Since the AFM tip is then ready again to pick up a β-aptamer strand, SMC&P can be operated as a cyclic process.

All experiments were carried out with a custom built AFM/TIRF hybrid microscope[20] as follows: In the presence of 50 nM MG in solution first the background image from the still empty construction site was recorded. Then the AFM tip was traversed toward the storage area and lowered toward the surface, while a force distance trace was recorded. The functionalization densities on the tip and the storage surface were chosen such that in approximately every third approach the handle oligos on the tip and a β-strand of the aptamer hybridized, resulting in a specific molecular multisegment chain between tip and surface. Upon retraction, the force is gradually built up in this chain, and the weakest of the segments yields (see Figure 3a). Note that the attachment geometries were chosen such that the handle oligos are loaded in shear geometry, which means that the hydrogen bonds are all loaded roughly equally, whereas the anchor is loaded in unzip geometry, which means that base pair for base pair sequentially unbinds. As a result, with a 95% likelihood it is the anchor that yields while the β-strand of the aptamer remains bound to the tip via its 20 bp handle. Despite the higher hybridization energy between the β-strand of the aptamer and the anchor oligo compared to the handle oligos, the force to open the hybrid in unzip geometry is much lower than the force required to open the hybrid in shear geometry because the mechanical work to separate the two halves is performed over a much larger distance than in the first case. Typical examples of the force distance traces recorded during the cut process are shown in

dx.doi.org/10.1021/nl300422y | Nano Lett. XXXX, XXX, XXX−XXX

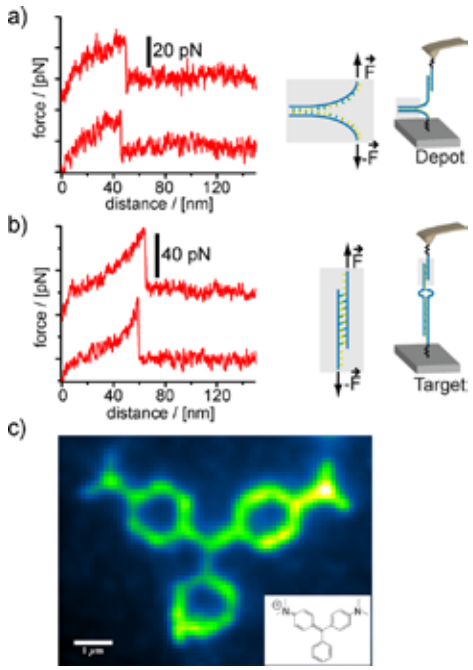

Figure 3. Typical force distance protocols of the cut (a) and paste (b) processes highlighted in Figure 1. (c) Fluorescence micrograph of a structure, consisting of more than 500 aptamers, which were assembled by SMC&P with the same tip. The insert shows the structural formula of MG that served as a blueprint of the arrangement.

Figure 3a. The rising parts of the curves reflect the entropic elasticity of the polymeric anchors, and the short plateau before the force drops to zero is caused by the unzipping of the DNA.

With the force distance curve corroborating that exactly one β-aptamer strand was picked up (see Figure 3a), the AFM tip was traversed to the construction side and lowered at a chosen position.[21] If the two halves of the split aptamer hybridize, again a chain is formed that is loaded when the tip is retracted from the surface. Since the two halves of the aptamer have a much longer sequence overlap than the handle oligos, the handle oligo complex yields (again with >90% probability) after which the tip is free to pick up a new molecule in the next cycle. Since again a force distance curve (see Figure 3b) was recorded, the deposition was either corroborated or a further attempt to paste the molecule was undertaken. Upon separation, the force distance traces depicted in Figure 3b show a continuous increase in force until the two strands loaded in shear geometry suddenly split in an all or none event and the force drops to zero.

In previous studies, we had shown that we can localize individual molecules by super resolution microscopy with an accuracy of better than 2 nm, and that the precision of the paste process is better than 10 nm. In this study here, we focused on the robustness of the process and repeated the cycle described above more than 500 times to assemble the pattern shown in Figure 3c. It depicts to the best of our knowledge the first example of a structure in which biomolecules were assembled one by one in a physiological ambient to perform a function, which emerges exclusively from their correct assembly. The bright fluorescence unambiguously corroborates that we have assembled functional binding sites from the two halves of the aptamer, and the well-pronounced contrast shows that we did so with superb selectivity.

This proof of principle opens the door toward the assembly of increasingly complex multicomponent systems at surfaces. Since we have already demonstrated that proteins or nanoparticles may be arranged by SMC&P, a large variety of systems with diverse molecular functions, which emerge from the unique arrangement of the constituents, may be envisioned. In combination with recent developments for the rapid production of protein libraries on microfluidic chips,[22] SMC&P will promote design and assembly of functional protein arrays or even entangled enzymatic networks.

■ ASSOCIATED CONTENT

Ⓢ Supporting Information

Details of material and methods, sample preparation, AFM measurements, TIRF-microscopy, fluorescence properties of the aptamer bound MG; additional results from nanometer precise localization and collocalization of Cy5 label and MG fluorescence. This material is available free of charge via the Internet at http://pubs.acs.org.

■ AUTHOR INFORMATION

Corresponding Author

*E-mail: gaub@lmu.de. Fax: +49 89 2180 2050.

Present Address

[§]Department of Cellular and Molecular Pharmacology, University of California, San Francisco, CA.

Notes

The authors declare no competing financial interest.

■ ACKNOWLEDGMENTS

This work was supported by the German Science Foundation and the Nanosystems Initiative Munich. Fruitful discussions with Ralf Jungman, Philip Severin, and Philip Tinnefeld are gratefully acknowledged.

■ REFERENCES

(1) Feynman, R. P. *Eng. Sci.* **1960**, *23* (5), 22–36.
(2) Crommie, M. F.; Lutz, C. P.; Eigler, D. M. *Science* **1993**, *262* (5131), 218–220.
(3) Jung, T. A.; Schlittler, R. R.; Gimzewski, J. K.; Tang, H.; Joachim, C. *Science* **1996**, *271* (5246), 181–184.
(4) Baum, R. *Chem. Eng. News* **2003**, *81* (48), 37–42.
(5) Kuhn, H. *Verh. Schweiz. Naturforsch. Ges.* **1965**, 245–266.
(6) Kufer, S. K.; Puchner, E. M.; Gumpp, H.; Liedl, T.; Gaub, H. E. *Science* **2008**, *319* (5863), 594–596.
(7) Binnig, G.; Quate, C. F.; Gerber, C. *Phys. Rev. Lett.* **1986**, *56* (9), 930–933.
(8) Drake, B.; Prater, C. B.; Weisenhorn, A. L.; Gould, S. A. C.; Albrecht, T. R.; Quate, C. F.; Cannell, D. S.; Hansma, H. G.; Hansma, P. K. *Science* **1989**, *243* (4898), 1586–1589.
(9) Puchner, E. M.; Kufer, S. K.; Strackharn, M.; Stahl, S. W.; Gaub, H. E. *Nano Lett.* **2008**, *8* (11), 3692–3695.
(10) Kufer, S. K.; Strackharn, M.; Stahl, S. W.; Gumpp, H.; Puchner, E. M.; Gaub, H. E. *Nat. Nanotechnol.* **2009**, *4* (1), 45–49.
(11) Cordes, T.; Strackharn, M.; Stahl, S. W.; Summerer, W.; Steinhauer, C.; Forthmann, C.; Puchner, E. M.; Vogelsang, J.; Gaub, H. E.; Tinnefeld, P. *Nano Lett.* **2010**, *10* (2), 645–651.
(12) Ben-Amotz, D.; Harris, C. B. *Chem. Phys. Lett.* **1985**, *119* (4), 305–311.
(13) Abedin, K. M.; Ye, J. Y.; Inouye, H.; Hattori, T.; Sumi, H.; Nakatsuka, H. *J. Chem. Phys.* **1995**, *103* (15), 6414.

(14) Bartlett, J. A.; Indig, G. L. *Dyes Pigm.* **1999**, *43* (3), 219–226.
(15) Szent-Gyorgyi, C.; Schmidt, B. F.; Creeger, Y.; Fisher, G. W.; Zakel, K. L.; Adler, S.; Fitzpatrick, J. A.; Woolford, C. A.; Yan, Q.; Vasilev, K. V.; Berget, P. B.; Bruchez, M. P.; Jarvik, J. W.; Waggoner, A. *Nat. Biotechnol.* **2008**, *26* (2), 235–240.
(16) Babendure, J. R.; Adams, S. R.; Tsien, R. Y. *J. Am. Chem. Soc.* **2003**, *125* (48), 14716–14717.
(17) Grate, D.; Wilson, C. *Proc. Natl. Acad. Sci. U.S.A.* **1999**, *96* (11), 6131–6136.
(18) Kolpashchikov, D. M. *J. Am. Chem. Soc.* **2005**, *127* (36), 12442–12443.
(19) Tokunaga, M.; Kitamura, K.; Saito, K.; Iwane, A. H.; Yanagida, T. *Biochem. Biophys. Res. Commun.* **1997**, *235* (1), 47–53.
(20) Gumpp, H.; Stahl, S. W.; Strackharn, M.; Puchner, E. M.; Gaub, H. E. *Rev. Sci. Instrum.* **2009**, *80* (6), 063704.
(21) If the force curve indicates that the pick up was not successful, the online control of the process allows for another pick-up attempt. If the force curve indicates that several molecules were picked up, they can be pasted in a "wastebasket" area rendering the tip ready again for the normal cycle.
(22) Gerber, D.; Maerkl, S. J.; Quake, S. R. *Nat. Methods* **2009**, *6* (1), 71–74.

dx.doi.org/10.1021/nl300422y | *Nano Lett.* XXXX, XXX, XXX–XXX

Supporting Information

Functional Assembly of Aptamer Binding Sites by Single-Molecule Cut-and-Paste

Mathias Strackharn[1], Stefan W. Stahl[1,2], Elias M. Puchner[1,3] & Hermann E. Gaub[1,*]

[1] Center for Nanoscience and Department of Physics, University of Munich, Amalienstraße 54, 80799 Munich, Germany

[2] Center for Integrated Protein Science (CIPSM), Munich, Germany

[3] The author has moved to the Department of Cellular and Molecular Pharmacology, University of California, San Francisco, 600 16th Street, San Francisco, CA 94158, USA

[*] gaub@lmu.de

All measurements described in the manuscript were carried out with a custom designed combined AFM/TIRF microscope described in detail in [1]. Here the description of those parts and procedures, which are relevant to the experiments described above:

AFM Measurements

The spring constants of the DNA modified cantilevers were calibrated in solution using the equipartition theorem [2,3]. For the single-molecule force-extension trace recordings BL-AC40TS cantilevers (Olympus Cooporation, Tokyo, Japan) were used with a typical spring constant of about 120 pN/nm and a resonance frequency of 30 kHz. This experiment was conducted in 100 mM sodium phosphate buffer, pH 5.5, 140 mM NaCl, 5 mM $MgCl_2$. For the functional assembly of the Malachite Green structure pattern MLCT-AUHW levers (Bruker, Camarillo, USA) were used. The protocol for the functional assembly as well as the data recording was programmed using Igor Pro (Wave Metrics) and an Asylum Research MFP3D controller, which provides ACD and DAC channels as well as a DSP board for setting up feedback loops. Cantilever positioning for pick-up and delivery was controlled in closed-loop operation. The typical cycle time for one functional assembly process lies between 2 and 3 seconds depending on the sample orientation and the traveling distance between depot and target area. The positioning feedback accuracy is ±3 nm however long term deviations may arise due to thermal drift. Extension velocities are set between 1 and 2.5 µm/s.

Measurements with TIRF microscopy

The fluorescence microscopy measurements were carried out with objective-type TIRF excitation on a microscope that was especially designed for a stable combination of AFM with TIRFM [1]. We excited with a fiber-coupled 639 nm diode laser (iBeam smart, TOPTICA, München, Germany) through a 100x/1.49 oil immersion objective lens (Nikon CFI Apochromat TIRF, Japan). As excitation filter, beam splitter, and emission filter a BrightLine HC 615/45, a Raman RazorEdge 633 RS, and a Chroma ET 685/70 (AHF, Tübingen, Germany) were used respectively. Images were taken with a back-illuminated EMCCD camera (DU-860D, Andor, Belfast, Ireland). After the functional assembly of the Malachite Green structure pattern 1 µM Malachite Green (Sigma, Taufkirchen, Germany) in PBS was added. For the single-aptamer fluorescence experiment single aptamers were identified by the fluorescence of the Cy5 label and its single-step bleaching. 100 nM Malachite Green in 100 mM sodium phosphate buffer, pH 5.5, 140 mM NaCl, 5 mM $MgCl_2$, was added. Fluorescence image sequences were taken at 10 Hz frame rate, gain 200, 1 MHz readout rate in frame transfer mode. The camera was operated at -80 °C.

Preparation of cantilevers

Cantilevers (MLCT, Bruker, Camarillo, USA, and Olympus AC40TS, Japan) were oxidized in a UV-ozone Cleaner (UVOH 150 LAB, FHR Anlagenbau GmbH, Ottendorf-Okrilla, Germany) and silanized with 3-aminopropydimethylethoxysilane (ABCR, Karsruhe, Germany), baked at 80 °C, pre-incubated with sodium borate buffer (pH 8.5), PEGylated with NHS-PEG-Maleimide (MW 5000, Rapp Polymere, Tübingen, Germany), and washed with ddH_2O as described in [4].

Thiolated cantilever DNA oligomers were reduced with 5 mM TCEP (Thermo Fisher Scientific, Rockford, USA) for 1 h at room temperature, purified by ethanol precipitation and dissolved again in a 50 mM sodium phosphate buffer, pH 7.2, 50 mM NaCl, 10 mM EDTA to a final concentration of 10 µM. The PEGylated cantilevers were then incubated at room temperature with the cantilever DNA oligomers for 1 h and rinsed with ddH_2O.

Preparation of cover glass surfaces

Cover glass slips were sonicated in 50% (v/v) 2-propanol and ddH_2O for 15 min and thoroughly rinsed with ddH_2O. They were then oxidized in 50% (v/v) sulfuric acid and hydrogen peroxide (30%) for 45 min and were then again well rinsed with ddH_2O. In addition a UV-ozone treatment was applied for 15 min. For the assembly of the Malachite Green structure pattern the cover glass slips were incubated overnight with 10 mg/ml amino dextran (MW 500000, Invitrogen, Carlsbad, USA), washed afterwards with ddH_2O and dried with a nitrogen stream. NHS-PEG-maleimide (MW 5000) was dissolved to 10 mM in a 50 mM sodium borate buffer, pH 8.5 and incubated on the cover glasses for 1 h. Cover glasses were then washed with ddH_2O. A microfluidic system was fixed on the cover glass. Thiolated depot DNA oligomers and target hybrid oligomers (IBA, Göttingen, Germany) were each reduced with 5 mM TCEP (Thermo Fisher Scientific, Rockford, USA) for 1 h at room temperature, purified by ethanol precipitation and dissolved again in a 50 mM sodium phosphate buffer, pH 7.2, 50 mM NaCl, 10 mM EDTA to a final concentration of 10 µM. The depot oligomers and the target hybrid oligomers were pumped through the respective channel of the microfluidics for 1 h. Both channels were then rinsed with ddH_2O. A solution 1 µM transfer hybrid oligomers and 5 nM Atto647N labelled

transfer oligomer in PBSwere pumped through the depot channel for 30 min. We used this minor fraction of fluorescent labelled DNA to allow for an exact alignment of the sample with the AFM cantilever. The channel was then rinsed with PBS to remove non-hybridized transfer hybrids. The microfluidic system was then removed again.

For force spectroscopy of the transfer process, the oxidized cover glass slips were silanized with a mixture of 2% 3-aminopropyldimethylethoxysilane, 90% EtOH, 8% ddH_2O for 1 h. Cover glasses were thoroughly rinsed with pure EtOH first and ddH_2O afterwards, and were baked at 80 °C for 30 min. After 30 min soaking in 50 mM sodium borate buffer, pH 8.5 the cover glasses were treated with 50 mM NHS-PEG-maleimide (MW 5000) in the sodium borate buffer for 1h and then rinsed with ddH_2O. As for the Malachite Green structure writing experiment, the depot oligomers and the target hybrid oligomers were reduced, purified and dissolved again. The reduced depot and target hybrid oligomers were deposited with a 30 µm capillary of a microplotter (GIX, Sonoplot, Middleton, USA) in two 800 µm long lines separated by around 30 µm. Molecules in solution were flushed away with ddH_2O and a line with 1 µM transfer hybrid oligomers and 5 nM of Atto647N labeled transfer oligomer in 4xPBS was plotted on top of the depot line. Non-hybridized oligomers were flushed away with 4xPBS.

For fluorescence spectroscopy experiments of single aptamers, the oxidized cover glass slips were functionalized with 10 mg/ml NHS-PEG-maleimide (MW 5000) in 50 mM sodium borate buffer, pH 8.5 for 1 h and then rinsed with ddH_2O. Thiolated transfer hybrid oligomers were reduced, purified and dissolved in the same fashion as described before. The cover glass slips were incubated with the reduced thiolated transfer hybrid for 1h, the sample was then washed with ddH_2O. Cover glasses were mounted an the fluorescence microscope and Cy5 labelled target

hybrid oligomers were hybridized in a 100 mM phosphate buffer, pH 5.5, 140 mM NaCl, 5 mM $MgCl_2$ to the surface bound transfer hybrid oligomers. The density was chosen such that it allowed for single molecule fluorescence spectroscopy. Buffer was exchanged several times to avoid unbound Cy5 labelled target hybrid oligomers in solution.

Preparation of the micro-fluidics chamber

Silicon elastomer and curing agent, (Sylgard 184, Dow Corning, Wiesbaden, Germany) were well mixed in a 10:1 ratio and were degassed twice at 20 mbar. The solution was poured on a silicon wafer with a lithographically prepared positive relief structure consisting of two parallel flow channels separated by 20 µm. The channels were 20 µm high, 100 µm broad, and about 1 cm long as shown in figure S 1. The system was degassed again and then baked at 60 °C for 1 h. When taken off of the silicon wafer, the PDMS elastomer has the negative structure of the flow channels on its lower side. Cannulas (Sterican, 0,80 x 22 mm, Carl Roth, Karlsruhe, Germany) were pierced through the PDMS in order to provide connections from the upper side to all ends of the channels. The lower side of the PDMS flow channels was contacted with the cover glass slips. A pump was connected to the cannulas on the upper side, such that oligomers and rinsing solutions could be pumped through the channels.

Sequences of the oligonucleotides

DNA bases are denoted with A, C, G, T. RNA bases are denoted with rA, rC, rG, rU. (All oligomers were purchased from IBA, Göttingen, Germany.)

thiolated cantilever oligomer:

5' SH- TTTTT CTGCAGGAATTCGATATCAA

thiolated depot oligomer:

5' SH- TTTTT AAGTAGCTATTCGAACTATAGCTTAAGGACGTCAA

thiolated target hybrid oligomer (α-part of the aptamer):

5' rCrCrA rGrGrU rArArC rGrArA rUrGrG rArUrU TAG CTA TTC GAA CTA TAG CTT AAG GAC GTC T -SH

transfer hybrid oligomer (β-part of the aptamer):

5' GAC GTC CTT AAG CTA TAG TTC GAA TAG CTA rUrUrU rCrCrC rGrArC rUrGrG TTT GAT ATC GAA TTC CTG CAG

thiolated transfer hybrid oligomer:

5' GAC GTC CTT AAG CTA TAG TTC GAA TAG CTA rUrUrU rCrCrC rGrArC rUrGrG TTT TTT T -SH

Cy5 labelled target hybrid oligomer:

5' rCrCrA rGrGrU rArArC rGrArA rUrGrG rArUrU TAG CTA TTC GAA CTA TAG CTT AAG GAC GTC T -Cy5

Atto647N labelled transfer oligomer:

5’ Atto647N-

TTTGACGTCCTTAAGCTATAGTTCGAATAGCTACTTTTTGATATCGAATTCCTGCAGT

Dissociation Constant of the the split Aptamer

In order to determine the K_d, the fluorescence of a constant amount (87 nM) of assembled aptamer at variable amounts of Malachite Green was measured with a fluorescence spectrometer (Fluoromax-3, JY Horiba, New Jersey, USA). The data is shown in figure S 2. The fit was performed with the function

$$f(MG_{tot}) = F_0 + (F_{max} - F_0) \cdot \frac{A_{tot} + MG_{tot} + K_d - \sqrt{(A_{tot} + MG_{tot} + K_d)^2 - 4A_{tot}MG_{tot}}}{2A_{tot}} \quad \text{(eq. S1)}$$

with F_0 the measured offset, F_{max} the maximum fluorescence, A_{tot} the concentration of the assembled aptamer, MG_{tot} the concentration of Malachite Green. This dependency follows directly from the law of mass action and the linear dependence of the overall fluorescence on the fractions of bound and unbound malachite green dye. K_d was determined to be 107±9 nM. This value compares to the K_d of the unsplit Malachite Green Aptamer of 117 nM [5].

Fluorescence Enhancement Properties

For the determination of the enhancement of quantum efficiency the fluorescence of 400 nM malachite green was measured alone and in presence of 200 nM α-part, β-part and both parts of the split aptamer hybridized in a fluorescence spectrometer. The results are shown in figure S 3,

S 4 and S 5. The measurement was performed in a 100 mM phosphate buffer, pH 5.5, 140 mM NaCl, 5 mM $MgCl_2$.

It follows from the law of mass action, that the concentration of aptamer bound malachite green is

$$[MGA] = \frac{[MG] + [A] + K_d - \sqrt{([MG] + [A] + K_d)^2 - 4[MG][A]}}{2} \quad \text{(eq. S2)}$$

The fluorescence output of the pure malachite green measurement is

$F_{MG} = f_{spectr} A Q_1 [MG]$ (eq. S3) and $F_{Apt} = f_{spectr} A\left(Q_1([MG] - [MGA]) + Q_2[MGA]\right)$ (eq. S4) the fluorescence output for the measurement with both parts of the split aptamer and malachite green. Kd is the dissociation constant, fspectr is a spectrometer specific constant, A the absorption of malachite green is approximately independent of the bound or unbound state, [A], [MG], and [MGA] are the concentrations of assembled aptamer, malachite green and malachite green-aptamer complex, and Q1, Q2 are the quantum efficiencies of unbound and bound malachite green, respectively. From this follows immediately that the enhancement of quantum efficiency is

$$\frac{Q_2}{Q_1} = \frac{\frac{F_{Apt}}{F_{MG}} + \frac{[MGA]}{[MG]} - 1}{\frac{[MGA]}{[MG]}} \quad \text{(eq. S5)}$$

.

The enhancement factor was here determined to be 1769±74, with K_d=107±9 nM, F_{Apt}/F_{MG}=747±15, [MG]=1000±10 nM, [MGA]=500±5 nM.

The fluorescence of either 500 nM either α-part or β-part of the split aptamer with 1 µM malachite green can directly be compared to the fluorescence of 1 µM malachite green only. It turns out that fluorescence is enhanced by around a factor 3 if either α- or β-part of the split aptamer are present.

profiles were calculated with ImageJ. Data was then imported into IGOR for further evaluation. The Cy5 fluorescence timetraces were background corrected because some background bleaching was overlaying. The background average value after bleaching was then added as an offset value to the fluorescence timetraces.

Single-Molecule Localization with NanometerAccuracy

The diffraction limited single molecule fluorescence distribution was taken in TIRF microscopy as described above. Fluorescence of Cy5 and the single aptamer-bound malachite green fluorescence events were averaged in ImageJ. Average images were then imported into IGOR for further calculations. The center of the fluorescence distribution was determined in IGOR by fitting a 2D gaussian to the distribution. A result is shown in figure S 7. Thermal drift on the order of 10 nm causes, that fluorescence events do not overlay exactly. Fitting errors are below 12 nm.

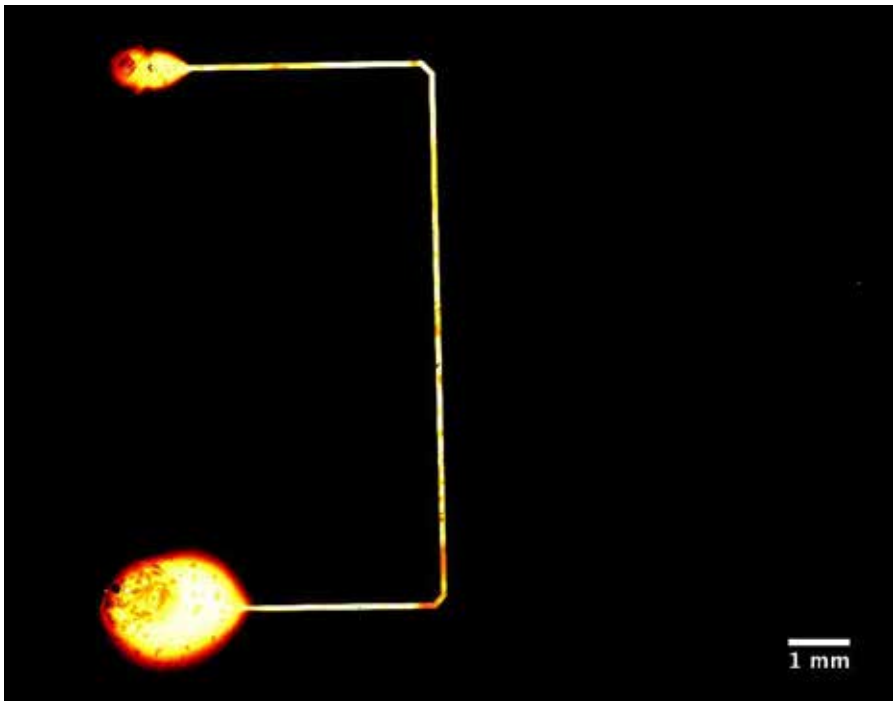

S 1. In a PDMS flow chamber a glass surface was functionalized in a depot region with thiolated depot oligomers. A dye labelled Transfer oligomer was then hybridized to the depot oligomers. The target region on the right side is functionalized with a thiolated target oligomer only. It canot be seen in fluorescence microscopy. The channel length is about 1 cm, the width 100 µm.

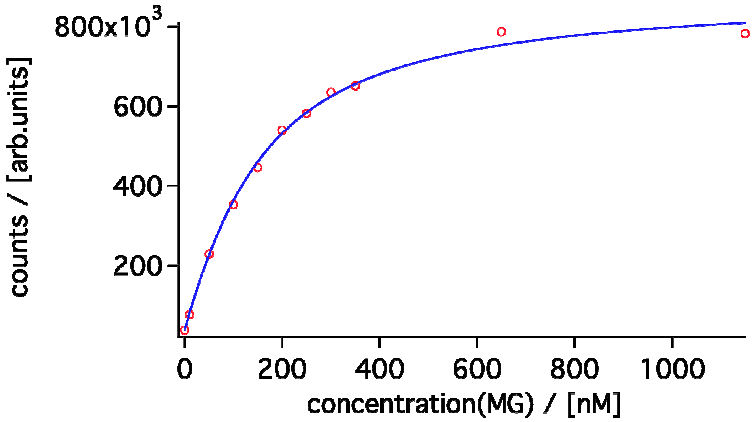

S 2. For the determination of the dissociation constant the fluorescence of aptamer bound malachite green was measured for different malachite green concentrations. The dissociation constant was determined to be 107±9 nM.

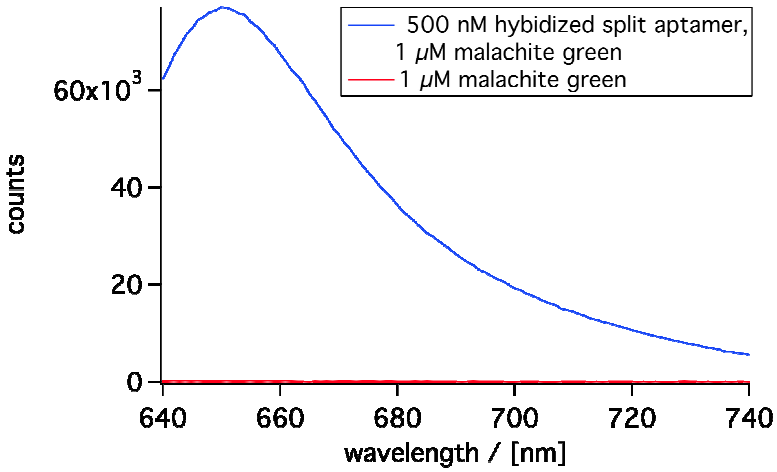

S 3. The combined split aptamer units enhance the quantum yield of malachite green by a factor of almost 1800 (blue curve). A detailed graph of the fluorescence of 1 µM malachite green only (red curve) is given in figure S 4.

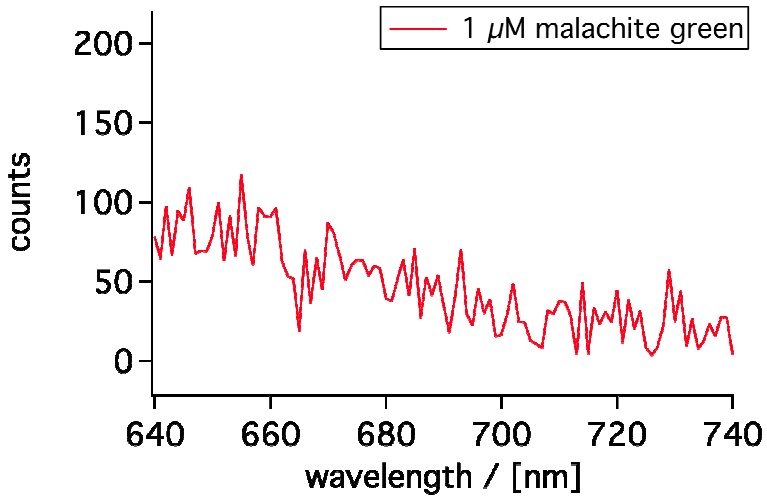

S 4. Fluorescence of 1 µM MG is depicted in this graph. It is extremely weak compared to the fluorescence of malachite green bound by the assembled aptamer.

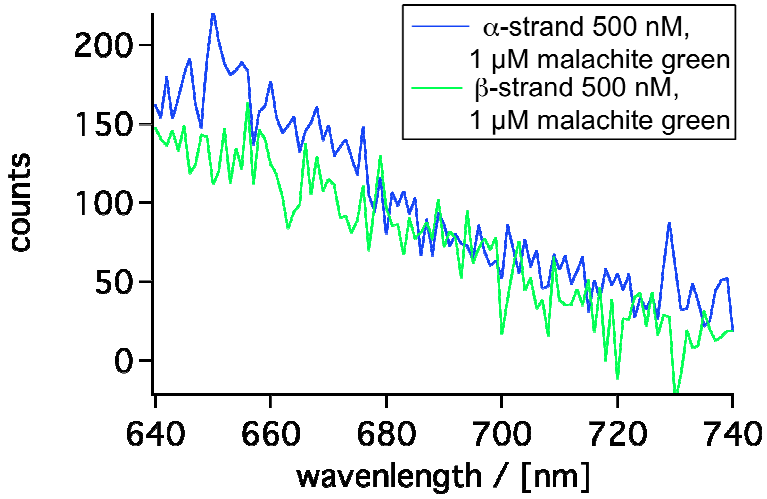

S 5. Fluorescence either of 500 nM α-strand (blue) or β-strand (green) is shown in this graph. Fluorescence of 1 µM malachite green is enhanced by only around a factor 3.

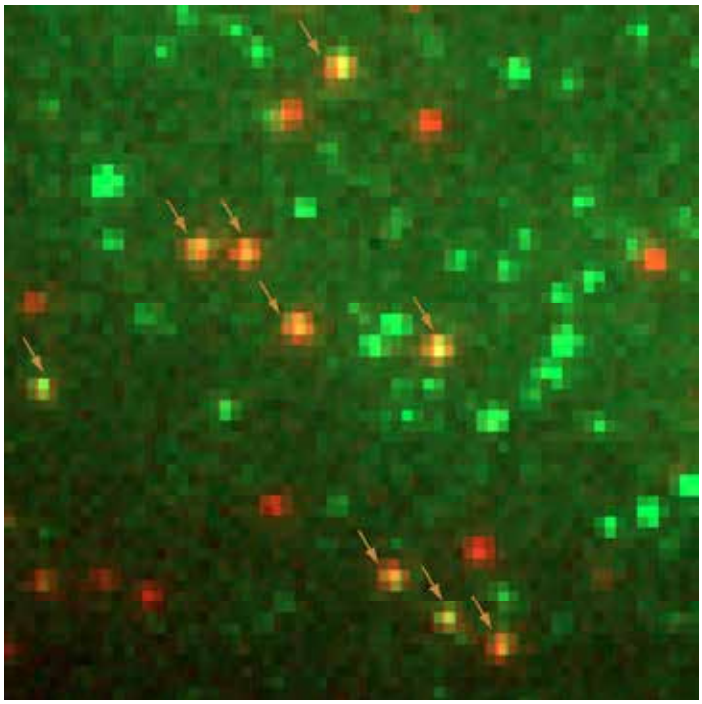

S 6. For the identification of individual functional aptamers, an averaged image of the Cy5 fluorescence (red) and an image of the malachite green fluorescence (green) were corrected for drift displacement and overlayed.

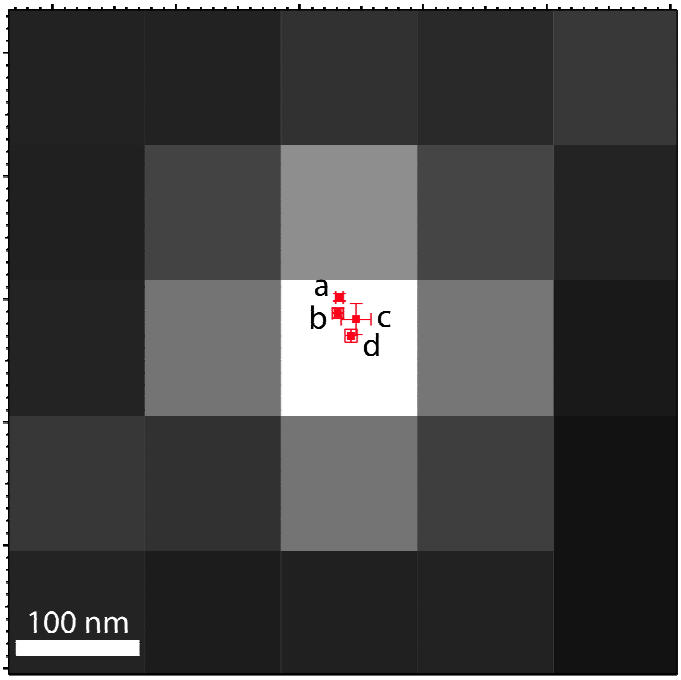

S 7. The positions of the Cy5 label (a), and the malachite green fluorescence bursts (b, c, and d in temporal order) were determined by fitting gaussians to the diffraction limited spots. The diffraction limited fluorescent pattern depicted in this graph is that of the malachite green fluorescence burst of (d). Error bars represent the fitting errors. Deviations from the original Cy5 position are on the order of 10 nm and can be assigned to thermal drift.

References:

1) Gumpp, H., Stahl, S.W., Strackharn, M., Puchner, E.M. & Gaub, H.E. Ultrastable combined atomic force and total internal reflection fluorescence microscope [corrected]. *The Review of scientific instruments* **80**, 063704 (2009).

2) Florin, E. Sensing specific molecular interactions with the atomic force microscope. *Biosensors and Bioelectronics* **10**, 895-901 (1995).

3) Butt, H.J. & Jaschke, M. *Nanotechnology* **6**, 1-7 (1995).

4) Zimmermann, J.L., Nicolaus, T., Neuert, G. & Blank, K. Thiol-based, site-specific and covalent immobilization of biomolecules for single-molecule experiments. *Nature protocols* **5**, 975-85 (2010).

5) Babendure, J.R., Adams, S.R. & Tsien, R.Y. Aptamers switch on fluorescence of triphenylmethane dyes. *Journal of the American Chemical Society* **125**, 14716-7 (2003).

Publikation 7

Nanoscale Arrangement of Proteins by Single-Molecule Cut&Paste. (submitted to JACS)

Strackharn, M.; Pippig, D.A.; Meyer, P.; Stahl, S. W.; Gaub, H. E.;

Nanoscale Arrangement of Proteins by Single-Molecule Cut&Paste

Mathias Strackharn[‡], Diana A. Pippig[*,‡], Philipp Meyer, Stefan W. Stahl[†], Hermann E. Gaub

Center for Nanoscience and Department of Physics, University of Munich, Amalienstraße 54, 80799 Munich, Germany

Supporting Information Placeholder

Protein-based nanostructures are key to the organization of life and it is their precise arrangement, which determines their specific functions. A single-molecule approach for the directed assembly of protein arrangements allows for a controlled composition of systems based on protein components. Applying antibodies and antigenic peptide tags we utilized the Single-Molecule Cut-and-Paste technique for the handling of single proteins. Protein-DNA complexes could be arranged to complex patterns with the functionality of the protein part remaining unimpaired.

The ability to arrange individual proteins in a controlled manner on a surface is a prerequisite for the study of complex systems e.g. of enzyme networks as a function of composition and alignment. With Single-Molecule Cut-and-Paste a technique for one-by-one arrangement of molecules under physiological conditions was implemented[1]. With this technique the bottom-up assembly of biomolecular structures from biological building blocks has already been demonstrated successfully in several examples. Utilizing attachment geometries resulting in different binding forces, single DNA molecules can be repeatedly picked up from a depot region by a functionalized AFM tip and then be placed with the precision of an AFM[2] on a target surface. The accuracy of the molecular deposition process was shown to depend on the length of the crosslinker, which serves to couple the anchor DNA to the surface[3]. Until today applications of this technique were solely realized by making use of a DNA-based hierarchical force system for pick up and deposition[4-6]. To make the SMC&P technology accessible to the field of protein science, an approach beyond mere DNA interactions is needed. We recently established an alternative implementation of a hierarchical force system, which replaces the DNA handle interaction between the transfer molecule and the AFM tip by a peptide:antibody complex[7]. Such an interaction is desirable for the transport of single proteins. A prerequisite for this is the construction of fusion proteins harboring small antigenic peptide tags, which serve as handles on the protein of interest. Thus a fully expressible system is obtained that does not require any additional modification of the protein.

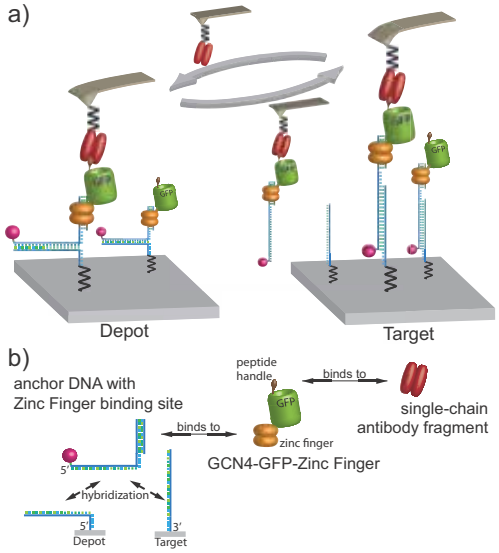

Figure 1. a) Schematics of the transfer process. The GCN4-GFP-Zinc Finger construct is bound with high affinity to the anchor DNA and stored via hybridization in the depot area. A single-chain antibody fragment, which is covalently attached to the cantilever tip, seizes the GCN4-tag, the DNA in unzip geometry opens up when the cantilever is lifted. The GCN4-GFP-Zinc Finger construct with the anchor DNA can then be transferred to the target site, where the shear geometry bond to the target DNA is stronger than the bond between antibody and GCN4 peptide. The protein construct is deposited in the target area, whereas the antibody on the cantilever is free again and can be reused in the next transfer cycle. b) Toolbox for the protein transport. The GCN4-GFP-Zinc Finger fusion protein can specifically bind to the DNA anchor strand via the Zinc Finger domain at the C-terminus. The N-terminal GCN4 peptide serves as a handle to pick up the complex.

For a first realization of a molecule-by-molecule arrangement of proteins based on this force system, an engineered fusion construct consisting of a Zinc Finger[8] and a GFP[9,10] moiety was used, allowing for positioning with mechanical control. A single-chain antibody fragment, that recognizes the 34 residue GCN4(7P14P) random coil peptide[11,12] was employed as handle system. For anchoring the construct to depot and target site DNA hybridization was utilized. Thus a connection between protein moiety and the DNA anchors is required. To this aim we used a six Zinc

Finger construct that contains the three finger peptide Zif268 and its mutated variant NRE[13] separated by a flexible linker. Zif268/NRE binds sequence specifically and with a sub-picomolar affinity to a 29 bp dsDNA[14]. The GCN4-GFP-Zinc Finger fusion construct was expressed in E. coli. Purified protein was bound to a connection DNA harboring the Zinc Finger target sequence and a 70 nucleotide long overhang. This contains a 30 nt spacer and 40 nt stretch chosen such, that it can hybridize with the anchor sequence in the depot and in the target area. In addition the connector DNA was labeled with a Cy5 dye.

Utilizing a microfluidics system[15] mounted on a cover slip we created a depot and a target site by functionalizing the glass surface with anchor DNAs. On the depot site these oligonucleotides were covalently attached at their 5' end, on the target site at the 3' end. Then the complex of the GCN4-GFP-Zinc Finger fusion protein with the connector DNA was hybridized to the depot anchors. The single-chain antibody fragments were covalently bound to the cantilever tip. For the cyclic transfer of the proteins to the target site (Fig. 1) the cantilever is first lowered towards the depot area, where the antibody is allowed to bind to the GCN4 peptide of the protein construct. In retracting the cantilever, all bonds of the system are loaded with the same force in series. Since the hybridization bond to the anchor DNA is in unzip geometry, the DNA strands separate base pair after base pair at a very low rupture force of about 25 pN, while the protein:connector-DNA complex remains attached to the cantilever, since the unbinding force of the peptide:antibody complex exceeds 40 pN at the given force loading rates. The cantilever with the Zinc Finger:DNA complex can then be moved by an xy-piezo system with Å precision to a predefined position in the target area. When the cantilever is lowered again, the connector DNA hybridizes to the anchor DNA. By subsequent retraction of the cantilever the hybridization bond is, in contrast to the depot process, loaded now in shear geometry. Because in this geometry all base pairs of the double strand are loaded in parallel, the rupture forces for opening up the DNA duplex bond are in the range of 60 pN. Since the antibody:peptide complex is already broken up at forces of 40 pN[7] the protein construct is detached from the cantilever and remains bound to the designated position on the target site via its DNA anchor. The antibody at the cantilever is thus free again and can be reused for the next cut & paste cycle. It should be noted that the damage to the cantilever, e.g. by unfolding of the antibody is negligible allowing for several thousands of repeated cycles. Due to its very high affinity, the Zinc Finger-DNA complex was stable during the transfer[16].

We were able to simultaneously follow the single-molecule transfer in force spectroscopy[17,18] and fluorescence spectroscopy[19]. During each of these cut & paste steps we independently confirmed by recording the force distance traces that individual molecules were handled. Fig. 2 shows a gallery of typical traces. In a) the force plateau prior to rupture is characteristic for the unzipping of handle and anchor DNA whereas in b) the peak is typical for the all or none rupture of the antibody:peptide bond. The blank traces show that not in all cases we were able to pick up or deliver a molecule, which required a retry.

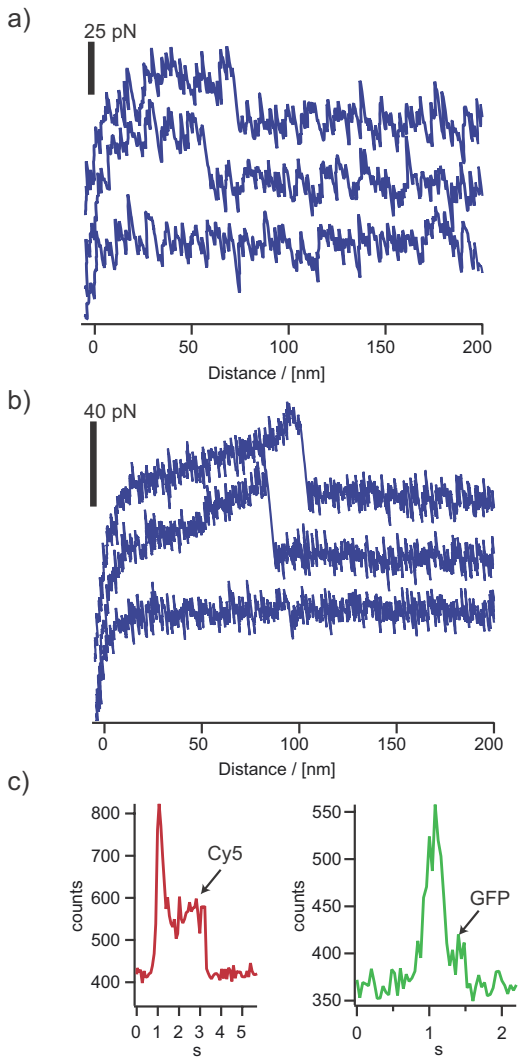

Figure 2. Typical force curves from a) the depot region and b) the target region. The cutting process in the depot region ends with a short plateau in the force-distance curve when the DNA is unzipped. When pasting the construct to the target area, the break of the antibody:antigen bond results in a sudden drop of the gradually built up force. In some cases no molecules were picked up or delivered, which is reflected in the zero-force curves. c) The deposition process can be monitored in TIRF microscopy. Photons scattered from the cantilever and those emitted by the dye contribute both to the overall signal, when the cantilever enters the evanescent field. After the cantilever is retracted, fluorescence of the Cy5 (left) or GFP (right) remains until stepwise photobleaching occurs.

Fig. 2 c) shows the time traces of a deposition process monitored in total internal reflection fluorescence from below. When the AFM tip with its Zinc Finger:DNA complex penetrates the evanescent field of the excitation laser, scattered light gives rise to the sharp increase, followed by the immediate drop when the tip is withdrawn. The remaining fluorescence of the Cy5 label of the transfer DNA can now clearly be discerned against the background. It

bleaches in a single step proving at the given buffer conditions that we had indeed pasted an individual molecule. As was shown in previous studies the position of this molecule can be determined with nanometer precision given a sufficient photostability. The GFP signal of a pasted complex was monitored the same way. As it is well known the fluorophore lifetime is drastically shorter but nevertheless clearly measurable proving that the transfer process had not damaged the protein!

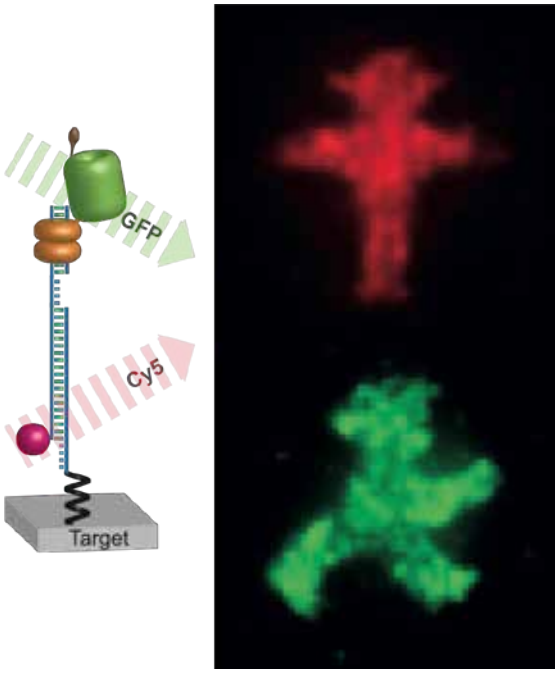

Figure 3. Out of hundreds of protein-DNA constructs a pattern displaying the red man of a pedestrian traffic light was assembled. The red emission of the Cy5 label at the DNA part was then measured. Next the pattern of a green man was assembled and this time the green fluorescence of the transferred GFP molecules was recorded. It proves that not only the cantilever bound antibody fragment stays intact during the transfer cycles, but also the transfer construct. The forces occurring during the transfer process are low enough, that the functionality of the transported GFP is not destroyed.

In order to demonstrate the robustness of the process, several hundred molecules were assembled to a micron-sized pattern of a red traffic light man[20]. The fluorescence of the Cy5 molecules could be imaged in objective-type TIRF microscopy[21] when excited with a red laser, albeit due to the Abbe-limited optics not in single molecule resolution. The microscope was then switched to blue laser excitation and molecules were assembled to form the pattern of a green traffic light man. After the assembly the green emission of the GFP molecules was recorded. The results are shown in Fig. 3. The two strongly fluorescing patterns prove the high reliability and robustness of this transport process. They also confirm that both, the fusion protein, giving rise to the GFP fluorescence, and the Cy5 labeled DNA are transported together. It should be noted that imperfections in the pattern arise from the varying functionalization densities in the depot and construction area but do not affect the conclusions drawn from this figure, that SMC&P of proteins is a feasible and robust process with negligible loss in transfer efficiency

The critical components, when transferring and assembling proteins by SMC&P are the proteins that should be arranged and observed. Twice during the transfer process forces are applied to the GFP – first during the cut and again during the paste step. Forces are required to be low enough to not alter the structure of the protein and destroy its functionality. The fluorescence of the green traffic light man unambiguously proves, that the GFP is still functional. The highest mean force that occurs during an SMC&P cycle arises as the antibody-antigen bond breaks. This force was set to be below 40 pN. Thus the hierarchical force system is gentle enough for the transfer of proteins that do not undergo serious conformational changes before this value is reached. GFP was reported to open the barrel structure only at a force of around 100 pN[22]. Destruction should therefore not be expected.

This proof of concept provides a technological approach, which will allow for the assembly of networks from arbitrary protein constituents. Systems, which develop new functionalities depending on their arrangement[23,24], can be designed and studied with respect to composition and alignment. Also the assembly of enzyme cascades will become possible and may be studied by means of single-molecule fluorescence techniques.

ASSOCIATED CONTENT

Supporting Information. Measurement details, preparation of proteins, surface chemistry, and oligonucleotide sequences are available free of charge via the Internet at http://pubs.acs.org.

AUTHOR INFORMATION

Corresponding Author

* diana.pippig@physik.uni-muenchen.de

Present Addresses

† Center for Integrated Protein Science (CIPSM), Munich, Germany.

Author Contributions

‡These authors contributed equally.

ACKNOWLEDGMENT

This work was supported by SFB 863 and the ERC.

REFERENCES

(1) Kufer, S. K.; Puchner, E. M.; Gumpp, H.; Liedl, T.; Gaub, H. E. *Science* **2008**, *319*, 594.

(2) Binnig, G.; Quate, C. F.; Gerber, C. *Phys Rev Lett* **1986**, *56*, 930.

(3) Kufer, S. K.; Strackharn, M.; Stahl, S. W.; Gumpp, H.; Puchner, E. M.; Gaub, H. E. *Nat Nanotechnol* **2009**, *4*, 45.

(4) Cordes, T.; Strackharn, M.; Stahl, S. W.; Summerer, W.; Steinhauer, C.; Forthmann, C.; Puchner, E. M.; Vogelsang, J.; Gaub, H. E.; Tinnefeld, P. *Nano Lett* **2010**, *10*, 645.

(5) Puchner, E. M.; Kufer, S. K.; Strackharn, M.; Stahl, S. W.; Gaub, H. E. *Nano Lett* **2008**, *8*, 3692.
(6) Strackharn, M.; Stahl, S. W.; Puchner, E. M.; Gaub, H. E. *Nano Lett* **2012**.
(7) Strackharn, M.; Stahl, S. W.; Severin, P. M.; Nicolaus, T.; Gaub, H. E. *Chemphyschem* **2011**.
(8) Christy, B.; Nathans, D. *Proc Natl Acad Sci U S A* **1989**, *86*, 8737.
(9) Heim, R.; Cubitt, A. B.; Tsien, R. Y. *Nature* **1995**, *373*, 663.
(10) Pedelacq, J. D.; Cabantous, S.; Tran, T.; Terwilliger, T. C.; Waldo, G. S. *Nat Biotechnol* **2006**, *24*, 79.
(11) Zahnd, C.; Spinelli, S.; Luginbuhl, B.; Amstutz, P.; Cambillau, C.; Pluckthun, A. *J Biol Chem* **2004**, *279*, 18870.
(12) Morfill, J.; Blank, K.; Zahnd, C.; Luginbuhl, B.; Kuhner, F.; Gottschalk, K. E.; Pluckthun, A.; Gaub, H. E. *Biophys J* **2007**, *93*, 3583.
(13) Greisman, H. A.; Pabo, C. O. *Science* **1997**, *275*, 657.
(14) Kim, J. S.; Pabo, C. O. *Proc Natl Acad Sci U S A* **1998**, *95*, 2812.
(15) Gerber, D.; Maerkl, S. J.; Quake, S. R. *Nat Methods* **2009**, *6*, 71.
(16) Wang, Y.; Oyokawa, S.; Han, S. W.; Huang, W.; Ikebukuro, K.; Nakamura, C.; Miyake, J. *NanoBiotechnology* **2006**, *2*, 87.
(17) Lv, S.; Dudek, D. M.; Cao, Y.; Balamurali, M. M.; Gosline, J.; Li, H. *Nature* **2010**, *465*, 69.
(18) Moy, V. T.; Florin, E. L.; Gaub, H. E. *Science* **1994**, *266*, 257.
(19) Myong, S.; Rasnik, I.; Joo, C.; Lohman, T. M.; Ha, T. *Nature* **2005**, *437*, 1321.
(20) The pattern we used shows a traffic light man as it was used in eastern Germany. After the reunification it mostly disappeared from the streets, but nowadays it can be found again in German cities.
(21) Funatsu, T.; Harada, Y.; Tokunaga, M.; Saito, K.; Yanagida, T. *Nature* **1995**, *374*, 555.
(22) Dietz, H.; Rief, M. *Proc Natl Acad Sci U S A* **2004**, *101*, 16192.
(23) Bayer, E. A.; Shimon, L. J.; Shoham, Y.; Lamed, R. *J Struct Biol* **1998**, *124*, 221.
(24) Zouni, A.; Witt, H. T.; Kern, J.; Fromme, P.; Krauss, N.; Saenger, W.; Orth, P. *Nature* **2001**, *409*, 739.

Supporting Information

Nanoscale Arrangement of Proteins by Single-Molecule Cut&Paste

Mathias Strackharn[‡], Diana A. Pippig[*,‡], Philipp Meyer, Stefan W. Stahl[†], Hermann E. Gaub

Center for Nanoscience and Department of Physics, University of Munich, Amalienstraße 54, 80799 Munich, Germany

[†] Center for Integrated Protein Science (CIPSM), Munich, Germany

[*]diana.pippig@physik.uni-muenchen.de

[‡]These authors contributed equally.

The experiments described in the manuscript were performed on an AFM/TIRFM hybrid, the details of which may be found in [1]. This supporting information specifies methods and materials that are relevant for the conduction of the measurements discussed in the main text.

AFM Measurements

A custom built AFM head and an Asylum Research MFP3D controller (Asylum Research, Santa Barbara, USA), which provides ACD and DAC channels as well as a DSP board for setting up feedback loops were used. Software for the automated control of the AFM head and xy-piezos during the SMCP experiments was programmed in Igor Pro (Wave Metrics, Lake Oswego, USA). MLCT-AUHW levers (Bruker, Camarillo, USA) were chemically modified (further below) and calibrated in solution using the equipartition theorem [2],[3]. Pulling velocities were set to 2 μm/s in the depot and 0.2 μm/s in the target area. The positioning feedback accuracy is ±3 nm. However, long term deviations may arise due to thermal drift. Typical times for one Cut & Paste cycle were in these experiments approximately 3 s.

TIRF Microscopy

The fluoresence microscope of the hybrid instrument excites the sample through the objective in total internal reflection mode. A 100x/1.49 oil immersion objective (CFI Apochromat TIRF, Nikon, Japan) was employed. Blue excitation for monitoring GFP fluorescence was achieved with a fiber-coupled 473 nm DPSS laser (CIEL, Laser Quantum, Cheshire, UK). The corresponding filter set consists of a Chroma z 470/10, a Chroma z 470 RDC and a Chroma HQ 525/50. Cy5 fluorophores were excited with a fiber-coupled 637 nm diode laser (iBeam smart, TOPTICA, München, Germany). Here the filter set was made up of a BrightLine HC 615/45, a Raman RazorEdge 633 RS, and a Chroma ET 685/70. All filters were purchased from AHF (Tübingen, Germany). Images

were recorded with a back-illuminated EMCCD camera (DU-860D, Andor, Belfast, Ireland) in frame transfer mode with 1 MHz readout rate at a frame rate of 10 Hz. The gain was set to 200. The camera was water cooled and operated at -75 °C.

Preparation of the C11L34 Single Chain Antibody Fragment

The C11L34 single chain antibody fragment was prepared as described in [4]. The scFv construct harbored a C-terminal His tag followed by a Cys to allow for site-specific immobilization and was obtained by periplasmic expression in *E. coli* SB536. C11L34 was purified by Ni^{2+} and immobilized antigen affinity chromatography according to standard protocols. The concentration was adjusted to 1.6 mg/ml in a storage buffer containing 50 mM sodium phosphate, pH 7.2, 50 mM NaCl and 10 mM EDTA.

Preparation of the GCN4-GFP-Zinc Finger Fusion Construct

A fusion protein construct consisting of an N-terminal GCN4(7P14P)-tag [4] (RMKQLEPKVEELLPKNYHLENEVARLKKLVGER) and the six Zinc Finger peptide Zif268/NRE (with an RQKDGERP linker sequence between the Zif268 and NRE moieties) was designed according to [5]. All construct fragments were amplified from synthetic templates (Mr.Gene or Geneart, Lifetechnologies, Paisley, UK). GCN4 was cloned into pET28a between NcoI and NdeI restriction sites. The original sequence coding for the Thrombin cleavage site in pET28a was replaced by one coding for the TEV-protease recognition site. Zif268/NRE was inserted subsequently between NdeI and NotI sites. A C-terminal ybbR-tag (DSLEFIASKLA) [6] is flanking the Zinc Finger region. The whole construct was subcloned into pGEX6P2 by means of BamHI and XhoI sites. Superfolder GFP [7] followed by a SGSG linker was inserted between the TEV

coding site and Zif268/NRE by sequence and ligation independent cloning [8].
The resulting fusion protein (GCN4-TEV-sfGFP-Zif268/NRE-ybbR) harbored a GST-tag and was expressed in *E.coli* BL21 DE3 cells. For this, one liter of SB medium was inoculated with 10 ml of an overnight culture and grown at 37°C. When an OD_{600} of 0.7 had been reached, over night expression at 18°C was induced by adding 0.25mM IPTG.

Cells were lysed in 50mM Tris HCl pH 7.5, 300 mM NaCl, 2mM DTT, 5% Glycerol, 10μM $ZnCl_2$ by a French pressure cell press. The GCN4-GFP-Zinc Finger construct was obtained in the soluble fraction and purified by Glutathione affinity chromatography on GST Trap columns (GE Healthcare, Freiburg, Germany). After over night incubation with PreScission protease the GST-tag was removed and the protein further purified by Heparin cation exchange chromatography (HiTrap Heparin, GE Healthcare, Freiburg, Germany). The purified fusion protein was dialyzed into storage buffer (50mM Tris HCl pH7.5, 150mM NaCl, 2mM DTT, 10μM $ZnCl_2$, 5% Glycerol), stored at -80°C and had a final concentration of 10μM.

Preparation of Cantilevers

Cantilevers were oxidized in a UV-ozone cleaner (UVOH 150 LAB, FHR Anlagenbau GmbH, Ottendorf-Okrilla, Germany) and silanized by soaking for 2 min in (3-Glycidoxypropyl)trimethoxysilane (ABCR, Karlsruhe, Germany). Subsequently they were washed in toluene, 2-propanol and ddH_2O and dried at 80 °C for 40 min. After incubating the cantilever in 10 mg/ml aminodextrane (D1860, Invitrogen, Carlsbad, USA) in a sodium borate buffer (pH 8.5), a heterobifunctional PEG crosslinker [9] with

N-hydroxy succinimide and maleimide groups (MW 5000, Rapp Polymere, Tübingen, Germany) was then applied for 1 h at 30 mM and then the C11L34 antibody fragments were bound at 8 °C to the lever during 4 h. Finally the cantilever was washed with PBS.

Preparation of Cover Glass Slips

Cover glasses were sonicated in 50% (v/v) 2-propanol in dd$H_2$0 for 15 min and oxidized in solution of 50% (v/v) hydrogen peroxide (30%) and sulfuric acid for 30 min. They were then washed in ddH_2O and dried in a nitrogen stream, silanized by soaking for 1 h in (3-Glycidoxypropyl)trimethoxysilane (ABCR, Karlsruhe, Germany). Subsequently they were washed twice in 2-propanol and ddH_2O and dried at 80 °C for 40 min. After this they were incubated in 10 mg/ml aminodextrane (D1860, Invitrogen, Carlsbad, USA) in a sodium borate buffer (pH 8.5), a heterobifunctional PEG crosslinker with N-hydroxy succinimide and maleimide groups (MW 5000, Rapp Polymere, Tübingen, Germany) was then applied for 1 h at 30 mM. Depot and Target DNA was reduced with TCEP and subsequently purified by ethanol precipitation. DNA pellets were dissolved in a phosphate buffer (pH 7.2, 50 mM NaCl, 10 mM EDTA). Target DNA was mixed with 10 % of a thiolated oligomer with the Zinc Finger recognition sequence. This ensures that a fusion protein without DNA, which might during the experiment attach to the cantilever, does not block antibody binding sites. A microfluidics system was now fixed on the cover glass, and the depot or the target oligomers were pumped through the channels for 1 h. Subsequently both channels were flushed with PBS. Zinc Finger A and B oligomers were mixed to 500 nM in a 1:1 ratio in PBS, heated to 80 °C during 10 min and then

cooled at 4 °C for 90 min. The fusion protein was added to a final concentration of 500 nM and allowed to bind to the DNA during additional 90 min. The protein-DNA solution was then flowed through the Depot channel for 90 min. Subsequently the channel was rinsed again with PBS and the microfluidics system was removed.

Oligomer Sequences

thiolated depot oligomer

5' SH - TTT TTT CAT GCA AGT AGC TAT TCG AAC TAT AGC TTA AGG ACG TCA A

thiolated target oligomer

5' CAT GCA AGT AGC TAT TCG AAC TAT AGC TTA AGG ACG TCA ATT TTT – SH

Zinc Finger A oligomer

5' Cy5 TTTGACGTCCTTAAGCTATAGTTCGAATAGCTACTTGCATGTTTTTTTTTTTTTTTTTT TTTTTTTTTTTTCTGCAAGGGTTCAGGCGTGGGCGGTAAG

Zinc Finger B oligomer

5' CTTACCGCCCACGC C TGAACCCTTGCAGA

References

1. Gumpp, H., et al., *Ultrastable combined atomic force and total internal reflection fluorescence microscope [corrected].* The Review of scientific instruments, 2009. **80**(6): p. 063704.

2. Florin, E., *Sensing specific molecular interactions with the atomic force microscope.* Biosensors and Bioelectronics, 1995. **10**(9-10): p. 895-901.
3. Butt, H.J. and M. Jaschke, *Calculation of thermal noise in atomic-force microscopy.* Nanotechnology, 1995. **6**(1): p. 1-7.
4. Morfill, J., et al., *Affinity-matured recombinant antibody fragments analyzed by single-molecule force spectroscopy.* Biophysical journal, 2007. **93**(10): p. 3583-90.
5. Kim, J.S. and C.O. Pabo, *Getting a handhold on DNA: design of poly-zinc finger proteins with femtomolar dissociation constants.* Proceedings of the National Academy of Sciences of the United States of America, 1998. **95**(6): p. 2812-7.
6. Yin, J., et al., *Site-specific protein labeling by Sfp phosphopantetheinyl transferase.* Nature protocols, 2006. **1**(1): p. 280-5.
7. Pedelacq, J.D., et al., *Engineering and characterization of a superfolder green fluorescent protein.* Nature biotechnology, 2006. **24**(1): p. 79-88.
8. Bryksin, A.V. and I. Matsumura, *Overlap extension PCR cloning: a simple and reliable way to create recombinant plasmids.* BioTechniques, 2010. **48**(6): p. 463-5.
9. Celik, E. and V.T. Moy, *Nonspecific interactions in AFM force spectroscopy measurements.* J Mol Recognit, 2012. **25**(1): p. 53-6.

Anhänge und Ausblicke

A) Farbstoff-bindende Aptamere für die optische Auslesung molekularer Prozesse: Möglichkeiten und Herausforderungen

In den vorgestellten Experimenten wurde die Fluoreszenz eines Malachit Grün-Moleküls, die auftritt, sobald das Molekül in die Bindungstasche des Malachit Grün-Aptamers gebunden hat, zum Auslesen der gelungenen funktionellen Assemblierung verwendet. Diese Vorgehensweise kann auch auf andere Systeme übertragen werden. Allein die Herstellung eines Aptamers durch Transkription einer entsprechenden DNA-Vorlage mit Hilfe einer RNA-Polymerase stellt schon ein System zur Verfügung, dessen enzymatische Aktivität auf der Ebene von einzelnen Molekülen beobachtet werden kann. Sobald die Transkription eines Aptamers vollständig abgelaufen ist, kann sich das Aptamer bilden und ein Malachit Grün-Molekül gebunden werden. Die Fluoreszenz des gebundenen Malachit Grüns kann dann gemessen werden. Durch Verwendung einer zirkulären DNA-Vorlage kann der Vorgang von einer Polymerase beliebig oft wiederholt werden. In diesem Fall sollte nach jeder vollständigen Transkription ein Aufblitzen zu beobachten sein. Dies ermöglicht also, die zeitlichen Abstände zwischen der vollständigen Herstellung der Aptamere zu messen und Auskunft über die Fluktuationen zu geben, denen der Herstellungsprozess unterliegt. Auch die Beobachtung komplexerer Konstellationen ist möglich. Im folgenden Kapitel wird darauf eingegangen werden. Neben dem Malachit Grün-Aptamer gibt es noch weitere farbstoffbindende Aptamere. Eine fluorogene Wirkung zeigt z.B. auch das von Paige et al. veröffentlichte Spinach-Aptamer, das einen Farbstoff bindet, der dem Farbstoffzentrum von GFP ähnelt (11). Auch hier wird durch Binden des Farbstoffs in die Aptamer-Bindungstasche die Fluoreszenz um drei Größenordnungen verstärkt. Dieses Aptamer kann in gleicher Weise verwendet werden, um die Arbeitsweise individueller Enzyme zu beobachten. Durch die deutlich längere Aptamer-Sequenz erhält man allerdings hier Zugriff auf langsamere Produktionsraten. Insgesamt muss bedacht werden, dass die Dauer für die vollständige Transkription eines Aptamers nur einen Mittelwert über viele Katalyseschritte wiedergibt. Ferner benötigt auch die Faltung in die korrekte Aptamerstruktur eine gewisse Zeit, wobei dieser Prozess das Auftreten des Fluoreszenzsignals insbesondere für komplexere Aptamere verzögern kann. Zeitliche Fluktuationen, denen die korrekte Faltung unterliegt, überlagern die der zu untersuchenden Polymeraseaktivität.

Besonderes Augenmerk musste bei den Experimenten mit dem Malachit Grün-Aptamer auf die Oberfächenfunktionalisierung gerichtet werden. Da Malachit Grün eine gewisse Affinität zu silanisierten Oberflächen aufwies, konnten diese nicht verwendet werden, denn der damit einhergehende stärkere Hintergrund ließ nicht die Messung einzelner Moleküle zu. Aus diesem Grund wurden für die Herstellung größerer Muster Amino-Dextrane direkt auf oxidierte Glasoberflächen gebunden, für die Beobachtung des Blinkverhaltens von Malachit Grün bei einzelnen Malachit Grün-Molekülen wurden in gleicher Weise NHS-Polyethylenglykol-Maleimid-Moleküle verwendet. Dennoch ist ersichtlich, dass Fluoreszenz auch von einzelnen Punkten entsteht, an denen sich kein Aptamer befindet (vgl. Supplement von Publikation 6). Das Spinach-Aptamer verhält sich in dieser Hinsicht möglicherweise vorteilhafter. Untersuchungen an einzelnen Spinach-Aptameren sind im Gange und Ergebnisse werden in der Masterarbeit von P. Meyer nachzulesen sein. Durch eine nanometergenaue Lokalisierung des Malachit Grün-Aptamers und des Ursprungs der Malachit Grün-Fluoreszenz konnte eine Beobachtung von falsch-positiven ausgeschlossen werden. Ein ähnliches Vorgehen ist bei der Beobachtung einzelner Enzyme denkbar, wenn diese fluoreszent gelabelt sind.

Es konnte bei den Experimenten außerdem beobachtet werden, dass eine gewisse Wahrscheinlichkeit dafür besteht, dass das Malachit Grün-Aptamer zerstört wird, wenn die gebundenen Farbstoffe gebleicht werden. Dieses Verhalten wurde von Grate und Wilson mit entstehenden Radikalen erklärt (12). Eigene Untersuchungen haben gezeigt, dass das Bleichen nicht einem einfach exponentiellen Verlauf folgt. Durch ein einfaches Modell, das außer Binden und Dissoziation auch eine endgültige Zerstörung des Aptamers in Betracht zieht, konnte das Bleichverhalten des im Aptamer gebundenen Malachit-Grüns erklärt werden.

Die Differentialgleichungen zu diesem System lauten:

$$\frac{d}{dt} bright(t) = k_{on} dark(t) - (k_{off} + k_{bleach}) bright(t)$$

$$\frac{d}{dt} dark(t) = k_{off} bright(t) - k_{on} dark(t)$$

$$\frac{d}{dt} destroyed(t) = k_{bleach} bright(t),$$

wobei k_{on}, k_{off} und k_{bleach} die Raten für das Binden, Dissoziieren und Zerstören sind. Die Lösung für den gebundenen Zustand ist

$$bright(t) = \frac{e^{t(-\frac{1}{2}k_{sum}+\frac{1}{2}\sqrt{a})}k_{on}(2\sqrt{a}k_{off}+2\sqrt{a}k_{on}-\sqrt{a}k_{sum}+a)}{ak_{on}+ak_{off}}$$
$$+\frac{1}{2}\frac{1}{a(k_{on}+k_{off})}\left(e^{t\left(-\frac{1}{2}k_{sum}-\frac{1}{2}\sqrt{a}\right)}k_{on}(-2\sqrt{a}k_{off}-2\sqrt{a}k_{on}+a+\sqrt{a}k_{sum})\right)$$

wobei $a = k_{off}^2 + 2k_{off}k_{bleich} + 2k_{off}k_{on} + k_{bleach}^2 - 2k_{on}k_{bleach} + k_{on}^2$.

Die Zerstörung des Aptamers durch Radikale macht eine Langzeitmessung des Bindens und Dissoziierens von Malachit Grün-Molekülen in und aus einem einzelnen Aptamer sehr schwer. Die Verwendung von Radikalfängern (auch von den in (12) angegebenen) hatte in den durchgeführten Experimenten keinen Einfluss. Es ist möglich, dass das Spinach-Aptamer, das das GFP nachahmt, sich in dieser Hinsicht vorteilhafter verhält, denn von GFP ist bekannt, dass die Generierung von Radikalen erst bei größeren Lichtleistungen induziert wird (85). Für das Auslesen der Transkriptionsrate in dem vorgeschlagenen Experiment sollte aber die Fluoreszenz eines gebundenen Malachit-Grün Moleküls ausreichen.

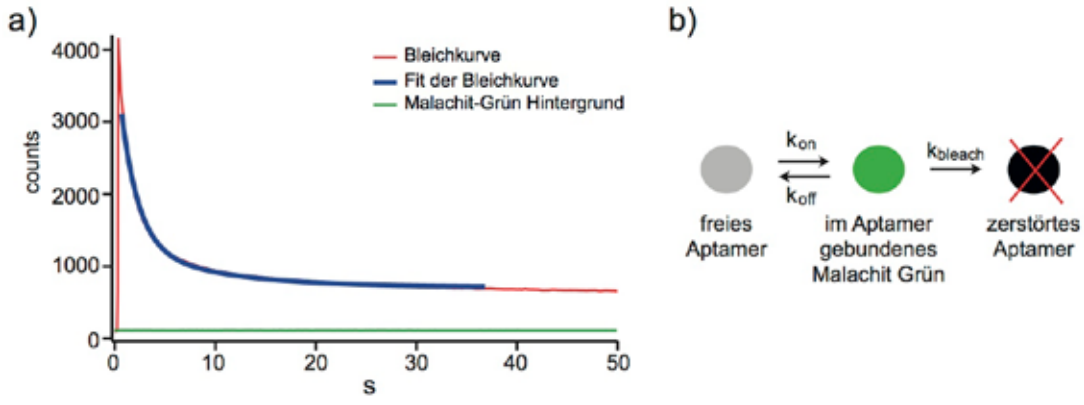

Fig. 19 Das Bleichen eines Ensembles von aptamerisch gebundenen Malachit-Grün Molekülen kann durch ein einfaches Modell beschrieben werden. In das freie Aptamer kann Malachit Grün binden. Nach dem Bleichen dissoziiert dieses aber wieder. Radikale können die endgültige Zerstörung des Aptamers herbeiführen. a) zeigt Bleichkurve und Fit nach diesem Modell. b) Skizze des Modells.

B) Die räumliche Anordnung biomolekularer Netzwerke auf Oberflächen

Im vorangehenden Kapitel wurde bereits beschrieben, wie die im Rahmen dieser Arbeit entwickelten Techniken zur zeitlichen Kontrolle enzymatischer Ereignisse verwendet werden können. Außerdem wurden Werkzeuge entwickelt, die es ermöglichen ganz gezielt einzelne Proteine auf Oberflächen zu positionieren. Da biologische Systeme in komplexen Netzwerken organisiert sind, ist das Verständnis der molekularen Abläufe in enzymatischen Systemen und ihre Abhängigkeit von räumlichen Parametern von enormer Bedeutung. Hier ist z.B. das stochastische Verhalten kleiner Systeme zwar schon theoretisch modelliert, bedarf aber noch einer experimentellen Validierung (9). Mit den in Publikation 1 und 7 gezeigten Möglichkeiten des direkten sowie sukzessiven Aufbaus von nanoskaligen Protein-Arrangements ist es möglich, derartige Systeme aus individuellen Komponenten aufzubauen und in verschiedenen geometrischen Konstellationen zu testen. Die im vorangehenden Kapitel vorgestellte Methode, Polymerase-Aktivität auszulesen, indem als Transkript einer DNA-Vorlage ein farbstoffbindendes Aptamer hergestellt wird, kann aufgegriffen werden, um ein einfaches, gekoppeltes Modellsystem herzustellen. Einzelne Polymerasen werden hierfür in einem bestimmten Abstand und in einer bestimmten Konstellation zueinander positioniert. Wenn die Polymerasen an dieselbe DNA-Vorlage binden und diese transkribieren, dann sind sie mechanisch über Spannung und Torsionsmoment gekoppelt. Dadurch sollte eine Korrelation der Aktivitäten der Enzyme entstehen. Die Single-Molecule Cut&Paste Technik bietet nun die Möglichkeit, verschiedene Geometrien aufzubauen und dadurch die Stärke der Kopplung zu regulieren. Genauso ist es vorstellbar, die Länge der DNA-Vorlage zu variieren oder verschieden schnell arbeitende Polymerasen zu verwenden. Die gekoppelten Aktivitäten der einzelnen Enzyme werden durch das Auftreten von Fluoreszenz an den Positionen der Polymerasen nachgewiesen, sobald ein Aptamer-Transkript erzeugt wurde. Die Zuordnung des Fluoreszenzsignals zu einer Polymerase kann durch Anfitten der Intensitätsverteilung und nanometergenaue Lokalisierung sichergestellt werden.

Das Cellulosom ist ein weiteres sehr interessantes Enzymsystem. Die Enzyme dieses Systems werden auf Membranen von Bakterien (z.B. Clostridium thermocellum) auf Scaffoldin-Einheiten räumlich organisiert wodurch die Degradierung von Zuckern mit besonders großer Effizienz durchgeführt wird (78). Dass für die wirtschaftliche Nutzung von Pflanzenzuckern zur Energiegewinnung derartige artifizielle Systeme, sogenannte Designercellulosome, von großem Nutzen sein können, macht deren detaillierte Studien und Optimierung wichtig. Durch Nutzung einer Vielzahl von Depots, in denen

verschiedene für die Degradation benötigte Enzyme gespeichert werden, können mit den erarbeiteten Single-Molecule Cut&Paste Methoden auf einer Konstruktionsfläche verschiedene künstliche Cellulosome zusammengestellt werden. Für die Vielzahl der benötigten Enzymkomponenten werden große Zahlen von Depotflächen benötigt. Für deren Herstellungen können individuell ansteuerbare Mikrofluidiken und *in vitro* Expressionssysteme verwendet werden (86). Da die Cellulasen besonders dicht nebeneinander aufgebaut werden müssen, muss die Präzision der Positionierung für diese Experimente optimiert werden. Insbesondere sind die Antikörperfragmente nur in großer Zahl und an langkettigen Zuckern am Cantilever für Single-Molecule Cut&Paste Experimente verwendet worden, um die Transfereffizienz zu erhöhen. Für höchste Präzision in der Positionierung ist es aber notwendig, mit einem Molekül an der Spitze zu arbeiten und die für die kovalente Anbindung an den Cantilever verwendeten Zuckerpolymere möglichst kurz zu halten (vgl. Publikation 2). Für das effiziente Zusammenstellen von Cellolusomen ist es also nötig, entweder die Kopplungseffizienz der Antikörperfragmente zu vergrößern, oder zusätzlich zu verifizieren, dass die Positionierung der Enzyme vollständig durchgeführt wurde.

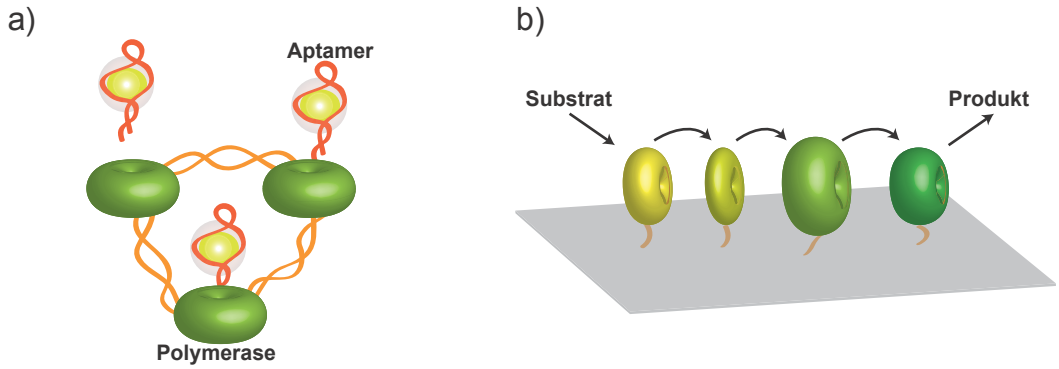

Fig. 20 Mögliche experimentelle Umsetzungen für enzymatische Netzwerke. a) Mehrere RNA-Polymerasen transkribieren dasselbe zirkuläre DNA-Template und erzeugen dabei Aptamere, die nach ihrer Fertigstellung fluorogene Farbstoffe binden und ein Fluoreszenzsignal emittieren. Die Polymerasen sind über die DNA mechanisch gekoppelt. b) In Designercellulosomen wird Cellulose nacheinander von verschiedenen Cellulasen prozessiert. Durch SMC&P können solche Systeme optimiert werden, indem man eine Vielzahl von Kombinationen zusammenstellt und testet.

Referenzen

1. Schrödinger, E., *What is Life? The Physical Aspect of the Living Cell*. (Univerity Press, Cambridge, 1948).
2. Meinhardt, H.; Prusinkiewicz, P.; Fowler, D. R., *The algorithmic beauty of sea shells*. The virtual laboratory (Springer-Verlag, Berlin ; New York, 1995), pp. xi, 204 p.
3. Elowitz, M. B.; Levine, A. J.; Siggia, E. D.; Swain, P. S.; *Stochastic gene expression in a single cell.* Science **2002**, 297 (5584), 1183-1186.
4. Raj, A.; Peskin, C. S.; Tranchina, D.; Vargas, D. Y.; Tyagi, S.; *Stochastic mRNA synthesis in mammalian cells.* PLoS Biol **2006**, 4 (10), e309.
5. Lu, H. P.; Xun, L.; Xie, X. S.; *Single-molecule enzymatic dynamics.* Science **1998**, 282 (5395), 1877-1882.
6. Terentyeva, T. G.; Engelkamp, H.; Rowan, A. E.; Komatsuzaki, T.; Hofkens, J.; Li, C. B.; Blank, K.; *Dynamic disorder in single-enzyme experiments: facts and artifacts.* ACS Nano **2012**, 6 (1), 346-354.
7. Kou, S. C.; Cherayil, B. J.; Min, W.; English, B. P.; Xie, X. S.; *Single-molecule Michaelis-Menten equations.* J Phys Chem B **2005**, 109 (41), 19068-19081.
8. Qian, H.; Elson, E. L.; *Single-molecule enzymology: stochastic Michaelis-Menten kinetics.* Biophys Chem **2002**, 101-102, 565-576.
9. Armbruster, D.; Nagy, J. D.; van de Rijt, E. A.; Rooda, J. E.; *Dynamic simulations of single-molecule enzyme networks.* J Phys Chem B **2009**, 113 (16), 5537-5544.
10. Gorris, H. H.; Walt, D. R.; *Mechanistic Aspects of Horseradish Peroxidase Elucidated through Single-Molecule Studies.* J Am Chem Soc **2009**, 131 (17), 6277-6282.
11. Paige, J. S.; Wu, K. Y.; Jaffrey, S. R.; *RNA mimics of green fluorescent protein.* Science **2011**, 333 (6042), 642-646.
12. Grate, D.; Wilson, C.; *Laser-mediated, site-specific inactivation of RNA transcripts.* Proc Natl Acad Sci U S A **1999**, 96 (11), 6131-6136.

13. Crommie, M. F.; Lutz, C. P.; Eigler, D. M.; *Confinement of electrons to quantum corrals on a metal surface.* Science **1993**, 262 (5131), 218-220.

14. Baum, R.; *Nanotechnology. Drexler and Smalley make the case for and against 'molecular assemblers'.* Chemical & Engineering News **2003**, 81 (48), 37-42.

15. Kufer, S. K.; Puchner, E. M.; Gumpp, H.; Liedl, T.; Gaub, H. E.; *Single-molecule cut-and-paste surface assembly.* Science **2008**, 319 (5863), 594-596.

16. Yildiz, A.; Forkey, J. N.; McKinney, S. A.; Ha, T.; Goldman, Y. E.; Selvin, P. R.; *Myosin V walks hand-over-hand: single fluorophore imaging with 1.5-nm localization.* Science **2003**, 300 (5628), 2061-2065.

17. Hirschfeld, T.; Block, M. J.; Mueller, W.; *Virometer: an optical instrument for visual observation, measurement and classification of free viruses.* J Histochem Cytochem **1977**, 25 (7), 719-723.

18. Moerner, W. E.; Kador, L.; *Optical detection and spectroscopy of single molecules in a solid.* Phys Rev Lett **1989**, 62 (21), 2535-2538.

19. Shera, E. B.; Seitzinger, N. K.; Davis, L. M.; Keller, R. A.; Soper, S. A.; *Detection of single fluorescent molecules.* Chemical Physics Letters **1990**, 174 (6),

20. Minsky, M.; *Memoir on inventing the confocal scanning microscope.* Scanning **1988**, 10 (4), 128-138.

21. Axelrod, D.; *Cell-substrate contacts illuminated by total internal reflection fluorescence.* J Cell Biol **1981**, 89 (1), 141-145.

22. Levene, M. J.; Korlach, J.; Turner, S. W.; Foquet, M.; Craighead, H. G.; Webb, W. W.; *Zero-mode waveguides for single-molecule analysis at high concentrations.* Science **2003**, 299 (5607), 682-686.

23. Tokunaga, M.; Kitamura, K.; Saito, K.; Iwane, A. H.; Yanagida, T.; *Single molecule imaging of fluorophores and enzymatic reactions achieved by objective-type total internal reflection fluorescence microscopy.* Biochem Bioph Res Co **1997**, 235 (1), 47-53.

24. Cheezum, M. K.; Walker, W. F.; Guilford, W. H.; *Quantitative comparison of algorithms for tracking single fluorescent particles.* Biophys J **2001**, 81 (4), 2378-2388.

25. Thompson, R. E.; Larson, D. R.; Webb, W. W.; *Precise nanometer localization analysis for individual fluorescent probes.* Biophys J **2002**, 82 (5), 2775-2783.

26. Yildiz, A.; Selvin, P. R.; *Fluorescence imaging with one nanometer accuracy: application to molecular motors.* Acc Chem Res **2005**, 38 (7), 574-582.

27. Betzig, E.; Patterson, G. H.; Sougrat, R.; Lindwasser, O. W.; Olenych, S.; Bonifacino, J. S.; Davidson, M. W.; Lippincott-Schwartz, J.; Hess, H. F.; *Imaging intracellular fluorescent proteins at nanometer resolution.* Science **2006**, 313 (5793), 1642-1645.

28. Hess, S. T.; Girirajan, T. P.; Mason, M. D.; *Ultra-high resolution imaging by fluorescence photoactivation localization microscopy.* Biophys J **2006**, 91 (11), 4258-4272.

29. Rust, M. J.; Bates, M.; Zhuang, X.; *Sub-diffraction-limit imaging by stochastic optical reconstruction microscopy (STORM).* Nat Methods **2006**, 3 (10), 793-795.

30. Steinhauer, C.; Forthmann, C.; Vogelsang, J.; Tinnefeld, P.; *Superresolution microscopy on the basis of engineered dark states.* J Am Chem Soc **2008**, 130 (50), 16840-16841.

31. Klar, T. A.; Hell, S. W.; *Subdiffraction resolution in far-field fluorescence microscopy.* Opt Lett **1999**, 24 (14), 954.

32. Smith, S. B.; Finzi, L.; Bustamante, C.; *Direct mechanical measurements of the elasticity of single DNA molecules by using magnetic beads.* Science **1992**, 258 (5085), 1122-1126.

33. Ashkin, A.; *Applications of laser radiation pressure.* Science **1980**, 210 (4474), 1081-1088.

34. Binnig, G.; Quate, C. F.; Gerber, C.; *Atomic Force Microscope.* Phys Rev Lett **1986**, 56 (9), 930-933.

35. Bustamante, C.; Macosko, J. C.; Wuite, G. J.; *Grabbing the cat by the tail: manipulating molecules one by one.* Nat Rev Mol Cell Biol **2000**, 1 (2), 130-136.

36. Meyer, G.; Amer, N. M.; *Novel optical approach to atomic force microscopy.* Appl Phys Lett **1988**, 53 (12), 1045.

37. Puchner, E. M.; Alexandrovich, A.; Kho, A. L.; Hensen, U.; Schafer, L. V.; Brandmeier, B.; Grater, F.; Grubmuller, H.; Gaub, H. E.; Gautel, M.; *Mechanoenzymatics of titin kinase.* Proc Natl Acad Sci U S A **2008**, 105 (36), 13385-13390.

38. Viani, M. B.; Schäffer, T. E.; Chand, A.; Rief, M.; Gaub, H. E.; Hansma, P. K.; *Small cantilevers for force spectroscopy of single molecules.* Journal of Applied Physics **1999**, 86 (4), 2258.

39. Watson, J. D.; Crick, F. H.; *Molecular structure of nucleic acids; a structure for deoxyribose nucleic acid.* Nature **1953**, 171 (4356), 737-738.

40. Šponer, J.; Leszczyński, J.; Hobza, P.; *Nature of Nucleic Acid–Base Stacking: Nonempirical ab Initio and Empirical Potential Characterization of 10 Stacked Base Dimers. Comparison of Stacked and H-Bonded Base Pairs.* The Journal of Physical Chemistry **1996**, 100 (13), 5590-5596.

41. http://de.wikipedia.org/wiki/Desoxyribonukleinsäure. (2012).

42. Rothemund, P. W.; *Folding DNA to create nanoscale shapes and patterns.* Nature **2006**, 440 (7082), 297-302.

43. Douglas, S. M.; Dietz, H.; Liedl, T.; Hogberg, B.; Graf, F.; Shih, W. M.; *Self-assembly of DNA into nanoscale three-dimensional shapes.* Nature **2009**, 459 (7245), 414-418.

44. Liedl, T.; Hogberg, B.; Tytell, J.; Ingber, D. E.; Shih, W. M.; *Self-assembly of three-dimensional prestressed tensegrity structures from DNA.* Nat Nanotechnol **2010**, 5 (7), 520-524.

45. Strunz, T.; Oroszlan, K.; Schafer, R.; Guntherodt, H. J.; *Dynamic force spectroscopy of single DNA molecules.* Proc Natl Acad Sci U S A **1999**, 96 (20), 11277-11282.

46. Albrecht, C. H.; Neuert, G.; Lugmaier, R. A.; Gaub, H. E.; *Molecular force balance measurements reveal that double-stranded DNA unbinds under force in rate-dependent pathways.* Biophys J **2008**, 94 (12), 4766-4774.

47. Essevaz-Roulet, B.; Bockelmann, U.; Heslot, F.; *Mechanical separation of the complementary strands of DNA.* Proc Natl Acad Sci U S A **1997**, 94 (22), 11935-11940.

48. Rief, M.; Clausen-Schaumann, H.; Gaub, H. E.; *Sequence-dependent mechanics of single DNA molecules.* Nat Struct Biol **1999**, 6 (4), 346-349.

49. Morfill, J.; Blank, K.; Zahnd, C.; Luginbuhl, B.; Kuhner, F.; Gottschalk, K. E.; Pluckthun, A.; Gaub, H. E.; *Affinity-matured recombinant antibody fragments analyzed by single-molecule force spectroscopy.* Biophys J **2007**, 93 (10), 3583-3590.

50. Zahnd, C.; Spinelli, S.; Luginbuhl, B.; Amstutz, P.; Cambillau, C.; Pluckthun, A.; *Directed in vitro evolution and crystallographic analysis of a peptide-binding single chain antibody fragment (scFv) with low picomolar affinity.* J Biol Chem **2004**, 279 (18), 18870-18877.

51. Klug, A.; *The discovery of zinc fingers and their applications in gene regulation and genome manipulation.* Annu Rev Biochem **2010**, 79, 213-231.

52. Pavletich, N. P.; Pabo, C. O.; *Zinc finger-DNA recognition: crystal structure of a Zif268-DNA complex at 2.1 A.* Science **1991**, 252 (5007), 809-817.

53. Fairall, L.; Schwabe, J. W.; Chapman, L.; Finch, J. T.; Rhodes, D.; *The crystal structure of a two zinc-finger peptide reveals an extension to the rules for zinc-finger/DNA recognition.* Nature **1993**, 366 (6454), 483-487.

54. Geurts, A. M.; Cost, G. J.; Freyvert, Y.; Zeitler, B.; Miller, J. C.; Choi, V. M.; Jenkins, S. S.; Wood, A.; Cui, X.; Meng, X.; Vincent, A.; Lam, S.; Michalkiewicz, M.; Schilling, R.; Foeckler, J.; Kalloway, S.; Weiler, H.; Menoret, S.; Anegon, I.; Davis, G. D.; Zhang, L.; Rebar, E. J.; Gregory, P. D.; Urnov, F. D.; Jacob, H. J.; Buelow, R.; *Knockout rats via embryo microinjection of zinc-finger nucleases.* Science **2009**, 325 (5939), 433.

55. Kim, J. S.; Pabo, C. O.; *Getting a handhold on DNA: design of poly-zinc finger proteins with femtomolar dissociation constants.* Proc Natl Acad Sci U S A **1998**, 95 (6), 2812-2817.

56. Pabo, C. O.; Peisach, E.; Grant, R. A.; *Design and selection of novel Cys2His2 zinc finger proteins.* Annu Rev Biochem **2001**, 70, 313-340.

57. Nudler, E.; Mironov, A. S.; *The riboswitch control of bacterial metabolism.* Trends Biochem Sci **2004**, 29 (1), 11-17.

58. Tuerk, C.; Gold, L.; *Systematic evolution of ligands by exponential enrichment: RNA ligands to bacteriophage T4 DNA polymerase.* Science **1990**, 249 (4968), 505-510.

59. Romig, T. S.; Bell, C.; Drolet, D. W.; *Aptamer affinity chromatography: combinatorial chemistry applied to protein purification.* J Chromatogr B Biomed Sci Appl **1999**, 731 (2), 275-284.

60. Brockstedt, U.; Uzarowska, A.; Montpetit, A.; Pfau, W.; Labuda, D.; *In vitro evolution of RNA aptamers recognizing carcinogenic aromatic amines.* Biochem Bioph Res Co **2004**, 313 (4), 1004-1008.

61. Stojanovic, M. N.; Kolpashchikov, D. M.; *Modular aptameric sensors.* J Am Chem Soc **2004**, 126 (30), 9266-9270.

62. Ben-Amotz, D.; Harris, C. B.; *Ground- and excited-state torsional dynamics of a triphenylmethane dye in low-viscosity solvents.* Chemical Physics Letters **1985**, 119 (4), 305-311.

63. Abedin, K. M.; Ye, J. Y.; Inouye, H.; Hattori, T.; Sumi, H.; Nakatsuka, H.; *Diffusive torsional dynamics of malachite green molecules in solid matrices probed by fluorescence decay.* The Journal of Chemical Physics **1995**, 103 (15), 6414.

64. Babendure, J. R.; Adams, S. R.; Tsien, R. Y.; *Aptamers switch on fluorescence of triphenylmethane dyes.* J Am Chem Soc **2003**, 125 (48), 14716-14717.

65. Baugh, C.; Grate, D.; Wilson, C.; *2.8 A crystal structure of the malachite green aptamer.* J Mol Biol **2000**, 301 (1), 117-128.

66. Kolpashchikov, D. M.; *Binary malachite green aptamer for fluorescent detection of nucleic acids.* J Am Chem Soc **2005**, 127 (36), 12442-12443.

67. Kühner, F.; Gaub, H. E.; *Modelling cantilever-based force spectroscopy with polymers.* Polymer **2006**, 47 (7), 2555-2563.

68. Kufer, S. K.; Strackharn, M.; Stahl, S. W.; Gumpp, H.; Puchner, E. M.; Gaub, H. E.; *Optically monitoring the mechanical assembly of single molecules.* Nat Nanotechnol **2009**, 4 (1), 45-49.

69. DeChancie, J.; Houk, K. N.; *The origins of femtomolar protein-ligand binding: hydrogen-bond cooperativity and desolvation energetics in the biotin-(strept)avidin binding site.* J Am Chem Soc **2007**, 129 (17), 5419-5429.

70. Chaiet, L.; Wolf, F. J.; *The Properties of Streptavidin, a Biotin-Binding Protein Produced by Streptomycetes.* Arch Biochem Biophys **1964**, 106, 1-5.

71. Duwez, A.-S.; Willet, N., *Molecular Manipulation with Atomic Force Microscopy*. (CRC Press, 2012).

72. Morfill, J.; Kuhner, F.; Blank, K.; Lugmaier, R. A.; Sedlmair, J.; Gaub, H. E.; *B-S transition in short oligonucleotides.* Biophys J **2007**, 93 (7), 2400-2409.

73. Evans, E.; Ritchie, K.; *Strength of a weak bond connecting flexible polymer chains.* Biophys J **1999**, 76 (5), 2439-2447.

74. Strackharn, M.; Stahl, S. W.; Severin, P. M.; Nicolaus, T.; Gaub, H. E.; *Peptide-Antibody Complex as Handle for Single-Molecule Cut & Paste.* Chemphyschem **2011**,

75. Wang, Y.; Oyokawa, S.; Han, S. W.; Huang, W.; Ikebukuro, K.; Nakamura, C.; Miyake, J.; *Analysis of DNA and Zinc Finger Interactions using Mechanical Force Spectroscopy.* NanoBiotechnology **2006**, 2, 87-93.

76. Dietz, H.; Rief, M.; *Exploring the energy landscape of GFP by single-molecule mechanical experiments.* Proc Natl Acad Sci U S A **2004**, 101 (46), 16192-16197.

77. Nixon, P. J.; Michoux, F.; Yu, J.; Boehm, M.; Komenda, J.; *Recent advances in understanding the assembly and repair of photosystem II.* Ann Bot **2010**, 106 (1), 1-16.

78. Bayer, E. A.; Shimon, L. J.; Shoham, Y.; Lamed, R.; *Cellulosomes-structure and ultrastructure.* J Struct Biol **1998**, 124 (2-3), 221-234.

79. Edman, L.; Földes-Papp, Z.; Wennmalm, S.; Rigler, R.; *The fluctuating enzyme: a single molecule approach.* Chemical Physics **1999**, 247 (1), 11-22.

80. Hassler, K.; Rigler, P.; Blom, H.; Rigler, R.; Widengren, J.; Lasser, T.; *Dynamic disorder in horseradish peroxidase observed with total internal reflection fluorescence correlation spectroscopy.* Opt Express **2007**, 15 (9), 5366-5375.

81. Berglund, G. I.; Carlsson, G. H.; Smith, A. T.; Szoke, H.; Henriksen, A.; Hajdu, J.; *The catalytic pathway of horseradish peroxidase at high resolution.* Nature **2002**, 417 (6887), 463-468.

82. Rodriguez-Lopez, J. N.; Gilabert, M. A.; Tudela, J.; Thorneley, R. N.; Garcia-Canovas, F.; *Reactivity of horseradish peroxidase compound II toward substrates: kinetic evidence for a two-step mechanism.* Biochemistry **2000**, 39 (43), 13201-13209.

83. Sakurada, H.; Koizumi, H.; Ohkawara, A.; Ueda, T.; Kamo, N.; *Use of dihydrorhodamine 123 for detecting intracellular generation of peroxides upon UV irradiation in epidermal keratinocytes.* Arch Dermatol Res **1992**, 284 (2), 114-116.

84. Zhou, M.; Diwu, Z.; Panchuk-Voloshina, N.; Haugland, R. P.; *A stable nonfluorescent derivative of resorufin for the fluorometric determination of trace hydrogen peroxide: applications in detecting the activity of phagocyte NADPH oxidase and other oxidases.* Anal Biochem **1997**, 253 (2), 162-168.

85. Tour, O.; Meijer, R. M.; Zacharias, D. A.; Adams, S. R.; Tsien, R. Y.; *Genetically targeted chromophore-assisted light inactivation.* Nat Biotechnol **2003**, 21 (12), 1505-1508.

86. Gerber, D.; Maerkl, S. J.; Quake, S. R.; *An in vitro microfluidic approach to generating protein-interaction networks.* Nat Methods **2009**, 6 (1), 71-74.

Danksagung

In dieser steckt Arbeit mehr als nur stundenlanges Messen im verdunkelten Keller oder die Arbeit in unserem Labor. Kluge Köpfe und fleißige Hände haben zum Gelingen beigetragen, ich wurde getröstet und ermuntert. An die ganze Gambi-Crew geht mein Dank für die unglaublich gute Atmosphäre, in der eben auch gute Wissenschaft gemacht werden kann.

Für die Unterstützung bedanke ich mich ganz besonders bei ...

...Prof. Hermann Gaub (Gambi) für die Ideen, Ratschläge und Diskussionen, die hervorragende Arbeitsumgebung und die kulinarischen Highlights, die diese Arbeit gedeihen ließen.

...Stefan Stahl, weil er bei unendlich vielen Messungen bei Tag und bei Nacht als AFM-Profi und Freund zur Seite stand.

...Diana Pippig für ihr gutes Händchen beim Zink-Finger und die angenehme Zeit beim Messen und beim anschließenden Eis essen.

...Philip Severin für die Herstellung von Proben am Microspotter und die Beratung bei der Auswertung von Kraftkurven.

...Elias Puchner für gute Diskussionen und die Zusammenarbeit beim Malachit-Grün-Aptamer.

...Stefan Kufer für das ganze *know how* in Hinsicht auf Einzelmoleküle und SMC&P, das er mir hinterlassen hat.

...Philipp Meyer für die vielen ZiFi-SMC&P-Messungen, die er geduldig vorbereitet und durchgeführt hat.

...Thorben Cordes für die gute Zusammenarbeit bei der Superresolution Mikroskopie.

...Prof. Philip Tinnefeld und Ingo Stein dafür, dass sie immer als Ansprechpartner in Fluoreszenzmikroskopiefragen da waren.

...Ralf David, mit dem ich tagelang Enzyme vorbereitet und nächtelang Enzyme gesucht habe.

...Hermann Gumpp für die Einführung in die Welt der kombinierten TIRF/AFM-Mikroskopie

...Thomas Nikolaus und Angelika Kardinal für die Hilfe und die gute Laune im Labor.

...Martin Benoit und Stefan Scheuer für Hilfe beim Hubschrauberfliegen und den unglaublich großen Spaß im Büro.

Für Ihre große Unterstützung, Geduld, Verständnis und ganz viel Daumendrücken danke ich ganz besonders herzlich Mama, Abasi und Kathrin.